Imperial College London

# Optical Near-Field Dynamics of Active 2D Semiconductors

Stefano Guazzotti

Condensed Matter Theory Group

Department of Physics

Imperial College London

August 2018

Thesis submitted for the degree of

Doctor of Philosophy of Imperial College London

*In loving memory of Massimo Guazzotti*

*Because you contributed to make me who I am today.*

## DECLARATION OF ORIGINALITY

I hereby declare that all material presented in this thesis is my own work, except where otherwise noted.

Stefano Guazzotti

## COPYRIGHT DECLARATION

# Abstract

When structures with a strong confinement of the electromagnetic fields are considered, the near-field dynamics becomes integral to the description of a semiconductor. Not only it provides feedback from the environment, as is the case in a laser system, but it further mediates the interaction between different, otherwise independent, positions. In such a context, a full-field spatio-temporal description is essential to faithfully describe the dynamics of either an extended semiconductor system or a set of spatially separated emitters.

This thesis highlights the importance of combining a complex (many-body and band-resolved) model of semiconductor carrier dynamics with a full-field description of the electromagnetic fields by presenting some applications. With the recent rise in popularity of atomically thin materials, semiconductors can be embedded in increasingly smaller optical environments, whose properties can only be studied by self-consistently combining carrier and field dynamics.

The ability to calculate the linear and non-linear response of a system under arbitrary excitation conditions is shown. This is performed without any prior knowledge of the electromagnetic environment and can thus be extended to complex geometries. By embedding active materials in a tailored environment, the complex interaction of the two can be exploited to engineer the optical response of the system by using a self-consistent modelling technique.

The complex dynamical interaction between field and gain in a semiconductor laser is another example of a system in which a self-consistent model is required. Here, a set of one-dimensional simulations is reported showing how the output of a semiconductor laser is highly sensitive to perturbation arising from sub-wavelength dynamics of the gain medium. By introducing a random patterning of the laser cavity, a novel approach

to the suppression of dynamical instabilities in a laser output is demonstrated. This scheme, based on complex wave interference, is introduced by spatially perturbing the optical environment.

# Acknowledgements

There are many people that helped and supported me during the long path of my PhD. Some of them provided technical help, others supported me in an academical sense. Many, many more helped me going through the bright and dark patches that arose during the last four years. I want to thank all of you here, but let me first spend a few words to acknowledge the contribution that everyone in my pre-PhD life had on this accomplishment. Even without directly appearing in my recent life, you all took part in shaping me, be it via positive or negative actions. This includes everyone from L'Aquila and Trieste for those wonderful university years, before we all parted ways.

With this out of the way, I would like to move to the people that have popped in and out of my life in the last four years.

First of all, I want to thank Alex, Emilio, Mario and Simone. It has now been 10 years, but I still remember our alternative approach to school with a large smile. I am especially grateful that you showed up when I needed it the most.

I would like to thank everyone who was in the PhD office when I joined and made me feel welcome, which is not an easy feat; thank you Adam, Fabian, Fionn, Freddie, John, Matthias and Ollie. And Peter D., who has seen two whole generations of PhD students going through the office. Many more thanks to the people who joined with me — Jamie, Peter F., Prem and Seyed — and everyone who arrived afterwards — Alexandra, Fan, Gleb, Iacopo, Marise, Nuttawut, Simon L. and Simon P. . A special thank goes to Illya and Lara for their emotional support and for pushing me to write. You all made the office a nice and fun place to work in.

I would like to thank Sang Soon as well as Stefan Bittner and Hui Cao — from over in Yale — for the productive and stimulating work we did together.

A very special thank you to Andreas and Doris for the amazing mixture of experience, fun, guidance, help and — personal as well as academic — support you were always happy to provide. I would like to thank my supervisor Prof. Ortwin Hess for providing such an amazing opportunity to experience the world of research.
A special mention goes to Francesca for all the support and love she showed me over the years. I don't think I can even find the words to express my gratitude, so I will just tell you this: a PhD can make you feel hopeless at times, but with you at my side I could almost go through another one.
Finally, I want to express all my gratitude and love to my parents and my sister for their support throughout my studies and this PhD.

# Contents

# List of Figures

# List of Tables

# Acronyms

**ABC** Absorbing boundary conditions

**AR** anti reflection

**ADE** Auxiliary Differential Equation

**CW** continuous wave

**DFT** density functional theory

**DBR** distributed Bragg reflector

**EFA** Envelope Function Approximation

**FP** Fabry–Pérot

**FDTD** Finite Difference Time Domain

**FWHM** full width half maximum

**HF** Hartree-Fock

**JDOS** joint density of states

**QW** Quantum Well

**RPA** random-phase approximation

**SESAM** semiconductor saturable absorber mirror

**SHG** Second Harmonic Generation

**THG** Third Harmonic Generation

**TMDC** Transition Metal Dichalcogenide

# List of publications

Portions of this thesis has been drawn from the following publications:

- S. Guazzotti, A. Pusch, D. E. Reiter, and O. Hess. "Dynamical calculation of third-harmonic generation in a semiconductor quantum well" Physical Review B **94**, 115303 (2016)
- S. Bittner, S. Guazzotti, Y. Zeng, X. Hu, H. Yılmaz, K. Kim, S. S. Oh, Q. J. Wang, O. Hess, and H. Cao. "Suppressing spatiotemporal lasing instabilities with wave-chaotic microcavities" Science (2018)
- S. Guazzotti, A. Pusch, D. E. Reiter, and O. Hess. "Dynamic theory of nanophotonic control of two-dimensional semiconductor nonlinearities" Physical Review B **98**, 245307 (2018)

# 1 Introduction

Most solid state physics textbooks define semiconductors quite loosely, either from their room temperature resistivity or their band structure and particularly bandgap. As an example, Ashcroft and Mermin [4] write

> Solids that are insulators at $T = 0$, but whose energy gaps are of such a size that thermal excitation can lead to observable conductivity at temperatures below the melting point, are known as *semiconductors*.

Regardless of their imprecise categorisation, semiconductors are a central component of our modern lifestyles. The ability to engineer the electronic properties of semiconductors on increasingly smaller scales is what underlies the Digital Revolution and the advent of the information Age. At the same time, their optical properties were refined and used to produce several devices which contributed to shape the modern world, e.g., photodiodes, light-emitting diodes (LED), laser diodes and photovoltaic cells[5, 6].

One remarkable property of semiconductors is their huge variety. Indeed, not only many naturally occurring minerals are semiconductors, but even more can be artificially produced. This large variety encompasses several different classes. Some semiconductor are composed of atoms of a single element either in crystalline form, e.g., silicon and selenium, or in more sophisticated structures, like Buckminsterfullerene ($C_{60}$) or carbon nanotubes. Other non elemental semiconductors include binary compounds, for example the III-V or II-VI are composed of elements from the third and fifth, or second and sixth, columns of the periodic table. This results in a very wide variety of optical and electronic properties[7, 8].

Another big advancement in semiconductor manufacturing came from the introduction of heterostructures. The concept of layering different semiconductor materials to

manipulate their optoelectronic properties was pioneered in 1969 to improve the performance of semiconductor lasers[6, 9]. This was instrumental in achieving continuous wave operation of semiconductor lasers at room temperature and strongly contributed to bringing them out of the lab.

Further developments in crystal growth techniques led to better control over heterostructure properties as well as the ability to manufacture thinner semiconductor layers. It was then possible to create a very sharp transition between a central thin layer of lower band gap material, e.g., GaAs, embedded in a crystal with higher bandgap, e.g., AlAs. In such a structure, known as a lattice matched Quantum Well (QW), the confinement of motion in the growth direction results in a partially discrete set of electronic states. This results in a quasi-two-dimensional electronic system with novel optoelectronic properties[7, 8, 10]. Nowadays, increasingly advanced techniques allow the realisation of more complex semiconductor heterostructures, in which the electron motion can be confined to a two-, one- or zero-dimensional subspace. These structures, commonly known as quantum wells, quantum wires and quantum dots, respectively, and their combinations create the possibility to engineer semiconductor systems with very peculiar properties[11].

The field of semiconductor physics is still evolving very quickly and new applications and devices appear all the time, e.g., quantum dot displays[12] are becoming commercially available. In the remainder of this introduction we will proceed to a more detailed discussion about some topics in semiconductor physics which are closely related to the work included in this Thesis. In particular, we explore some of the recent developments in the field of semiconductor lasing, with an emphasis on high power lasers. Furthermore, we discuss the discovery of a new class of atomically thin direct gap semiconductors and some of their remarkable properties.

### Semiconductor lasers

As we discussed in the previous section, the introduction of heterostructures and quantum confinement had a strong impact on the field of semiconductor lasers by enabling stable operation at room temperature. Following that, semiconductor lasers spread through various industries where they have been used for all sort of applications, from reading and writing optical discs to fibre-optic communication. Stable semiconductor lasers operating at low to medium power can be achieved from the edge emission of a QW in a narrow stripe-geometry. For these systems, the laser optical cavity is formed by the QW plane itself resulting in a long gain region which enables low threshold lasing. When this geometry is laterally expanded to achieve higher power, however, the resulting edge emitting QW lasers show spatio-temporal instabilities in the emission characterised by filamentation and pulsation[13–18]. These arise from the complex non-linear interaction between the optical field and the semiconductor gain[19–21] and are worsened by the large interaction area and the presence of several transverse modes. Several approaches have been proposed to reduce or suppress these instabilities in order to achieve high power lasing with stable beam profiles[22–28].

An alternative to broad area semiconductor lasers is presented by the family of surface-emitting lasers. In these systems the optical cavity is aligned along the growth direction of the QW and thus the emission happens from the QW surface. The longitudinal confinement of light is achieved through two distributed Bragg reflectors (DBRs) which can either be both integrated in the diode structure (vertical-cavity surface-emitting laser or VCSEL) or one integrated and one external (vertical-external-cavity surface-emitting laser or VECSEL)[29–33].

### Transition Metal Dichalcogenides

Ever since the successful isolation of graphene by Novoselov [34], a new research field has formed to explore the properties of atomically thin materials[35–38]. More recently,

a renewed interest in this class of materials has been sparked by the isolation of $MoS_2$ monolayers and their optical characterisation[39, 40].

Molybdenum disulfide is a representative of a larger class of materials, collectively named Transition Metal Dichalcogenides (TMDCs). These are compounds of a transition metal element, M, and a chalcogen element, X, with chemical composition $MX_2$. The bulk form of these materials is a layered system in which the repeated unit, analogous to graphene in a graphite bulk, is formed through strong covalent bonds. The presence of weak van der Waals-like bonds in the stacking direction allows for easy mechanical exfoliation of the system resulting in the isolation of single or few layers. Each of these units, known as a monolayer, is composed of two triangular lattices of X and an interleaved triangular lattice of M. This results in a strongly-bound quasi-two-dimensional hexagonal monolayer.

Several TMDCs show extraordinary optical and electronic properties coming from the confinement of electrons in two-dimensional subspaces. In 2010, Mak et al. [39] and Splendiani et al. [40] observed a large increase in total luminescence when going from bulk $MoS_2$ to a single monolayer. This results from a crossover from indirect to direct bandgap which had been predicted via *ab initio* calculations by Li and Galli [41] and Lebègue and Eriksson [42]. Indeed, both experiments and calculations show that the indirect gap is strongly blueshifted with decreasing number of layers. In contrast, the band structure at the K and K′ points, where the direct gap is located, is dominated by strongly localised orbitals with very weak inter-layer interaction and is thus independent on the number of layers[39–45]. Following $MoS_2$, several groups observed photoluminescence in other TMDC monolayers, including $MoSe_2$ and $WSe_2$[46–48].

Other remarkable properties of this class of two-dimensional materials come from the presence of two degenerate but non-equivalent valleys located at the K and K′ points of the hexagonal reciprocal lattice. As a consequence of the broken inversion symmetry, the optical interband transitions have valley dependent selection rules, such that right- (left-) circularly polarised light only excites carriers in the K (K′) valley[49–53]. Furthermore, the presence of the valley Hall effect (in which carriers from different valleys flow

to opposite transverse edges under an in-plane electric field) has been predicted[54] and recently observed[55]. Lastly, $MoS_2$ has a strong spin-orbit coupling which results in the split of the valence band inside the K and K′ valleys[56]. The combination of polarisation selection rules and spin-split-induced frequency selection rules create the novel possibility of optically exciting carriers with various combinations of spin and valley indices[57].

Another important consequence of the two-dimensional nature of TMDC monolayers is the weakening of the screening provided by the electron-hole plasma. This is expected to reduce the screening of the carrier-carrier Coulomb interaction, resulting in strongly bound excitons[45, 58–61]. Indeed, recent experiments have shown remarkable agreement with the values predicted via *ab initio* calculations as well as strong deviation from the common Rydberg series for higher energy levels[62–67]. Furthermore, screening in two-dimensional materials is strongly dependent on the dielectric environment, which affects the bandgap and exciton binding energies[43, 58, 60, 68–72].

It was recently shown that the broken inversion symmetry in TMDC monolayers results in a non-vanishing second order non-linearity[73, 74]. The system, however, is centrosymmetric when it is composed of two (or an even number of) layers, causing suppression of the Second Harmonic Generation (SHG). Leveraging this strong sensitivity to layer thickness, SHG can be used as a powerful microscopy technique to characterise TMDC flakes[75]. Lastly, generation of a second harmonic shows a very large enhancement when the excitation is resonant with half of an electronic transition, providing a powerful spectroscopic tool to investigate excitons in TMDC monolayers[66]

In conclusion, the two-dimensional nature of this class of semiconductors results in the possibility of easily embedding them in very diverse structures, ranging from van der Waals heterostructures[76] to photonic[77–80] and plasmonic[81–84] cavities, where their unique properties can be enhanced and manipulated.

## THESIS STRUCTURE

This thesis is structured as follows.

Chapter 2 provides an overview of the theory involved in the study of the near-field dynamics of active two-dimensional semiconductors. We quickly overview the time-domain full-field approach to the dynamics of the electromagnetic fields (section 2.1) and the electronic properties of quasi-free electrons in crystalline semiconductors (section 2.2). Following that, we present the density matrix and second quantisation formalisms (section 2.3) and their use in deriving the equations of motion for a system of independent electrons (section 2.4). Section 2.5 shows the perturbative approach to non-linear optics including the second and third order susceptibilities of some relevant few-level systems. In section 2.6 we discuss the Coulomb interaction and the derivation of the semiconductor Bloch equations in HF approximation. We further discuss the inclusion of some additional terms which introduce in a phenomenological way some of the characteristic features of carrier-carrier interaction. Finally, section 2.7 shows how the model can be adapted to a $MoS_2$ monolayer, which is taken as the prototypical TMDC.

Chapter 3 shows results for the carrier and polarisation dynamics in a semiconductor QW in the linear (section 3.1) and non-linear regimes (section 3.2). These results have first been published in Guazzotti et al. [1]. The second half of the chapter (section 3.3) focusses on the linear and non-linear dynamics of TMDC monolayers, including SHG and its enhancement. This is partly included in a manuscript which is currently under review.

Chapter 4 discusses the dynamics of carriers in a semiconductor QW laser, with particular emphasis on the self-consistent interaction with the time-domain description of the electromagnetic field. In section 4.1 we explain the changes (additions and simplifications) to the model needed in order to describe lasing from a semiconductor system. Section 4.2 shows the unstable lasing dynamics which is observed in a one-dimensional FP laser. In section 4.3 we discuss the inclusion of carrier transport through a diffusion model and its effect on carrier and field dynamics. Finally, we show how changing from

a simple FP cavity to a disordered one results in complex wave dynamics and instability suppression (section 4.4). A subset of the results of chapter 4 forms the theoretical component of Bittner et al. [2].

Finally, chapter 5 presents a unifying look over the main results of this thesis and provides an outlook.

# 2 Theory of optical excitation of semiconductor carriers

In this chapter we introduce the theoretical background which allows to study the near-field dynamics of two-dimensional semiconductors. This is rooted in the description and interaction of two separate physical systems, the electromagnetic fields on one side and the semiconductor charge carriers on the other. To investigate the semiconductor dynamics under the near-field feedback coming from nano- and micro-cavities, we use a classical description for the electromagnetic subsystem, based on the direct solution of Maxwell's equations in their differential formulation. This results in a spatio-temporal full-field description with sub-wavelength resolution.

The quantum nature of the charge carriers in the semiconductor is accounted for through a description of the electronic states arising in the semiconductor in terms of the band structure of the bulk material and any quantum confinement effects introduced by the presence of heterojunctions. Furthermore, the density matrix formalism is introduced to provide a statistical description of the dynamics of charge carriers in the macroscopic semiconductor subsystem. The combination of classical electromagnetic fields and quantum mechanical carriers results in a model extending Maxwell-Bloch equations to a many-body band-resolved semiconductor system.

Finally, the macroscopic quantum coherences arising from the density matrix formalism are used to introduce feedback from the semiconductor carriers to the electromagnetic fields. This results in a two-way interaction between the two subsystems and thus a self-consistent picture of the near-field dynamics of the combined semiconductor-light-cavity system.

## 2.1 SPATIO-TEMPORAL DYNAMICS OF ELECTROMAGNETIC FIELDS

We will start with a few brief words about the Finite Difference Time Domain (FDTD) method, but a more comprehensive treatment can be obtained from a variety of sources[85–87]. The method describes the time evolution of the electromagnetic fields, **E** and **B**, by solving the differential formulation of Maxwell's equations in space and time domain under the assumption of no free charges or currents,

$$\nabla \cdot \mathbf{D} = 0 \tag{2.1a}$$

$$\nabla \cdot \mathbf{B} = 0 \tag{2.1b}$$

$$\nabla \times \mathbf{E} = -\frac{\partial \mathbf{B}}{\partial t} \tag{2.1c}$$

$$\nabla \times \mathbf{H} = \frac{\partial \mathbf{D}}{\partial t} \,. \tag{2.1d}$$

This requires the knowledge of an initial configuration over a finite spatial domain, which will then be propagated forward in time according to a discretised version of eq. 2.1. The finite spatial grid is truncated through the use of suitable boundary conditions describing how the simulation domain interfaces with the *outside world*, e.g., being a finite system in empty space or an infinite periodic system. Finally, some way to introduce fields in the simulation domain is required, either via a localised oscillating current, representing an internal source, e.g., emission from an atom or a molecule, or injecting a travelling wave into the domain, which represents an external plane wave reaching the system of interest.

The time evolution of the fields includes both the electric, **E**, and displacement, **D**, fields. This defines the electric polarisation, $\mathbf{P}(\mathbf{r}, t)$ which can be used to introduce a dynamical response of the material at **r**,

$$\mathbf{D} = \varepsilon_0 \mathbf{E} + \mathbf{P} \,. \tag{2.2}$$

This polarisation can then be separated in an active component, $\mathbf{P}_a$, which is treated dynamically and a background component, $\mathbf{P}_b$, arising from phonons, strongly off-resonant electronic transitions, and other off-resonant processes. The background polarisation is assumed to be linear with respect to the field, $\mathbf{P}_b = \varepsilon_0 \chi_b \mathbf{E}$, leading to the introduction of an effective background permittivity, $\varepsilon_b = 1 + \chi_b$,

$$\mathbf{D} = \varepsilon_0 \varepsilon_b \mathbf{E} + \mathbf{P}_a \, . \tag{2.3}$$

A similar relationship holds between the magnetic fields, $\mathbf{B}$ and $\mathbf{H}$, via the magnetic polarisation, also known as magnetisation, $\mathbf{M}$. In this thesis, however, we only focus on the electric response of active media. One well-established method to introduce materials in the FDTD method is through the use of the Auxiliary Differential Equation (ADE) method. This allows us to include the response from arbitrary materials for which a time domain description of the polarisation as a classical field can be formulated. The time evolution of $\mathbf{P}$ is usually governed by one or multiple differential equations, the auxiliary equations, which in turn usually depend on $\mathbf{E}$ or $\mathbf{B}$. The calculation is then performed by stepping Maxwell's equations forward in time alongside the auxiliary differential equations.

## 2.2 BLOCH ELECTRONS IN CRYSTALLINE SEMICONDUCTORS

In order to present a model capable of providing the optical response of a semiconductor in terms of a dynamically calculated polarisation for the composing electrons, let us start from a brief review of the quantum mechanical description of electrons in solids with an emphasis on semiconductor materials. A more detailed description can be found in several books, like Ashcroft and Mermin [4] or Kittel [88]. This would require to, in principle, solve the many-body Schrödinger equation for the electron-nuclei system. In order to make the problem tractable, a series of successive approximations is used resulting in the problem of independent electrons subjected to a static and periodic

external potential which effectively represent the attraction from the nuclei as well as part of the electron-electron repulsion. This is an eigenvalue problem that corresponds to finding the solutions to the following time-independent single-particle Schrödinger equation

$$\mathcal{H}_0\psi(\mathbf{r}) = \mathcal{T}\psi(\mathbf{r}) + \mathcal{U}_{\text{eff}}(\mathbf{r})\psi(\mathbf{r}) = \mathcal{E}\psi(\mathbf{r}), \tag{2.4}$$

where $\mathcal{T}$ is the single-particle kinetic energy term in the position representation

$$\mathcal{T} = -\frac{\hbar^2}{2m}\nabla_{\mathbf{r}}^2 \tag{2.5}$$

and $\mathcal{U}_{\text{eff}}(\mathbf{r})$ is the effective potential whose periodicity matches that of the underlying lattice of nuclei, i.e., $\mathcal{U}_{\text{eff}}(\mathbf{r}) = \mathcal{U}_{\text{eff}}(\mathbf{r}+\mathbf{R})$ for all lattice vectors $\mathbf{R}$.

Following Bloch theorem, we can write the eigenstates of $\mathcal{H}_0$ as Bloch waves

$$\psi_{n\mathbf{k}}(\mathbf{r}) = e^{i\mathbf{k}\cdot\mathbf{r}}u_{n\mathbf{k}}(\mathbf{r}) \tag{2.6}$$

where the solution is labelled with $\mathbf{k}$, the wave vector in the reciprocal lattice, and $n$, which identifies different solutions with a given $\mathbf{k}$. The final piece of the solution is the function $u_{n\mathbf{k}}(\mathbf{r})$ which has the same periodicity as the effective potential, $\mathcal{U}_{\text{eff}}(\mathbf{r})$, and is itself the solution of a related eigenvalue problem

$$\mathcal{H}_{\mathbf{k}}u_{n\mathbf{k}}(\mathbf{r}) = \left(\frac{\hbar^2}{2m}\left(\frac{\nabla}{i}+\mathbf{k}\right)^2 + \mathcal{U}_{\text{eff}}(\mathbf{r})\right)u_{n\mathbf{k}}(\mathbf{r}) = \mathcal{E}_n(\mathbf{k})\,u_{n\mathbf{k}}(\mathbf{r}). \tag{2.7}$$

For a given value of $n$, $\mathcal{E}_n(\mathbf{k})$, called an energy band, is a continuous function over $\mathbf{k}$ with the periodicity of the reciprocal lattice. The band structure of the crystal, i.e., the full set of eigenvalues $\mathcal{E}_n(\mathbf{k})$, contains information on which energy regions, called bandgaps, are forbidden to Bloch electrons due to the absence of states. The presence and position of these bandgaps with respect to the number of electrons, and therefore the Fermi energy, has a substantial influence on the electron dynamics as well as on the optical response of the electron system.

Semiconductors are defined as those materials in which the Fermi energy lies within a bandgap with a consequent separation between valence (occupied) bands and conduction (unoccupied) bands. In this situation we can exploit the periodicity and continuity of each band, $\mathcal{E}_n(\mathbf{k})$, to state that we are bound to have a maximum of a valence band, $n = v$, and a minimum of a conduction band, $n = c$, between which the bandgap lies We can further perform Taylor expansions to find a parabolic approximation of the two bands around the energy extrema

$$\widetilde{\mathcal{E}}_v(\mathbf{K}_v) \approx \mathcal{E}_v(\mathbf{k}_{v0}) - \frac{1}{2} k_\mu \left|\mathbf{H}^v_{\mu\nu}\right| k_\nu \tag{2.8a}$$

$$\widetilde{\mathcal{E}}_c(\mathbf{K}_c) \approx \mathcal{E}_c(\mathbf{k}_{c0}) + \frac{1}{2} k_\mu \left|\mathbf{H}^c_{\mu\nu}\right| k_\nu, \tag{2.8b}$$

where $\mathbf{H}^n_{\mu\nu}$ is the Hessian of band $n$, $\mathbf{K}_n = \mathbf{k} - \mathbf{k}_{n0}$ is the wave vector measured from the extremum of band $n$, $\mathbf{k}_{n0}$, and the $+$ $(-)$ sign explicitly identify the conduction (valence) band as having a minimum (maximum). It is customary to define a band dependent effective mass tensor, $[M_n]_{\mu\nu}$, as

$$\left[M_n^{-1}\right]_{\mu\nu} = \frac{1}{\hbar^2} \frac{\partial^2 \mathcal{E}_n(\mathbf{k})}{\partial k_\mu \partial k_\nu}. \tag{2.9}$$

which allows the dispersion to be rewritten in parabolic approximation, making it similar to that of free electrons. In particular, if we look at the case where the effective mass tensor is isotropic

$$\widetilde{\mathcal{E}}_n(\mathbf{K}) \approx \mathcal{E}_{n0} \pm \frac{\hbar^2 \mathbf{K}^2}{2|m_n|} \tag{2.10}$$

where $\mathcal{E}_{n0} = \mathcal{E}_n(\mathbf{k}_{n0})$ and $m_n$ is the effective mass for band $n$, i.e., the single value present in the effective mass tensor. This leads us to the introduction of *holes*, i.e., unoccupied electronic states, as the relevant carriers in the valence band. Holes behave like particles with a positive effective mass $m_h = -m_v$, (hence the $-$ and $\pm$ signs in eqs. 2.10 and 2.8a respectively) carrying a positive elementary charge, $+e$.

This approximation, also known as the effective mass approximation, can be used to greatly simplify the band structure when looking at the dynamics of carriers in semicon-

ductor systems, provided that electrons are not created with too much energy. Indeed, this is the case when the semiconductor system is probed or excited through light whose frequency is close to (or lower than) the bandgap.

When the excitation lies well above the bandgap, the semiconductor response can be described in two different ways:

1. a full treatment can be achieved by adopting the complete band structure and including some kind of relaxation model,

2. a suitable quasi-equilibrium distribution(s) can be used as an initial state.

The latter method provides a simpler model capable of correctly calculating the response to (ultra)-short pulses of a system when the exact dynamics of achieving quasi-equilibrium is not essential. The initial state usually consists of a set of Fermi-Dirac distribution for the different bands, where the temperature relates to the excess energy for carriers in the given band. An important remark is that this approximation is orthogonal to the band structure description and can be applied together with the effective mass approximation or with a more sophisticated band structure.

On the other hand, one may be interested in the interplay between carrier relaxation and external excitation. In this case, a more complex model can be built using the complete band structure and carrier relaxation, as well as energy dissipation, can be included at several levels of precision as will be partially discussed in section 2.6.

The theory that will be presented in the rest of this chapter, from section 2.3 on, can be used either with or without parabolic band approximation, as the band structure only enters as a set of parameters that can be calculated beforehand.

One last important feature we can extract from the band structure is the nature of the gap which can be qualified as either *direct*, when $\mathbf{k}_{v0} = \mathbf{k}_{c0}$ or *indirect*, when the band extrema are located at different points of the reciprocal space. This difference has a strong effect on the interband carrier dynamics and thus on the response to electromagnetic fields. In this work, we will only focus on direct gap semiconductors, even though the model can be extended to provide a description suitable for indirect gap systems.

### 2.2.1 The Envelope Function Approximation

In this work we focus on two-dimensional systems. The simplest way to introduce a two-dimensional system in a semiconductor is through the growth of a heterostructure consisting of a thin slab of lower-bandgap material, the QW proper, between two half-spaces, the *barriers*, see fig. 2.1a. As the thickness of the inner material decreases, the lowest-lying electronic states will start to get confined in one direction and thus show a partially discrete spectrum, this is known as a Quantum Well (QW). One way to get an approximate solution is the Envelope Function Approximation (EFA). This consists in factorising the wave function into a component that changes on atomic length-scales and a much slower varying function which acts as an envelope. It is thus possible to calculate the envelope function by solving a Schrödinger equation for the semiconductor electrons and holes subject to a confinement potential which is determined by the heterostructure. This can be reduced to a lower-dimensional problem by looking at the symmetry of the confinement potential

$$\left(-\frac{\hbar^2\nabla_{\mathbf{s}}^2}{2m_n(\mathbf{s})}+\mathcal{U}_{\text{conf}}(\mathbf{s})\right)\phi_j(\mathbf{s})=\epsilon_j\phi_j(\mathbf{s}) \tag{2.11}$$

where $\mathbf{s}$ stands for the subset of $\mathbf{r}$ along which the confinement potential is not constant, i.e., $\mathcal{U}_{\text{conf}}(\mathbf{r})=\mathcal{U}_{\text{conf}}(\mathbf{s})$, and $m_n(\mathbf{s})$ is the effective mass in band $n$, which will in principle change across different materials. As a consequence of the non-constant mass, the Hamiltonian in eq. 2.11 is in general non-Hermitian. The resulting spectrum, $\epsilon_j$, is usually composed of a set of discrete levels, arising from localised states, and a continuum formed by delocalised crystal states that are too energetic to be trapped.

The resulting total energy of this single-particle state can be obtained as the sum of the energy in the confined and unconfined directions

$$E_{nj}(\mathbf{k}_\perp)=\epsilon_{nj}+\mathcal{E}_n(\mathbf{k}_\perp) \tag{2.12a}$$

$$E_n(\mathbf{k}_\mathbf{s},\mathbf{k}_\perp)=\epsilon_n(\mathbf{k}_\mathbf{s})+\mathcal{E}_n(\mathbf{k}_\perp) \tag{2.12b}$$

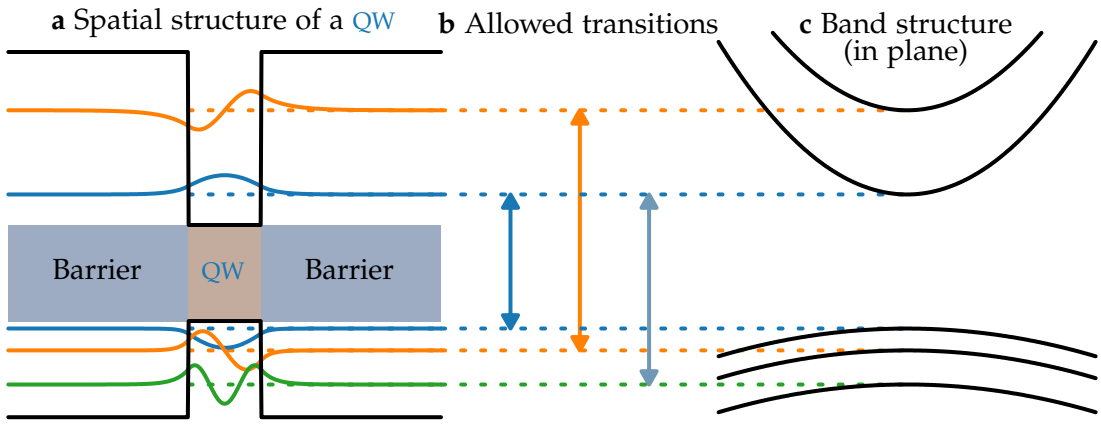


**Figure 2.1:** Graphical representation of a QW. Subfigure a shows the spatial structure of a QW, consisting of a thin layer (red shading) sandwiched between to infinitely thick barriers (blue shading). The black line represent the spatial variation of the valence band maximum and conduction band minimum, as well as the QW confinement potential. The dashed (continuous) lines show the energy (wave function) of the bound states of the confinement potential. The arrows in b show the optically allowed transitions in dipole approximation. Subfigure c shows the electron and hole subbands arising from the confined states along $z$ and with a parabolic dispersion in the $xy$ plane.

where $n$ is the index of the bulk band, $\mathbf{k}_\perp$ is the wave vector in the unconfined direction, and the two lines in eq. 2.12 represent the bound and unbound states, respectively, indexed by the (discrete set) $\mathbf{j}$ and (continuous) $\mathbf{k_s}$ quantum numbers. The set of discrete results labelled by the index $j$ and arising from the same band, $n$, is referred to as the subband spectrum to stress its origin from the splitting of a single band. In this thesis, the focus is on the states arising from the bound solutions to eq. 2.11, which are most relevant for excitations below the bulk bandgap energy. The model can be extended to account for the unbound states as well as barrier, i.e., bulk, states.

When talking about QWs we are referring to heterostructures in which electrons are confined in a single dimension, the growth direction. This reduces eq. 2.11 to a 1D Schrödinger equation whose solutions are characterised by a single discrete quantum number and a two-dimensional wave vector. We will keep with the convention of aligning the growth direction along the $z$ axis, i.e., $\mathbf{s} = \hat{z}$ and $\mathbf{k}_\perp = (k_x, k_y)$ Some sophisticated confinement potentials can be found in the literature to describe QWs with specific, experimentally observed or growth-induced, characteristics like strain, equally spaced levels, broken inversion symmetry[7, 89–91].

Here we will focus on the simplest 1D confinement potential,

$$U_{\text{conf}}(z) = \begin{cases} 0 & \text{for } |z| < \frac{L}{2} \\ U_0 & \text{for } |z| > \frac{L}{2} \end{cases} \tag{2.13}$$

which is a finite square well of thickness L, cf. fig. 2.1a, well suited to the description of lattice matched QWs. Nevertheless, the extension to more complex confinement models or multiple quantum wells is straightforward. In this model the total confinement potential for electrons and holes is taken as the bandgap mismatch between barrier and well materials,

$$U_{e0} + U_{h0} = \Delta_b - \Delta_w, \tag{2.14}$$

where $\Delta_b$ ($\Delta_w$) is the bandgap of the barrier (well) material. The values of $U_{e0}$ and $U_{h0}$ are determined by the band alignments between bulk and QW material.

Once the parameters are defined we can split the Schrödinger equation in a barrier and well part,

$$\frac{\hbar^2}{2m_w}\partial_z^2\phi_{nw}(z) = \epsilon_n\phi_{nw}(z) \tag{2.15a}$$

$$\left(\frac{\hbar^2}{2m_b}\partial_z^2 + U_{n0}\right)\phi_{nb}(z) = \epsilon_n\phi_{nb}(z) \tag{2.15b}$$

which can be solved by imposing the correct set of boundary conditions, similarly to the traditional problem of a particle in a potential well. The main deviation from the standard treatment present in quantum mechanics textbooks arises because of the difference in particle mass between the different layers, i.e., $m_w \neq m_b$, and requires the use of the so-called Bastard boundary condition [89]

$$\frac{1}{m_w}\frac{\partial\phi_{nw}}{\partial z} = \frac{1}{m_b}\frac{\partial\phi_{nb}}{\partial z} \tag{2.16}$$

at the interfaces between barrier and well materials. This condition ensures that the particle flux is continuous across the interface between the two materials.

The Schrödinger equation presented in eq. 2.15 has to be solved numerically but some broad features can be generally stated. First, there is a finite number of eigenvalues, $j = 0, 1, \ldots, j_{max}$, all of which satisfy the condition $\epsilon_{nj} < \mathcal{U}_{n0}$. Second, the eigenfunctions have definite parity properties, being even for $j = 2k$ and odd for $j = 2k+1$. Furthermore, in the barrier region, the envelope functions decay exponentially with rate $\gamma_{nj} \propto \sqrt{\mathcal{U}_{n0} - \epsilon_{nj}}$. If we ignore the mixing between different bands, we are now able to write the full wave function of the QW's bound state $(nj\mathbf{k}_\perp)$

$$\psi_{nj\mathbf{k}_\perp}(\mathbf{r}_\perp, z) = e^{i\mathbf{k}_\perp \cdot \mathbf{r}_\perp} u_{n\mathbf{k}_{n0}}(\mathbf{r}_\perp)\, \phi_{nj}(z) \tag{2.17}$$

where $n$ is the band index, $j$ is the subband index, $\mathbf{k}_\perp$ is the in-plane wave vector and $u_{n\mathbf{k}_{n0}}(\mathbf{r}_\perp)$ is the Bloch function evaluated at the band extremum. An example of the numerical solutions of eq. 2.15 can be seen in fig. 2.1.

## 2.3 SECOND QUANTISATION FORMALISM AND EQUATIONS OF MOTION

In order to allow changes in the number of electrons and holes and to easily include the correct fermionic symmetry of the wave function, it is convenient to extend the description of the system to second quantisation. We start by introducing the field operators $\widehat{\Psi}^\dagger(\mathbf{r})$ and $\widehat{\Psi}(\mathbf{r})$, which describe respectively the creation and destruction of an electron at position $\mathbf{r}$. These quantum field operators can be expanded on the set of single-particle creation (annihilation) operators, $\widehat{c}^\dagger_{nj\mathbf{k}}$ ($\widehat{c}_{nj\mathbf{k}}$),

$$\widehat{\Psi}^\dagger(\mathbf{r}) = \sum_{nj\mathbf{k}} \psi^*_{nj\mathbf{k}}(\mathbf{r})\, \widehat{c}^\dagger_{nj\mathbf{k}} \tag{2.18}$$

where $\mathbf{k} = \mathbf{k}_\perp$ is the two-dimensional in-plane component of the wave vector and the coefficients, $\psi_{nj\mathbf{k}}(\mathbf{r}_\perp, z)$, are the first quantisation single-particle wave functions obtained in eq. 2.17. In order to obey the Pauli exclusion principle and, more generally, satisfy

the antisymmetric nature of the many-body wave function, the fermionic creation and annihilation operators have to satisfy the following algebraic relationships

$$\{ \hat{c}^{\dagger}_{njk}, \hat{c}^{\dagger}_{n'j'k'} \} = \{ \hat{c}_{njk}, \hat{c}_{n'j'k'} \} = 0 \tag{2.19a}$$

$$\{ \hat{c}_{njk}, \hat{c}^{\dagger}_{n'j'k'} \} = \delta_{nn'}\delta_{jj'}\delta_{kk'} \tag{2.19b}$$

where $\{ \cdot, \cdot \}$ is the anti-commutator, defined as

$$\{ \hat{A}, \hat{B} \} = \hat{A}\hat{B} + \hat{B}\hat{A}. \tag{2.20}$$

A defining characteristic of semiconductors is, as already mentioned in section 2.2, the presence of a gap, i.e., an energy region in which no states are located, lying around the Fermi energy. This means that, at least at zero temperature, the set of occupied (valence) and unoccupied (conduction) states are completely disjoint in energy. This is at the base of the electrically insulating nature of semiconductors, as a flow of current can only be established if enough energy is provided to promote carriers across the bandgap as opposed to metals where low energy excitations are available.

The presence of these two distinct sets of states results in a natural way of splitting carriers in two different categories, namely conduction band electrons and valence band holes. This comes from the realisation that the properties of an almost full band can be derived by looking at the smaller number of empty states rather than the larger number of full states. These holes, already introduced in section 2.2, can be treated as particles with the energy dispersion given in eq. 2.10 (taking the $-$ sign), positive mass, positive charge and opposite crystal momentum. This can be easily formulated in the language of second quantisation by considering the creation of an electron in the valence band as the annihilation of a hole and vice versa

$$\hat{c}^{\dagger}_{njk} \longrightarrow \hat{d}_{vj\bar{k}} \tag{2.21a}$$

$$\hat{c}_{njk} \longrightarrow \hat{d}^{\dagger}_{vj\bar{k}}, \tag{2.21b}$$

where $v$ is a discrete index labelling valence bands, $j$ is a subband index and $\overline{\mathbf{k}} = -\mathbf{k}$ is the crystal momentum of the hole. It can be easily shown using eqs. 2.19 and 2.21 that these new operators satisfy the same anticommutation relationship as the electron operators

$$\{\, \hat{d}^{\dagger}_{vj\mathbf{k}}, \hat{d}^{\dagger}_{v'j'\mathbf{k}'} \,\} = \{\, \hat{d}_{vj\mathbf{k}}, \hat{d}_{v'j'\mathbf{k}'} \,\} = 0 \tag{2.22a}$$

$$\{\, \hat{d}_{vj\mathbf{k}}, \hat{d}^{\dagger}_{v'j'\mathbf{k}'} \,\} = \delta_{vv'}\delta_{jj'}\delta_{\mathbf{k}\mathbf{k}'} \tag{2.22b}$$

allowing us to identify holes as fermionic quasi-particles that are created (annihilated) by the application of the $\hat{d}^{\dagger}_{vj\mathbf{k}}$ ($\hat{d}_{vj\mathbf{k}}$) operator. A further property is that conduction electron operators will anticommute with any valence hole operator as the anticommutator can be rewritten in terms of electron operators that will always have a different band index, $n$. In this new basis we can change the expansion of the quantum field operator to read

$$\hat{\Psi}^{\dagger}(\mathbf{r}) = \sum_{cj\mathbf{k}} \psi^{*}_{cj\mathbf{k}}(\mathbf{r})\, \hat{c}^{\dagger}_{cj\mathbf{k}} + \sum_{vj\mathbf{k}} \psi^{*}_{vj\mathbf{k}}(\mathbf{r})\, \hat{d}_{vj\overline{\mathbf{k}}}\,, \tag{2.23}$$

where $c$ is the discrete index which labels the conduction bands, $v$ the corresponding index for the valence bands and $\psi_{nj\mathbf{k}}(\mathbf{r})$ are kept as electronic wave functions.

In the second quantisation formalism combinations of creation and annihilation operators can be used to express any possible operator. In particular, we are at the moment mainly concerned with deriving expressions for one-particle operators, which are generally expressed as

$$\mathcal{O} = \sum_{i} o_i\,, \tag{2.24}$$

where $o_i$ is an ordinary single-particle operator acting on particle $i$ and the sum runs over all possible particles. We find a second quantisation representation for the single-particle operator, $o$, as

$$\hat{\mathcal{O}} = \sum_{nn'} \langle n|\, o\, |n'\rangle\, a^{\dagger}_{n} a_{n'} = \sum_{nn'} o_{nn'} a^{\dagger}_{n} a_{n'}\,, \tag{2.25}$$

where $|n\rangle$ is a complete basis. This takes on a particularly simple form when the basis is chosen such that the single-particle operator $o$ is diagonal,

$$\widehat{\mathcal{O}} = \sum_{\lambda} o_{\lambda} a_{\lambda}^{\dagger} a_{\lambda} \,, \tag{2.26}$$

where it is important to remark that the index $\lambda$ can be either discrete or continuous. Another important case, that of two-particle operators, will be treated in section 2.6 in the context of the Coulomb carrier-carrier interaction.

The last building block needed to compose the theoretical framework used in this thesis is the density matrix formalism. This provides a way to deal with mixed states, i.e., those in which an ensemble of physical systems is found to be in a mixture of different states, through a statistical description which bears some resemblances with classical statistical mechanics.

The core of the formalism resides in the definition of the density operator

$$\rho \equiv \sum_{i} w_i \, |\alpha^{(i)}\rangle \, \langle \alpha^{(i)}| \,, \tag{2.27}$$

where $w_i$ is the fraction of physical systems found in state $|\alpha^{(i)}\rangle$ and the sum runs over all populated states. As part of this definition, the states $|\alpha^{(i)}\rangle$ in which the system is found do not have to be orthogonal and the number of states included in the summation is not related to the dimensionality of the states. The fractional populations, however, have to satisfy the normalisation condition

$$\sum_{i} w_i = 1 \,. \tag{2.28}$$

With this definition, the density operator can be used to describe both pure and mixed states, as well as to calculate ensemble averages of operators,

$$\langle \mathcal{O} \rangle_{\rho} = \mathrm{Tr} \left[ \rho \mathcal{O} \right] \,. \tag{2.29}$$

It can also be convenient to define a corresponding density matrix, $\rho_{nn'}$, as the matrix elements of the density operator in a given base, which provides an explicit way of calculating the ensemble average

$$\langle \mathcal{O} \rangle_\rho = \sum_{nn'} \rho_{nn'} \langle n' | \mathcal{O} | n \rangle \ . \tag{2.30}$$

Within this formalism, we can further compute the dynamics of an ensemble average, $\langle \mathcal{O} \rangle_\rho (t)$, by tracking the time evolution of either the state, represented as a density operator $\rho(t)$, or the operator in the Heisenberg picture, $\mathcal{O}(t)$. In the former case the time evolution of the density operator, taken to be in the Schrödinger picture, is dictated by the von Neumann equation, while in the latter the operator $\mathcal{O}$ is evolved in time through the Heisenberg equation

$$i\hbar \frac{d\mathcal{O}(t)}{dt} = [\, \mathcal{O}(t), \mathcal{H} \,] \ , \tag{2.31}$$

where $\mathcal{H}$ is the Hamiltonian of the system and $[\,\cdot,\cdot\,]$ is the commutator

$$[\, \mathcal{A}, \mathcal{B} \,] = \mathcal{A}\mathcal{B} - \mathcal{B}\mathcal{A} \ . \tag{2.32}$$

Following the second approach, we can write out the equation of motion for a generic ensemble average $\left\langle \widehat{\mathcal{O}} \right\rangle_\rho (t)$ as

$$i\hbar \frac{d \langle \mathcal{O} \rangle_\rho (t)}{dt} = i\hbar \left\langle \frac{d\mathcal{O}(t)}{dt} \right\rangle_{\rho_0} = \langle [\, \mathcal{O}(t), \mathcal{H} \,] \rangle_{\rho_0} \tag{2.33}$$

where $\rho_0$ is used here to further stress that the density operator is static in time and will be dropped from now on for ease of reading.

## 2.4 INDEPENDENT ELECTRONS DYNAMICS

To describe the dynamics of electrons we have to define the Hamiltonian of the system. A first approximation to the Hamiltonian consists in describing the electrons independently of each other, while interactions between them can be later introduced through additional terms. So, we start by looking at the case of independent electrons in a semiconductor system. In the absence of any potential external to the semiconductor system we can write the second quantisation Hamiltonian for independent electrons as

$$\widehat{\mathcal{H}}_0 = \sum_{cjk} E^e_{cjk} \widehat{c}^\dagger_{cjk} \widehat{c}_{cjk} + \sum_{vjk} E^h_{vjk} \widehat{d}^\dagger_{vjk} \widehat{d}_{vjk} \,, \tag{2.34}$$

where we applied eq. 2.26 with $\widehat{c}^\dagger_{cjk}$ ($\widehat{d}^\dagger_{vjk}$) and $\widehat{c}_{cjk}$ ($\widehat{d}_{vjk}$) as the electron (hole) creation and annihilation operators for the eigenstates of the single-particle semiconductor Hamiltonian. The corresponding single-particle eigenvalues, $E^e_{cjk}$ and $E^h_{vjk}$, can be obtained from solving the time-independent problem at different levels of approximation. Here we will focus on the theory and results in the case of a structure with two parabolic bands, thus dropping the usage of the $c$ and $v$ indices, in which the confinement is accounted for through the EFA as it was outlined in section 2.2†.

The interaction between a quantum mechanical electron system and a classical electromagnetic field can be rigorously introduced through the use of minimal coupling. This consists in modifying the single-particle Hamiltonian in first quantisation to account for an additional energy term, $-e\varphi(\mathbf{r}, t)$, and a modified momentum for the electrons

$$\mathbf{p} \longrightarrow \mathbf{p} + e\mathbf{A}(\mathbf{r}, t) \,, \tag{2.35}$$

where $\varphi(\mathbf{r}, t)$ and $\mathbf{A}(\mathbf{r}, t)$ are respectively the scalar and vector potentials used to describe the electromagnetic field and $e$ is the elementary charge defined as the absolute value of the electron charge. By looking at a system in which the field variation hap-

† It is worth stressing that the same approach can be used to derive equations of motion starting from more sophisticated models with only small additional complications

pens on a scale much larger than the typical atomic scales it is possible to reframe the interaction in the electric dipole approximation. This results in the addition of a simple single-particle term to the Hamiltonian operator of the electronic system, eq. 2.34, whose first quantisation form reads

$$\mathcal{H}_{cl} = e\hat{\mathbf{r}} \cdot \mathbf{E}(\mathbf{R}, t) \,, \tag{2.36}$$

where $\hat{\mathbf{r}}$ is the position operator and $\mathbf{E}(\mathbf{R}, t)$ is the electric field. Here $\mathbf{R}$ is used to signify that the electric field varies on longer scales than the single-particle wave functions, $\psi_{njk}(\mathbf{r})$. Equation 2.25 can be applied to the carrier light interaction Hamiltonian eq. 2.36 to derive its second quantisation form,

$$\hat{\mathcal{H}}_{cl} = \sum_{njk} \sum_{n'j'k'} e\mathbf{E}(\mathbf{R}, t) \cdot \langle njk|\hat{\mathbf{r}}|n'j'k'\rangle \, \hat{c}^{\dagger}_{njk} \hat{c}_{n'j'k'} \,, \tag{2.37}$$

where we are using the same basis as in eq. 2.34 and $n, n' \in \{v, c\}$. Equation 2.37 can be further simplified by observing that the amount of momentum carried by the field can be neglected when compared to the typical values of crystal momentum of electrons in a solid, which is equivalent to neglecting all matrix elements of $\hat{\mathbf{r}}$ for which $\mathbf{k} \neq \mathbf{k}'$. Transforming it into the electron-hole representation while further unfolding $n$ and $n'$ over the two bands yields the final form for the interaction Hamiltonian between semiconductor carriers and electromagnetic fields

$$\hat{\mathcal{H}}_{cl} = e\mathbf{E}(\mathbf{r}, t) \cdot \sum_{\mathbf{k}} \sum_{jj'} \left[ \mu^{(c)}_{\mathbf{k}jj'} \hat{c}^{\dagger}_{\mathbf{k}j} \hat{c}_{\mathbf{k}j'} - \mu^{(v)}_{\mathbf{k}jj'} \hat{d}^{\dagger}_{\mathbf{k}j} \hat{d}_{\mathbf{k}j'} + \mu_{\mathbf{k}jj'} \hat{c}^{\dagger}_{\mathbf{k}j} \hat{d}^{\dagger}_{\bar{\mathbf{k}}j'} + \mu^{*}_{\mathbf{k}jj'} \hat{d}_{\bar{\mathbf{k}}j'} \hat{c}_{\mathbf{k}j} \right] \,, \tag{2.38}$$

where the intraband acceleration terms have been neglected and the $\mu$'s are the matrix element of the position operator, $\hat{\mathbf{r}}$, between the corresponding electronic states,

$$\mu^{(c)}_{\mathbf{k}jj'} = \int \mathbf{r} \psi^{*}_{cj\mathbf{k}}(\mathbf{r}) \, \psi_{cj'\mathbf{k}}(\mathbf{r}) \, d\mathbf{r} \tag{2.39a}$$

$$\mu^{(v)}_{\mathbf{k}jj'} = \int \mathbf{r} \psi^{*}_{vj'\bar{\mathbf{k}}}(\mathbf{r}) \, \psi_{vj\bar{\mathbf{k}}}(\mathbf{r}) \, d\mathbf{r} \tag{2.39b}$$

$$\mu_{\mathbf{k}jj'} = \int \mathbf{r} \psi^{*}_{cj\mathbf{k}}(\mathbf{r}) \, \psi_{vj'\mathbf{k}}(\mathbf{r}) \, d\mathbf{r} \,. \tag{2.39c}$$

By applying the EFA it can be shown that the interband dipole matrix elements, $\mu_{\mathbf{k}jj'}$, can be approximately calculated from the corresponding bulk value, $\mu_{\mathbf{k}}^{(cv)}$, as

$$\mu_{\mathbf{k}jj'} = \mu_{\mathbf{k}}^{(cv)} \int_{-\infty}^{\infty} \phi_{cj}^{*}(z)\, \phi_{vj'}(z)\, dz\,, \tag{2.40}$$

where $\phi_{cj}(z)$ ($\phi_{vj}(z)$) is the envelope function for the j-th conduction (valence) subband.† Analogously for the intersubband dipole matrix elements

$$\mu_{\mathbf{k}jj'}^{(c)} = \mathbf{u}_z \int_{-\infty}^{\infty} \phi_{cj}^{*}(z)\, z\phi_{cj'}(z)\, dz \tag{2.41a}$$

$$\mu_{\mathbf{k}jj'}^{(v)} = \mathbf{u}_z \int_{-\infty}^{\infty} \phi_{vj}^{*}(z)\, z\phi_{vj'}(z)\, dz\,, \tag{2.41b}$$

where $\mathbf{u}_z$ is the unit vector in the direction of positive $z$.

The dipole matrix elements are one of the main factors which determine the selection rules for optically induced transitions, in particular those that can be ascribed to real space symmetry properties of the wave functions. In the specific case of QWs, these selection rules reflect the general features of the confining potential through the envelope functions. In the common case of an inversion symmetric confinement the resulting envelope functions, $\phi_{nj}(z)$, have a definite parity and alternate between even and odd symmetry, cf. fig. 2.1a. Consequently, the interband dipole matrix elements given in eq. 2.40 forbid transitions between states j and j′ with different parity, i.e.,

$$\mu_{\mathbf{k}jj'} = 0 \qquad \text{if } j + j' = 2l,\ l \in \mathbb{N}\,. \tag{2.42}$$

Conversely eq. 2.41 shows that intersubband transitions, i.e., transitions between subbands coming from the same band, are only allowed between states with opposite parity.

† Note that $\phi_{cj}(z)$ and $\phi_{vj}(z)$ are eigenstates of different Hamiltonian operators and, as such, are not required to be orthogonal.

### 2.4.1 Equations of motion

Now that the Hamiltonian of the independent system is completely built from the sum of eqs. 2.34 and 2.38 it is possible to proceed following the theory outlined in section 2.3 to derive equations that describe the time evolution of operators in the system as well as ensemble averages within a density matrix approach. The main quantities of interest at the non-interacting level are all single-particle quantities and can be expressed in terms of single-particle density matrices. In particular, the basic dynamical variables required to describe the dynamics of the (photo-)excited semiconductor system are the occupations of single-particle states as well as the coherences between states that are coupled through the non-diagonal part of the Hamiltonian, eq. 2.38. These are all contained in the interband and intraband electron and hole density matrices, respectively,

$$p_{\mathbf{k}jj'} = \left\langle \hat{d}_{\overline{\mathbf{k}}j} \hat{c}_{\mathbf{k}j'} \right\rangle \tag{2.43a}$$

$$n^{e}_{\mathbf{k}jj'} = \left\langle \hat{c}^{\dagger}_{\mathbf{k}j} \hat{c}_{\mathbf{k}j'} \right\rangle \tag{2.43b}$$

$$n^{h}_{\mathbf{k}jj'} = \left\langle \hat{d}^{\dagger}_{\mathbf{k}j} \hat{d}_{\mathbf{k}j'} \right\rangle , \tag{2.43c}$$

where coherences between states with different crystal momentum, $\mathbf{k}$ and $\mathbf{k}'$, either intraband or interband, are taken to be identically zero.† The time evolution for these quantities can be derived by applying the Heisenberg equation to the electron and hole creation and annihilation operators, according to eq. 2.33, with $\hat{\mathcal{H}} = \hat{\mathcal{H}}_0 + \hat{\mathcal{H}}_{cl}$. The resulting commutators can be expanded and simplified by applying the relationship

† This comes as a consequence of the starting condition as well as the selection rules imposed by the dipole matrix elements contained in eq. 2.37, which, in turn, originate from the homogeneity of the system. Indeed off-diagonal terms in the crystal momentum index are needed to treat spatially inhomogeneous systems[92, 93].

outlined in eqs. 2.19 and 2.22†. The ensemble average taken with respect to the initial density operator, $\rho_0$, results in the closed set of differential equation

$$\begin{aligned} i\hbar\partial_t n^e_{\mathbf{k}jj'} &= \left(E^e_{\mathbf{k}j'} - E^e_{\mathbf{k}j}\right) n^e_{\mathbf{k}jj'} \\ &\quad + e\mathbf{E}(\mathbf{r},t)\cdot\sum_i \left(\mu_{\mathbf{k}j'i}p^*_{\mathbf{k}ij} - \mu^*_{\mathbf{k}ji}p_{\mathbf{k}ij'} + \mu^{(c)}_{\mathbf{k}j'i}n^e_{\mathbf{k}ji} - \mu^{(c)}_{\mathbf{k}ij}n^e_{\mathbf{k}ij'}\right) \end{aligned} \tag{2.45a}$$

$$\begin{aligned} i\hbar\partial_t n^h_{\mathbf{k}jj'} &= \left(E^h_{\mathbf{k}j'} - E^h_{\mathbf{k}j}\right) n^h_{\mathbf{k}jj'} \\ &\quad + e\mathbf{E}(\mathbf{r},t)\cdot\sum_i \left(\mu_{\bar{\mathbf{k}}ij'}p^*_{\bar{\mathbf{k}}ji} - \mu^*_{\bar{\mathbf{k}}ij}p_{\bar{\mathbf{k}}j'i} - \mu^{(v)}_{\mathbf{k}j'i}n^h_{\mathbf{k}ji} + \mu^{(v)}_{\mathbf{k}ij}n^h_{\mathbf{k}ij'}\right) \end{aligned} \tag{2.45b}$$

$$\begin{aligned} i\hbar\partial_t p_{\mathbf{k}jj'} &= \left(E^e_{\mathbf{k}j'} + E^h_{\bar{\mathbf{k}}j}\right) p_{\mathbf{k}jj'} \\ &\quad + e\mathbf{E}(\mathbf{r},t)\cdot\left(\mu_{\mathbf{k}j'j} - \sum_i \left(\mu_{\mathbf{k}j'i}n^h_{\bar{\mathbf{k}}ij} + \mu_{\mathbf{k}ij}n^e_{\mathbf{k}ij'} - \mu^{(c)}_{\mathbf{k}j'i}p_{\mathbf{k}ji} + \mu^{(v)}_{\bar{\mathbf{k}}ji}p_{\mathbf{k}ij'}\right)\right) \end{aligned} \tag{2.45c}$$

which are the non-interacting approximation to the Semiconductor Bloch equations in a two-band, multi-subband QW.

It is important to note that at this level of approximation, i.e., independent electrons with no intraband relaxation, eq. 2.45 describes a system that only depends on the wave vector in a parametric way. In essence, this describes a collection of independent multi-level systems, each one located at a specific point in $\mathbf{k}$-space and whose structure is dictated by the semiconductor band (and subband) structure at the given position in reciprocal space. In particular if a shallow well is used, in which only one or two subbands are present, one can imagine the system described by eq. 2.45 as being composed of a set of independent two- or four-level systems, which have been extensively studied in the literature.

Finally, observables have to be calculated, optionally in a time-dependent fashion, for several reasons like analysing the macroscopic behaviour of the system or comparing

† A more workable way of writing these Fermionic anticommutator relationships in the context of calculating commutators is

$$\begin{aligned} \hat{c}^\dagger_\alpha\hat{c}^\dagger_{\alpha'} &= -\hat{c}^\dagger_{\alpha'}\hat{c}^\dagger_\alpha \\ \hat{c}_\alpha\hat{c}_{\alpha'} &= -\hat{c}_{\alpha'}\hat{c}_\alpha \\ \hat{c}^\dagger_\alpha\hat{c}_{\alpha'} &= \delta_{\alpha\alpha'} - \hat{c}_{\alpha'}\hat{c}^\dagger_\alpha \end{aligned}$$

with experimental results. A macroscopic quantity that occupies a fundamental role in the theory is the induced sheet polarisation,

$$\mathbf{P}_2(\mathbf{r},t) = \sum_{jj'} \frac{1}{A} \sum_{\mathbf{k}} \left( \mu_{\mathbf{k}jj'} p^*_{\mathbf{k}j'j}(\mathbf{r},t) + \mu^*_{\mathbf{k}jj'} p_{\mathbf{k}j'j}(\mathbf{r},t) \right) \tag{2.46}$$

as it provides a way of linking the microscopic (quantum) carrier dynamics with the spatio-temporal description of the classical electromagnetic fields. In order to include the polarisation into Maxwell's equations, however, it is necessary to convert the two-dimensional quantity from eq. 2.46 into a proper bulk polarisation which requires accounting for the density of QWs which can be achieved with a multiplication by $N_{QW}/L$, where $N_{QW}$ is the number of QWs present over a length L.

## 2.5 NON-LINEAR RESPONSE OF FEW-LEVEL SYSTEMS

Non-linear optics can roughly be divided into non-resonant and resonant non-linearities. For non-resonant non-linearities a perturbative approach can be used to describe the main properties. Here, the non-linear polarisation is expanded as a series of non-linear susceptibilities, $\chi^{(i)}$,

$$\varepsilon_0^{-1} P(\omega) = \chi^{(1)} E(\omega) + \chi^{(2)} E^2(\omega) + \chi^{(3)} E^3(\omega) + \dots . \tag{2.47}$$

A more fundamental description of non-linearities is needed in the resonant case, where the response of the system is affected by the presence of excited carriers. The Bloch equations provide such an approach as polarisations and occupations are included on the same level. This allows a description of the optical response going beyond what can be achieved via a finite number of terms of the non-linear series expansion in eq. 2.47[94, Ch. 6]. An example of this is given by the saturation of absorption, shown by several

physical systems. This appears as a dependence of the absorption spectrum, $\alpha(\omega)$, on the intensity of the exciting field, I, as

$$\alpha(\omega; I) = \frac{\alpha_0(\omega)}{1 + I/I_s}, \tag{2.48}$$

where $\alpha_0(\omega)$ is the linear absorption coefficient and $I_s$ is a material dependent constant, called saturation intensity. Equation 2.48 can be expanded as a series,

$$\alpha(\omega; I) = \alpha_0(\omega)\left(1 - \frac{I}{I_s} + \left(\frac{I}{I_s}\right)^2 - \left(\frac{I}{I_s}\right)^3 + \dots\right), \tag{2.49}$$

which, however, only converges for $I < I_s$.

Nevertheless, it can be convenient to calculate the analytical form of some non-linear susceptibilities of a level system, as these can still be useful in some excitation regimes. Furthermore, it will make it easier to highlight where and how the non-linear optical response of a Bloch equation model goes beyond the power series description given in eq. 2.47.†

A few examples of systems that can be used to discuss the non-linear response of a QW are the two- and three-level systems shown in fig. 2.2. Part of the results presented in this thesis show how semiconductor systems can be used to generate harmonics of the excitation field. Even though semiconductors are quite complex, some basic features can still be understood by looking at the optical response of a simple two-level system. This can be generalised to the response of a multi-level, i.e., band resolved, system by performing an integral with the band-dependent density of states, but this is still limited to effects that can be represented as a single (or a few) non-linear susceptibility. The dynamical Bloch equation based model, on the other hand, is intrinsically providing results beyond what is possible with a power series expansion and is more easily extended to include additional phenomena as it will be shown in later sections.

† Only the final forms of the non-linear susceptibilities are given here, and only for specific configurations that are of interest to this work. The derivation, a more general formulation and an in-depth discussion can be found in Boyd [94, Chapters 3 and 6]

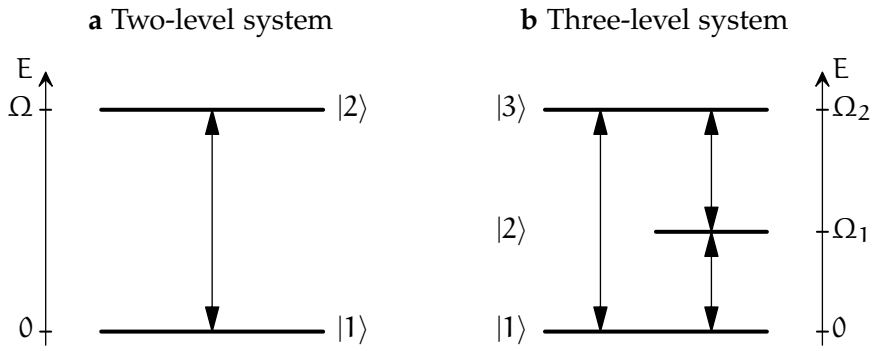


**Figure 2.2:** Sketch of two- and three-level systems. The configuration of the three-level system allows SHG if $\Omega_2 \approx 2\Omega_1$.

The first non-linear susceptibility that is present in a normal two-level system, as the one presented in fig. 2.2a, is the third order term, $\chi_2^{(3)}$, as all terms corresponding to an even power of the field are identically zero in systems that show an inversion symmetry. The third order susceptibility can be derived as

$$\chi_2^{(3)}(3\omega,\omega,\omega,\omega) = \frac{4\mu^4\Omega(\omega+i\gamma)\Delta\rho}{\omega\left((3\omega+i\gamma)^2-\Omega^2\right)\left((\omega+i\gamma)^2-\Omega^2\right)}, \tag{2.50}$$

where $\omega$ is the excitation frequency, $\Delta\rho = n_2 - n_1$ is the inversion, $\mu$ is the dipole matrix element between ground and excited state, $\hbar\Omega$ is the energy difference between the two levels, $\gamma = \frac{1}{T_2}$ is the coherence decay rate and all non-radiative processes are neglected. Of particular importance are the two terms in parentheses in the denominator of eq. 2.50, that show that the $\chi^{(3)}$ has resonances when the excitation occurs at one-third of the transition energy or at the transition energy, respectively.

### 2.5.1 Even order non-linearities

As it has already been mentioned, it can be shown that all terms of even order in the expansion from eq. 2.47 are identically zero in materials that show an inversion symmetry. It is however possible to modify the model presented to account for non-centrosymmetric systems like the case of a QW with an applied static electric field[95].

In such a system the wave functions of the different states, $\psi_{njk}(\mathbf{r})$, do not have a definite parity, i.e.,

$$\widehat{\mathcal{P}}\psi_{njk}(\mathbf{r}) \neq (-1)^{p}\psi_{njk}(\mathbf{r}) \ , \tag{2.51}$$

where $\widehat{\mathcal{P}}$ is the parity transformation operator. Under this assumption all the symmetry arguments made in section 2.4 are not valid any more and the optical selection rules for the system can only be obtained by explicitly evaluating the integrals in eq. 2.39. One further consequence of considering states without a definite parity, is that the expectation value of the position operator is in general different from zero, resulting in a permanent dipole moment for states in the conduction band,

$$\mathbf{M}^{(c)}_{kjj} = -e\boldsymbol{\mu}^{(c)}_{kaa} = -e\int \mathbf{r}\psi^{*}_{cjk}(\mathbf{r})\,\psi_{cjk}(\mathbf{r})\,d\mathbf{r} = -e\int \mathbf{r}\left|\psi_{cjk}(\mathbf{r})\right|^{2}d\mathbf{r} \tag{2.52}$$

and similarly for holes in the valence band.

We can perform a two-level approximation on a suitable system and thus distil out the effects of the permanent dipoles in their simplest form. The Hamiltonian of the system looks like

$$\begin{aligned}\widehat{\mathcal{H}}_{2'} &= E_1\hat{c}_1^{\dagger}\hat{c}_1 + E_2\hat{c}_2^{\dagger}\hat{c}_2 + e\mathbf{E}(\mathbf{r},t)\cdot\left(\boldsymbol{\mu}\hat{c}_2^{\dagger}\hat{c}_1 + \boldsymbol{\mu}\hat{c}_1^{\dagger}\hat{c}_2 + \boldsymbol{\mu}_1\hat{c}_1^{\dagger}\hat{c}_1 + \boldsymbol{\mu}_2\hat{c}_2^{\dagger}\hat{c}_2\right) \\ &= (E_1 + e\mathbf{E}(\mathbf{r},t)\cdot\boldsymbol{\mu}_1)\,\hat{c}_1^{\dagger}\hat{c}_1 + (E_2 + e\mathbf{E}(\mathbf{r},t)\cdot\boldsymbol{\mu}_2)\,\hat{c}_2^{\dagger}\hat{c}_2 + e\mathbf{E}(\mathbf{r},t)\cdot\boldsymbol{\mu}\left(\hat{c}_2^{\dagger}\hat{c}_1 + \hat{c}_1^{\dagger}\hat{c}_2\right) \ ,\end{aligned} \tag{2.53}$$

where $|1\rangle$ and $|2\rangle$ are the ground and excited states of the system, respectively. The terms composing eq. 2.53 have been grouped to highlight that the permanent dipole, together with the field, results in a (dynamic) shift of the energy levels. The resulting equations of motion read

$$i\hbar\partial_t n_1 = 2e\mathbf{E}(\mathbf{r},t)\cdot\boldsymbol{\mu}\mathcal{J}(p) \tag{2.54a}$$

$$i\hbar\partial_t n_2 = -2e\mathbf{E}(\mathbf{r},t)\cdot\boldsymbol{\mu}\mathcal{J}(p) \tag{2.54b}$$

$$i\hbar\partial_t p = (E_2 - E_1 + e\mathbf{E}(\mathbf{r},t)\cdot(\boldsymbol{\mu}_2 - \boldsymbol{\mu}_1))\,p + e\mathbf{E}(\mathbf{r},t)\cdot\boldsymbol{\mu}(n_1 - n_2) \ , \tag{2.54c}$$

where $\mathfrak{I}(z)$ is the function returning the imaginary part of $z$. In the centrosymmetric case, where $\mu_2 = 0$ and $\mu_1 = 0$, or in the more general case in which $\mu_2 = \mu_1$, eq. 2.54 reduces to the more traditional form of a normal two-level system. Following a similar process to what was done before, it is possible to calculate the non-linear susceptibilities of such a two-level system. It can be shown that the presence of the permanent dipole in the new Hamiltonian results in the addition of a term to the third order non-linear susceptibility presented in eq. 2.50,

$$\chi'(\omega) = \frac{4\mu^2\Omega\,|\mathbf{M}_2 - \mathbf{M}_1|^2\,\Delta\rho\left(i\gamma^3 + 3\gamma^2\omega + i\gamma\Omega^2 + 3\omega\left(\omega^2 + \Omega^2\right)\right)}{3\omega\left((\omega + i\gamma)^2 - \Omega^2\right)\left((3\omega + i\gamma)^2 - \Omega^2\right)\left((2\omega + i\gamma)^2 - \Omega^2\right)}\,, \tag{2.55}$$

where $\omega$ is the frequency of the exciting field and the response is observed at $3\omega$. Compared to the result in eq. 2.50 the last bracket in the denominator induces resonant behaviour at a new frequency, $\omega = \Omega/2$. This correction disappears as expected for centrosymmetric systems, in which $\mathbf{M}_2 = 0$ and $\mathbf{M}_1 = 0$, and the $\chi_2^{(3)}$ from eq. 2.50 is recovered.

Similarly, it is possible to calculate the even order terms of the expansion in eq. 2.47, in particular the second order term which is responsible for the process of SHG

$$\chi_{2'}^{(2)}(2\omega, \omega, \omega) = \frac{2i\mu^2\,|\mathbf{M}_2 - \mathbf{M}_1|\left(\gamma\left(\gamma - i\omega\right)\left(\gamma - 2i\omega\right) + \left(\gamma - 3i\omega\right)\Omega^2\right)\Delta\rho}{\omega\left((\omega + i\gamma)^2 - \Omega^2\right)\left((2\omega + i\gamma)^2 - \Omega^2\right)}\,, \tag{2.56}$$

where $\omega$ is the frequency of the exciting monochromatic field, and the response is observed at $2\omega$. The non-linear susceptibility in eq. 2.56 has resonances at the transition energy as well as at half of the transition frequency, corresponding to the two-photon resonance configuration. As expected this term depends on $\mathbf{M}_2 - \mathbf{M}_1$, so that it vanishes for centrosymmetric materials as well as for pairs of states that have the same dipole moment.

This second order non-linearity is significantly different from what can be obtained in the case of a centrosymmetric system where the process can only happen in a way that involves the presence of three levels. Such a system can be simplified as a three-level system analogous to the one presented in fig. 2.2b, which shows SHG, too. The second

order non-linear susceptibility of such a system in its most generic form is quite long and cumbersome, but a simpler form can be derived under the assumption that the levels are equally spaced in energy, i.e., $\Omega_2 \approx 2\Omega_1 \equiv 2\Omega$,

$$\chi_3^{(2)}(2\omega,\omega,\omega) = \frac{12 d_1 d_2 \mu \Omega^2 \left(6\omega^2 + 7i\gamma\omega - 2\gamma^2 - 2\Omega^2\right)(n_0 - 2n_1 + n_2)}{\left((\omega+i\gamma)^2 - \Omega^2\right)\left((2\omega+i\gamma)^2 - \Omega^2\right)\left((2\omega+i\gamma)^2 - 4\Omega^2\right)}\,, \quad (2.57)$$

where $\omega$ is the excitation frequency, $d_1$ and $d_2$ are the dipole matrix elements for the $|1\rangle \rightarrow |2\rangle$ and $|2\rangle \rightarrow |3\rangle$ transitions respectively, $\mu$ is the dipole matrix element for the $|1\rangle \rightarrow |3\rangle$ transition and $\gamma$ is the dephasing rate, assumed to be the same for all transitions.

## 2.6 INTERACTING ELECTRONS DYNAMICS

Carriers in semiconductors are interacting particles and their interaction can have a strong influence on the optical properties of the semiconductor, especially in the low-excitation and low-density regime. We thus have to include those interaction effects in our description of the optical response of 2D semiconductor structures.

Due to their charged nature the strongest interaction between carriers comes from the Coulomb interaction. This is a two-body interaction potential which only depends on the charge and distance between the two particles, i.e., $V(\mathbf{r}_1, \mathbf{r}_2) = V(|\mathbf{r}_1 - \mathbf{r}_2|)$. In a quantum mechanical formalism the electrons are delocalised objects, described through a probability density $\rho(\mathbf{r})$, and their electrostatic interaction can be described via the potential energy term

$$V[\rho_1, \rho_2] = \frac{e^2}{4\pi\varepsilon_0} \int\int \frac{\rho_1(\mathbf{r}_1)\,\rho_2(\mathbf{r}_2)}{|\mathbf{r}_1 - \mathbf{r}_2|} d\mathbf{r}_1 d\mathbf{r}_2\,. \quad (2.58)$$

This is the generalisation of the Coulomb interaction between two point particles

$$V_0(\mathbf{r}_1, \mathbf{r}_2) = V_0(r = |\mathbf{r}_1 - \mathbf{r}_2|) = \frac{1}{4\pi\varepsilon_0} \frac{q_1 q_2}{|\mathbf{r}_1 - \mathbf{r}_2|}\,, \quad (2.59)$$

to the charge density of an electron, $-e\rho(\mathbf{r})$.

The Coulomb potential is added to the Hamiltonian from section 2.4 as

$$\widehat{\mathcal{H}}_{cc} = \frac{1}{2}\int\int \widehat{\rho}(\mathbf{r}_1)\,\widehat{\rho}(\mathbf{r}_2)\,V_0(|\mathbf{r}_1-\mathbf{r}_2|)\,d\mathbf{r}_1 d\mathbf{r}_2\,, \tag{2.60}$$

where the $\frac{1}{2}$ avoids double counting of the interaction energy. This expression closely resembles the definition given in eq. 2.58 with the difference that $\widehat{\rho}$ is now the density operator of the carrier system,

$$\widehat{\rho}(\mathbf{r}) = \widehat{\Psi}^{\dagger}(\mathbf{r})\,\widehat{\Psi}(\mathbf{r})\,, \tag{2.61}$$

defined in terms of the field operator, $\widehat{\Psi}$. By inserting the expansion from eq. 2.18 it is possible to rewrite the Coulomb potential in the basis of the single-particle states characterised by the compound quantum number $\alpha = nj\mathbf{k}$ as

$$\widehat{\mathcal{H}}_{cc} = \frac{1}{2}\sum_{\substack{\alpha_1,\alpha_2\\ \alpha_3,\alpha_4}} V_{\alpha_1\alpha_2\alpha_3\alpha_4}\,\widehat{c}^{\dagger}_{\alpha_1}\widehat{c}^{\dagger}_{\alpha_2}\widehat{c}_{\alpha_3}\widehat{c}_{\alpha_4} \tag{2.62}$$

where the matrix elements $V_{\alpha_1\alpha_2\alpha_3\alpha_4}$ are defined as

$$V_{\alpha_1\alpha_2\alpha_3\alpha_4} = \int\int \psi^{*}_{\alpha_1}(\mathbf{r}_1)\,\psi^{*}_{\alpha_2}(\mathbf{r}_2)\,V_0(|\mathbf{r}_1-\mathbf{r}_2|)\,\psi_{\alpha_3}(\mathbf{r}_2)\,\psi_{\alpha_4}(\mathbf{r}_1)\,d\mathbf{r}_1 d\mathbf{r}_2\,. \tag{2.63}$$

Within the EFA it is possible to rewrite the integrals within eq. 2.63 in the two independent subspaces $\mathbf{r}_\perp$ and $\mathbf{s}$. By applying the same length-scale argument underlying the whole EFA it is then possible to unlink the integrals in the two subspaces,

$$V_{\alpha_1\alpha_2\alpha_3\alpha_4} = \widetilde{V}_{\beta_1\beta_2\beta_3\beta_4}F_{\delta_1\delta_2\delta_3\delta_4}\,, \tag{2.64}$$

where $\beta = n\mathbf{k}$ is the compound index characterising the free part of the wave function, $e^{i\mathbf{k}_\perp\cdot\mathbf{r}_\perp}u_{n\mathbf{k}_{n0}}(\mathbf{r}_\perp, z)$, and $\delta = nj$ is the one characterising the envelope function, $\phi_{nj}(\mathbf{s})$.

It is further possible to interpret $\widetilde{V}_{\beta_1\beta_2\beta_3\beta_4}$ as a two-dimensional Fourier transform, such that

$$\widetilde{V}_{\beta_1\beta_2\beta_3\beta_4} = \widetilde{V}(q) = \frac{e^2}{2\varepsilon_0 A}\frac{1}{q}\,, \tag{2.65}$$

with the exchanged momentum, $q = |\mathbf{q}| = |\mathbf{k}_3 - \mathbf{k}_2| = |\mathbf{k}_4 - \mathbf{k}_1|$. The remaining part constitutes the form factors,

$$F_{\delta_1\delta_2\delta_3\delta_4}(q) = \int\int \phi^*_{\delta_1}(\mathbf{s}_1)\,\phi^*_{\delta_2}(\mathbf{s}_2)\,e^{-q|\mathbf{s}_1-\mathbf{s}_2|}\phi_{\delta_3}(\mathbf{s}_2)\,\phi_{\delta_4}(\mathbf{s}_1)\,d\mathbf{s}_1 d\mathbf{s}_2 \tag{2.66}$$

which only depend on the slowly varying envelopes, $\phi_\delta(\mathbf{s})$.

This can be further adapted to the formalism presented in section 2.3 by casting it into the electron-hole picture, i.e., explicitly splitting summations over band index in eq. 2.62 into separate terms,

$$\sum_\alpha = \sum_{njk} = \sum_{jk}\left(\sum_c + \sum_v\right)\,, \tag{2.67}$$

where $c$ and $v$ respectively run on conduction and valence bands, and replacing valence band electronic operators with hole operators following the rules outlined in eq. 2.21. This process results in $2^4 = 16$ terms, each composed of a product of four fermionic operators. These can be grouped into different categories depending on the nature of the four operators, which represent different types of physical processes. Terms including an odd number of electron (or hole) operators, representing processes like Auger recombination, are neglected as are those that change the number of electrons (or holes) as they require the exchange of a large amount of energy. Terms representing interband exchange interaction are neglected as well. After reordering of the operators

to achieve normal ordering the remaining four operator terms compose the commonly used Coulomb interaction Hamiltonian

$$\begin{aligned}\widehat{\mathcal{H}}_{cc} = &\frac{1}{2}\sum_{\mathbf{k}\mathbf{k}'\mathbf{q}}\sum_{\substack{\mu_1,\mu_2\\ \mu_3,\mu_4}} V_{\mu_1\mu_2\mu_3\mu_4}(q)\,\widehat{c}^{\dagger}_{\mu_1\mathbf{k}_1+\mathbf{q}}\widehat{c}^{\dagger}_{\mu_2\mathbf{k}_2-\mathbf{q}}\widehat{c}_{\mu_3\mathbf{k}_2}\widehat{c}_{\mu_4\mathbf{k}_1}\\ &+\frac{1}{2}\sum_{\mathbf{k}\mathbf{k}'\mathbf{q}}\sum_{\substack{\nu_1,\nu_2\\ \nu_3,\nu_4}} V_{\nu_1\nu_2\nu_3\nu_4}(q)\,\widehat{d}^{\dagger}_{\nu_1\mathbf{k}_1+\mathbf{q}}\widehat{d}^{\dagger}_{\nu_2\mathbf{k}_2-\mathbf{q}}\widehat{d}_{\nu_3\mathbf{k}_2}\widehat{d}_{\nu_4\mathbf{k}_1}\\ &-\sum_{\mathbf{k}\mathbf{k}'\mathbf{q}}\sum_{\substack{\mu_1,\mu_2\\ \nu_1,\nu_2}} V_{\mu_1\mu_2\nu_1\nu_2}(q)\,\widehat{c}^{\dagger}_{\mu_1\mathbf{k}_1+\mathbf{q}}\widehat{d}^{\dagger}_{\nu_1\mathbf{k}_2-\mathbf{q}}\widehat{d}_{\nu_2\mathbf{k}_2}\widehat{c}_{\mu_2\mathbf{k}_1}\,,\end{aligned} \tag{2.68}$$

where $\mu$ and $\nu$ are band-subband compound indices for conduction and valence bands, respectively. The effective single-particle, i.e., two operators, terms that emerge as a consequence of reordering operators to achieve normal ordering are assumed to be included in $\widehat{\mathcal{H}}_0$. In eq. 2.68 it becomes apparent how the absence of an electron in the valence band, i.e., a hole, behaves as a positively charged particle which feels an attractive force towards negatively charged particles. This results in the minus sign preceding the third term of eq. 2.68 as opposed to the positive sign of the first two terms which represent repulsion among particles with the same charge (electrons and holes, respectively).

The Hamiltonian in eq. 2.68 can be used to calculate the effects of the carrier-carrier interaction on the dynamics of the system. In particular this will introduce new terms in the equation of motion of the single-particle quantities, introduced in section 2.4, which will depend on ensemble averages of four operator terms. The equations of motion of these quantities will in turn depend on terms containing six operators and so on, resulting in an infinite hierarchy of equations of motion for density matrices with an increasing number of particles. In order to obtain results for the carrier dynamics it is possible to truncate this hierarchy at different levels by approximately factorising terms containing ensemble averages of a higher number of operators into combinations of lower order terms. An alternative approach, the so-called *dynamics-controlled truncation*, was introduced by Axt and Stahl [96] and consists in an expansion over powers of the exciting field. In cases in which the Hamiltonian conserves the total number of carriers

and the initial state is taken to be the vacuum of electron-hole pairs, the hierarchy can be rigorously truncated to any order of the driving field[96, 97].

The lower possible order of approximation of the carrier-carrier Hamiltonian, known as Hartree-Fock (HF) or mean field approximation, consists into factorising ensemble averages of four operator terms into products of two operator terms,

$$\begin{aligned}\left\langle \widehat{c}^{\dagger}_{\mu_1\mathbf{k}_1+\mathbf{q}}\widehat{c}^{\dagger}_{\mu_2\mathbf{k}_2-\mathbf{q}}\widehat{c}_{\mu_3\mathbf{k}_2}\widehat{c}_{\mu_4\mathbf{k}_1}\right\rangle \approx &\left\langle \widehat{c}^{\dagger}_{\mu_1\mathbf{k}_1+\mathbf{q}}\widehat{c}_{\mu_4\mathbf{k}_1}\right\rangle \left\langle \widehat{c}^{\dagger}_{\mu_2\mathbf{k}_2-\mathbf{q}}\widehat{c}_{\mu_3\mathbf{k}_2}\right\rangle \delta_{\mathbf{q},0} \\ &- \left\langle \widehat{c}^{\dagger}_{\mu_1\mathbf{k}_1+\mathbf{q}}\widehat{c}_{\mu_3\mathbf{k}_2}\right\rangle \left\langle \widehat{c}^{\dagger}_{\mu_2\mathbf{k}_2-\mathbf{q}}\widehat{c}_{\mu_4\mathbf{k}_1}\right\rangle \delta_{\mathbf{k}_1+\mathbf{q},\mathbf{k}_2} \ ,\end{aligned} \tag{2.69}$$

where the $\delta$'s have been introduced as only terms that are diagonal in $\mathbf{k}$ have contributions from $\widehat{\mathcal{H}}_0 + \widehat{\mathcal{H}}_{cl}$ and are thus assumed to be dominant over off-diagonal $\mathbf{k}$ terms. This approximation can be applied while deriving equations of motion from a Hamiltonian including the four operator terms presented in eq. 2.68 or, in a completely equivalent way, used to build an effective Hartree-Fock Hamiltonian in which every term contains only two operators. At this level of approximation the corrections induced by carrier-carrier interaction can be easily included in the equations of motion presented in eq. 2.45 via a renormalisation of the band structure and of the instantaneous Rabi frequency $\hbar\Omega_{\mathbf{k}jj'}(t) = e\mathbf{E}(\mathbf{r},t)\cdot\boldsymbol{\mu}_{\mathbf{k}jj'}$

$$\mathrm{E}^{e}_{\mathbf{k}j} \longrightarrow \widetilde{\mathrm{E}}^{e}_{\mathbf{k}jj'} = \mathrm{E}^{e}_{\mathbf{k}j}\delta_{j,j'} + \delta\mathrm{E}^{e}_{\mathbf{k}jj'}(t) \tag{2.70a}$$

$$\mathrm{E}^{h}_{\mathbf{k}j} \longrightarrow \widetilde{\mathrm{E}}^{h}_{\mathbf{k}jj'} = \mathrm{E}^{h}_{\mathbf{k}j}\delta_{j,j'} + \delta\mathrm{E}^{h}_{\mathbf{k}jj'}(t) \tag{2.70b}$$

$$\hbar\Omega_{\mathbf{k}jj'}(t) \longrightarrow \hbar\widetilde{\Omega}_{\mathbf{k}jj'}(t) = \Omega_{\mathbf{k}jj'}(t) - \Delta_{\mathbf{k}jj'}(t) \ . \tag{2.70c}$$

Although the structure of the equations of motion is not modified, the dynamical correcting terms included in eq. 2.70 have the effect of coupling the dynamics of different $k$ states via the Coulomb matrix elements introduced in eq. 2.64

$$\delta E^{e}_{\mathbf{k}jj'}(t) = -\sum_{\mathbf{k}'}\sum_{ii'} V^{ee}_{jij'i'}\left(\left|\mathbf{k}-\mathbf{k}'\right|\right) n^{e}_{\mathbf{k}'ii'}(t) \tag{2.71}$$

$$\delta E^{h}_{\mathbf{k}jj'}(t) = -\sum_{\mathbf{k}'}\sum_{ii'} V^{hh}_{i'j'ij}\left(\left|\mathbf{k}-\mathbf{k}'\right|\right) n^{h}_{\mathbf{k}'ii'}(t) \tag{2.72}$$

$$\Delta_{\mathbf{k}jj'}(t) = -\sum_{\mathbf{k}'}\sum_{ii'} V^{eh}_{ji'j'i}\left(\left|\mathbf{k}-\mathbf{k}'\right|\right) p_{\mathbf{k}'ii'}(t)\ , \tag{2.73}$$

where the time dependence has been written explicitly to further stress how this effect is dynamical in nature.

To better understand the meaning of these terms it is convenient to look at a system in which only one electron and one hole subband are present. In such a system the electron and hole self-energies assume the simpler form

$$\delta E^{e}_{\mathbf{k}}(t) = -\sum_{\mathbf{k}'} V^{ee}\left(\left|\mathbf{k}-\mathbf{k}'\right|\right) n^{e}_{\mathbf{k}'}(t) \tag{2.74a}$$

$$\delta E^{h}_{\mathbf{k}}(t) = -\sum_{\mathbf{k}'} V^{hh}\left(\left|\mathbf{k}-\mathbf{k}'\right|\right) n^{h}_{\mathbf{k}'}(t)\ , \tag{2.74b}$$

which results in a downward shift in conduction and valence band energies.† The resulting $\mathbf{k}$-resolved reduction of transition energies induces an overall redshift of the absorption spectrum whose precise characteristics are affected by the number and distribution of excited carriers, $n^{e}_{\mathbf{k}}(t)$ and $n^{h}_{\mathbf{k}}(t)$. The modification of the Rabi frequency due to the electron-hole attraction,

$$\hbar\widetilde{\Omega}_{\mathbf{k}}(t) = e\mathbf{E}(\mathbf{r},t)\cdot\boldsymbol{\mu}_{\mathbf{k}} + \sum_{\mathbf{k}'} V^{eh}\left(\left|\mathbf{k}-\mathbf{k}'\right|\right) p_{\mathbf{k}'}(t)\ , \tag{2.75}$$

is responsible for the appearance of resonances in the absorption spectrum located within the bandgap. These are the excitonic resonances[6, 7, 10].

† From eqs. 2.64 to 2.66 it can be deduced that the Coulomb matrix elements are positive, while the definition of the occupations $n^{e/h}$ implies that they are non-negative.

In contrast to what happens in the HF approximation, the inclusion of further orders of the Coulomb interaction results in the appearance of new dynamical variables and thus in the increase of the number of simultaneous differential equations that need to be solved. In the next step following the mean-field approximation, one has to consider the time evolution of ensemble averages of terms containing four operators, e.g., $\left\langle \hat{c}_1^\dagger \hat{c}_2^\dagger \hat{c}_3 \hat{c}_4 \right\rangle (t)$. The dynamics of such terms can be derived, similarly to what was shown previously, through the Heisenberg equation using the Hamiltonian defined by eqs. 2.34, 2.38 and 2.68. As expected, this will result in the appearance of ensemble averages of terms containing the product of six operators which will need to be factorised into terms of lower order to obtain a closed set of update equations. By choosing the specific approximations, one determines which higher order Coulomb processes, e.g., screening, carrier relaxation, polarisation dephasing..., are included in the dynamics[93]. Some of these processes are presented in sections 2.6.1 to 2.6.3, along with explanations on how they can be phenomenologically included at the HF level, thus reducing the need to extend the dynamical treatment to higher order correlations.

### 2.6.1 Intraband carrier relaxation

One of the most apparent effects of the Coulomb interaction is the introduction of scattering events between carriers, which can be described in terms of a Boltzmann equation for electrons and holes. A sketch of the derivation is presented here following the treatment in Chow, Koch, and Sargent [6], but a more in-depth treatment and alternative derivations can be found in several reference books like Haug and Koch [10] and Rossi [11]. First the variation between the ensemble average of a four operators term and its HF approximation is defined as

$$\delta K^{e}_{\mathbf{k},\mathbf{k}'-\mathbf{q},\mathbf{k}-\mathbf{q},\mathbf{k}'} = \left\langle \hat{c}_{\mathbf{k}}^\dagger \hat{c}_{\mathbf{k}'-\mathbf{q}}^\dagger \hat{c}_{\mathbf{k}-\mathbf{q}} \hat{c}_{\mathbf{k}'} \right\rangle - \left\langle \hat{c}_{\mathbf{k}}^\dagger \hat{c}_{\mathbf{k}} \right\rangle \left\langle \hat{c}_{\mathbf{k}-\mathbf{q}}^\dagger \hat{c}_{\mathbf{k}-\mathbf{q}} \right\rangle \delta_{\mathbf{k},\mathbf{k}'} \,, \tag{2.76}$$

where the Hartree term, $\left\langle \widehat{c}^{\dagger}_{\mathbf{k}} \widehat{c}_{\mathbf{k}} \right\rangle \left\langle \widehat{c}^{\dagger}_{\mathbf{k}'} \widehat{c}_{\mathbf{k}'} \right\rangle \delta_{\mathbf{q},0}$, has been neglected. The differential equation responsible for the time evolution of this variation can be formally integrated under the assumption that the Coulomb contribution is slowly varying

$$\delta K^{e}_{\mathbf{k},\mathbf{k}'-\mathbf{q},\mathbf{k}-\mathbf{q},\mathbf{k}'}(t) \approx \frac{\partial_t \delta K^{e}_{\mathbf{k},\mathbf{k}'-\mathbf{q},\mathbf{k}-\mathbf{q},\mathbf{k}'}\big|_{cc}}{i\Delta\epsilon_{e\mathbf{k}\mathbf{k}'\mathbf{q}}/\hbar - \gamma} \,. \tag{2.77}$$

where $\gamma$ is a phenomenological decay constant, $\Delta\epsilon_{e\mathbf{k}\mathbf{k}'\mathbf{q}} = E^{e}_{\mathbf{k}} + E^{e}_{\mathbf{k}'-\mathbf{q}} - E^{e}_{\mathbf{k}-\mathbf{q}} - E^{e}_{\mathbf{k}'}$ and

$$i\hbar\partial_t \delta K^{e}_{\mathbf{k},\mathbf{k}'-\mathbf{q},\mathbf{k}-\mathbf{q},\mathbf{k}'}\Big|_{cc} = \left\langle [\, \widehat{\mathcal{H}}_{cc}, \widehat{c}^{\dagger}_{\mathbf{k}} \widehat{c}^{\dagger}_{\mathbf{k}'-\mathbf{q}} \widehat{c}_{\mathbf{k}-\mathbf{q}} \widehat{c}_{\mathbf{k}'} \,] \right\rangle \,. \tag{2.78}$$

Next all resulting ensemble averages of six and four operators are factorised into single-particle density matrices and the result has the form of a Boltzmann equation,

$$\partial_t n^{e}_{\mathbf{k}}\Big|_{coll} = -n^{e}_{\mathbf{k}} \Gamma^{out}_{e\mathbf{k}}\left[n^{e}, n^{h}\right] + \left(1 - n^{e}_{\mathbf{k}}\right) \Gamma^{in}_{e\mathbf{k}}\left[n^{e}, n^{h}\right] \,, \tag{2.79}$$

where the $\Gamma^{in}_{e\mathbf{k}}\left[n^{e}, n^{h}\right]$ and $\Gamma^{out}_{e\mathbf{k}}\left[n^{e}, n^{h}\right]$ rates are built from the sum of all possible *in* and *out* scattering events preserving energy and momentum. If the carrier distributions are sufficiently close to quasi-equilibrium Fermi-Dirac distributions, eq. 2.79 can be approximated via the relaxation time approximation

$$\partial_t n^{e}_{\mathbf{k}}\Big|_{coll} \approx -\gamma^{e}_{\mathbf{k}}\left[f^{e}, f^{h}\right]\left(n^{e}_{\mathbf{k}} - f^{e}_{\mathbf{k}}\right) \,, \tag{2.80}$$

where $\gamma^{e}_{\mathbf{k}}\left[f^{e}, f^{h}\right] = \Gamma^{out}_{e\mathbf{k}}\left[n^{e}, n^{h}\right] + \Gamma^{in}_{e\mathbf{k}}\left[n^{e}, n^{h}\right]$ and $f^{e}_{\mathbf{k}}$ ($f^{h}_{\mathbf{k}}$) is the electron (hole) quasi-equilibrium Fermi-Dirac distribution corresponding to the same number of carriers and temperature of $n^{e}_{\mathbf{k}}(t)$ ($n^{h}_{\mathbf{k}}(t)$). This approximation with a $\mathbf{k}$ dependent scattering rate fails to preserve the total number of carriers, so that one often sets $\gamma^{e}_{\mathbf{k}}\left[f^{e}, f^{h}\right] = \gamma^{e}_{\mathbf{k}_0}\left[f^{e}, f^{h}\right]$ which instead preserves the number of carriers†.

† In order to avoid a dynamical calculation of these rates, it is possible to calculate the values in advance as the table $\gamma^{e}_{i,j} = \gamma^{e}(i\Delta k, j\Delta N)$, where a closed system is assumed, such that the same total numbers of electrons and holes are excited, see e.g. Böhringer and Hess [31, 32]

### 2.6.2 Polarisation dephasing

The presence of the Coulomb induced scattering processes outlined in the previous subsection also contributes to the loss of phase coherence between different states. Together with the carrier-carrier interaction, several other coherent and incoherent processes contribute to the phenomenon known as *dephasing*. This is commonly introduced via the relaxation time approximation,

$$\partial_t p_\alpha \Big|_{\text{relax}} = -\gamma_\alpha^p \left[n^e, n^h\right] p_\alpha \,, \tag{2.81}$$

where $\gamma_\alpha^p \left[n^e, n^h\right]$ is the dephasing rate which depends in a functional sense on the electron and hole distributions. A value for this parameter can either be derived from higher order correlations, see e.g., Chow, Koch, and Sargent [6], or phenomenologically set to a value that reproduces experimental results. In the latter case it is common to assume the dephasing rate to be the same for all possible transitions, $\gamma_\alpha^p \left[n^e, n^h\right] = \gamma^p$.

### 2.6.3 Screening of the Coulomb interaction

Since the conduction electrons (and valence holes) in a semiconductor are only loosely bound to atoms, the electron-hole system shares a lot of similarities with a plasma. In particular in such a system the particles will rearrange themselves in order to reduce the electric field produced by a particle, resulting in an effective screening of the interaction. In the case of Coulomb interaction, this has the added benefit of removing the divergence which appears in the calculation of the scattering integrals when the exchanged momentum, $\mathbf{q}$, tends to zero. This effect emerges self-consistently from a treatment of interaction up to second order similar to the one discussed in section 2.6.1, where the six operator terms arising from eq. 2.78 are factorised in all possible combinations of lower order terms, i.e., one and two particle density matrices [93, 98–100]. The resulting equation of motion for the two particle correlation, $\delta K^e_{\mathbf{k},\mathbf{k}',\mathbf{k}'+\mathbf{q},\mathbf{k}-\mathbf{q}}(t)$, can be written

as the sum of five terms, $S_i$, which represent different physical phenomena. The second, third and fifth terms, respectively represent the screening of the Coulomb potential with increasing degrees of accuracy, starting from random-phase approximation (RPA) and further correcting it with exchange terms, that are needed to obtain the correct symmetry for the two particle correlation, and vertex corrections.

A more phenomenological approach to include the effects of screening within the RPA consists of replacing the momentum space component of the bare Coulomb potential, $\widetilde{V}(q)$, used in section 2.6 with an effective screened potential,

$$\widetilde{W}(\mathbf{q},\omega) = \frac{\widetilde{V}(q)}{\epsilon(\mathbf{q},\omega)}\,, \tag{2.82}$$

where $\epsilon(\mathbf{q},\omega)$ is the electron-hole plasma dielectric function. Within a two-band approximation and using the RPA the spatial and spectral dispersions of the longitudinal dielectric function are given by the Lindhard formula

$$\epsilon(q,\omega) = 1 - \widetilde{V}(q) \sum_{\substack{\alpha=e,h \\ j_\alpha \mathbf{k}}} \frac{n^{\alpha}_{j_\alpha j_\alpha \mathbf{k}-\mathbf{q}} - n^{\alpha}_{j_\alpha j_\alpha \mathbf{k}}}{\hbar(\omega+i\delta) + E^{\alpha}_{j_\alpha \mathbf{k}-\mathbf{q}} - E^{\alpha}_{j_\alpha \mathbf{k}}}\,, \tag{2.83}$$

which describes a complex retarded dielectric function. In the *plasmon-pole* approximation, the continuum of electron-hole excitations represented by poles in eq. 2.83 is replaced by a single effective plasmon pole,

$$\frac{1}{\epsilon(\omega)} = 1 + \frac{\omega_{pl}^2}{(\omega+i\delta)^2 - \omega_q^2}\,, \tag{2.84}$$

with the two-dimensional plasma frequency[6],

$$\omega_{pl}^2 = \frac{e^2 N L}{2\varepsilon_0 \varepsilon m^*} q\,, \tag{2.85}$$

with the QW thickness, L. Equation 2.84 has the same structure as the Drude (classical) result in the long-wavelength approximation except for the introduction of the effective plasmon frequency,

$$\omega_q^2 = \omega_{pl}^2 \left(1 + \frac{q}{\kappa}\right) + \frac{C}{4}\left(\frac{\hbar q^2}{2m^*}\right)^2 , \tag{2.86}$$

where $m^*$ is the electron-hole reduced mass, N is the sheet density and C is a numerical constant which is usually taken between 1 and 4 [6, 101]. In the quasi-equilibrium limit, the inverse screening length is

$$\kappa = \frac{e^2}{2\varepsilon_0 \varepsilon \pi \hbar^2} \sum_{\substack{\alpha = e,h \\ j_\alpha}} m_\alpha f^\alpha_{j_\alpha j_\alpha \mathbf{k}} \Big|_{\mathbf{k}=\mathbf{0}} , \tag{2.87}$$

where $f^\alpha_{j_\alpha j_\alpha \mathbf{k}}$ is the quasi-equilibrium distribution. In the static limit, $\omega \to 0$, the screened interaction potential is

$$W_{\alpha_1\alpha_2\alpha_3\alpha_4} = \widetilde{W}(q)\, F_{\delta_1\delta_2\delta_3\delta_4} , \tag{2.88}$$

with

$$\widetilde{W}(q) = \widetilde{V}(q)\left(1 - \frac{\omega_{pl}^2}{\omega_q^2}\right) . \tag{2.89}$$

The screened interaction potential, $W_{\alpha_1\alpha_2\alpha_3\alpha_4}$, can then be used as a replacement for the bare Coulomb potential in the HF correction terms presented in eqs. 2.71 to 2.73. A further term is introduced in the single-particle energy as a consequence of the screening of the interaction, the Coulomb hole self-energy,

$$\delta E^{CH} = \sum_{\mathbf{q}\neq 0} \left(W(q) - V(q)\right) < 0 , \tag{2.90}$$

which provides a correction for the effective inclusion of Coulomb interaction in the equilibrium single-particle band structure. As a consequence the hole single-particle energy within the HF approximation of a screened Coulomb potential has the complete form,

$$\widetilde{E}^h_{\mathbf{k}jj} = E^h_{\mathbf{k}j} + \delta E^h_{\mathbf{k}jj}(t) + \delta E^{CH} , \tag{2.91}$$

where the same naming convention as in eq. 2.70 has been followed.

## 2.7 MODEL MODIFICATIONS FOR TMDC MONOLAYERS

In order to show that this method can easily be applied to very diverse semiconductor systems, we will now go through the steps needed to model the carrier dynamics in a TMDC. This section will follow the same logical ordering with which different terms were presented in the previous sections and highlight the changes that have to be implemented. As a side note, this also shows that some of the steps discussed in the rest of the chapter are not needed, as long as parameters for the model can be obtained from external sources, e.g., density functional theory (DFT) simulations or fitting to experimental results.

Following Berghäuser and Malic [60] we write the wave function in the following tight-binding form

$$\psi_{\lambda_s \xi \mathbf{k}}(\mathbf{r}) = \frac{1}{\sqrt{N}} \sum_{j \in \{Mo,S\}} C_{\lambda_s \xi \mathbf{k} j} \sum_{\mathbf{R}_j}^{N} e^{i\mathbf{k}\cdot\mathbf{R}_j} \phi_{\lambda_s \xi j}(\mathbf{r} - \mathbf{R}_j) \ , \tag{2.92}$$

with the band, $\lambda \in \{c, v\}$, spin, $s \in \{\uparrow, \downarrow\}$, and valley, $\xi \in \{K, K'\}$, indices. Here $\phi_{\lambda_s \xi j}(\mathbf{r} - \mathbf{R}_j)$ provide the basis for the tight-binding expansion and are linear combinations of the relevant atomic orbitals†. The energy dispersion of the independent electrons can then be obtained by solving the Schrödinger equation

$$\mathcal{H}_0 \psi_{\lambda_s \xi \mathbf{k}} = E_{\lambda_s \xi \mathbf{k}} \psi_{\lambda_s \xi \mathbf{k}} \ , \tag{2.93}$$

where the Hamiltonian, $\mathcal{H}_0$, is composed of a kinetic and a spin-orbit term,

$$\mathcal{H}_0 = \mathcal{H}_{kin} + \mathcal{H}_{so} = \frac{p^2}{2m_0} + U(\mathbf{r})\, \mathbf{L} \cdot \mathbf{S} \ , \tag{2.94}$$

† For a $MoS_2$ monolayer the valence band is mainly formed by the $d_{x^2+y^2} \pm i d_{xy}$ orbitals of the molybdenum atoms with a small influence of the $p_x \pm i p_y$ orbitals of the sulphur atoms while the conduction band is dominated by the $d_{z^2}$ orbitals of Mo with a minor influence of the $p_x \pm i p_y$ orbitals of the S atoms. The $\pm$ sign correspond to the presence of two non-degenerate valleys, K and K′.

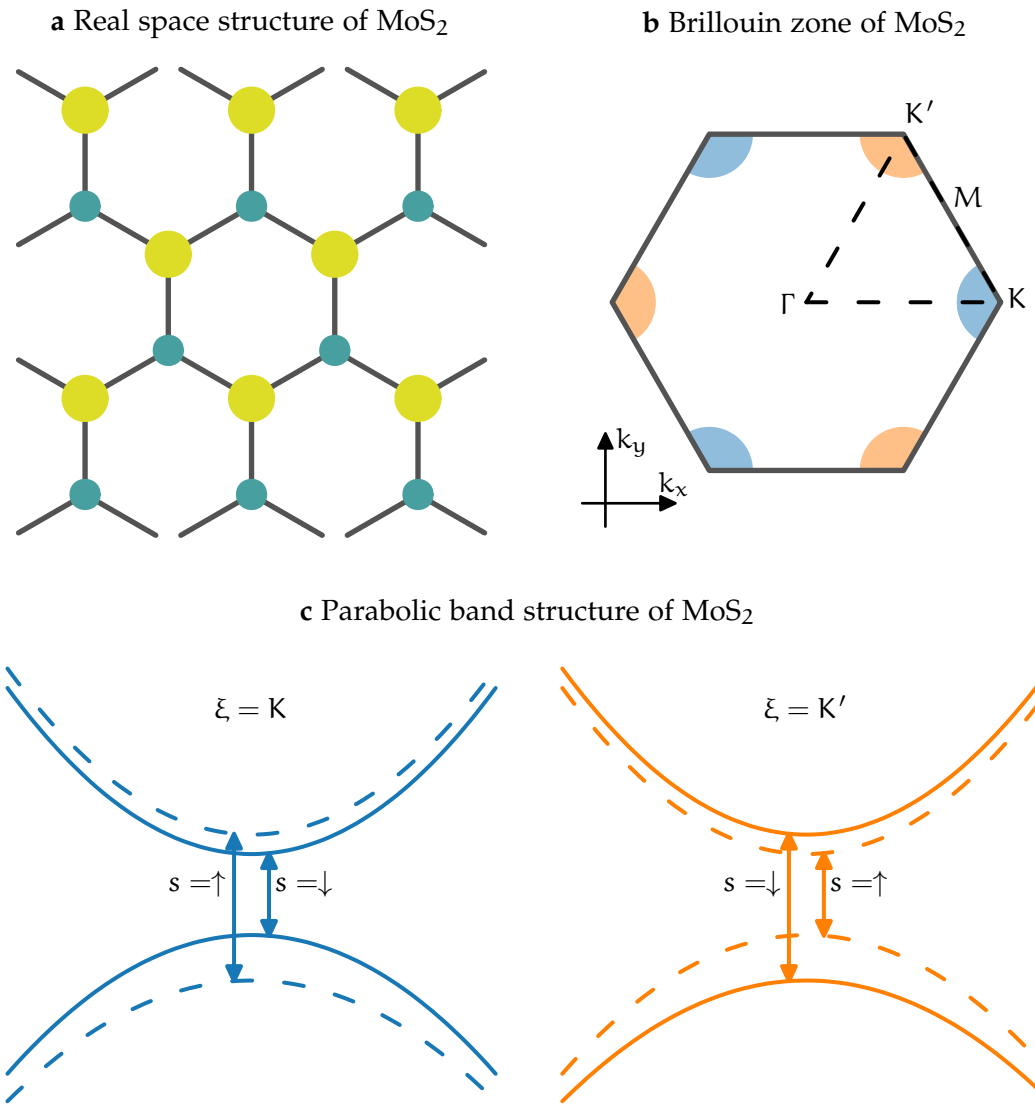


**Figure 2.3:** Pane a shows a schematic representation of the real space structure of a TMDC monolayer. This shows the characteristic hexagonal lattice composed of metal (blue) and chalcogen (yellow) atoms, e.g. Mo and S, respectively. Pane b shows the Brillouin zone corresponding to a hexagonal lattice. The presence of two different constituents results in non equivalent K (blue) and K′ (orange) valleys. Pane b shows the parabolic band approximation for the K (left) and K′ (right) valleys with masses and gaps fitted to DFT results. Note the inversion of the spin-split bands between the K and K′ valleys.

with the linear momentum, $\mathbf{p}$, angular momentum, $\mathbf{L}$, and spin, $\mathbf{S}$, operators. We further assume a nearest-neighbour scheme in which

$$\langle \phi_{\lambda_s \xi j}\left(\mathbf{R}_j\right) | \phi_{\lambda_s \xi i}\left(\mathbf{R}_i\right)\rangle = \delta_{i,j} \tag{2.95}$$

$$\langle \phi_{\lambda_s \xi j}\left(\mathbf{R}_j\right) | \mathcal{H}_{kin} | \phi_{\lambda_s \xi i}\left(\mathbf{R}_i\right)\rangle = t_{\lambda_s} \ . \tag{2.96}$$

Under these assumptions together with the ansatz of eq. 2.92 the solutions in the K and K′ valleys are completely decoupled and the problem is reduced to a set of four linear equations that can be solved to obtain the energy dispersion

$$E_{\lambda_s \mathbf{k}\xi} = \frac{\lambda}{2}\sqrt{\left(E_{gap} + s\xi\Delta\varepsilon_{\lambda_s\xi}\right)^2 + 4\left|t_{\lambda_s}\right|^2 f\left(\mathbf{k}_\xi\right)} \ , \tag{2.97}$$

where $\lambda = \pm 1$ indicates conduction and valence band respectively and $f(\mathbf{k})$ contains the anisotropic $\mathbf{k}$ dependence responsible for the characteristic trigonal warping of hexagonal lattice materials. The wave vector, $\mathbf{k}_\xi$, is measured from the centre of the corresponding valley, i.e., $\mathbf{k}_\xi = \mathbf{k} - \mathbf{K}_\xi$. A small momentum expansion can be used to rewrite eq. 2.97 as an isotropic parabolic band structure,

$$E_{\lambda_s \mathbf{k}\xi} \approx \lambda \frac{\hbar^2 k_\xi^2}{2m_{\lambda_s\xi}} + \frac{\lambda}{2}E_{gap} + \frac{s\lambda\xi}{2}\Delta\varepsilon_\lambda \ , \tag{2.98}$$

with the effective masses, $m_{\lambda_s\xi} = \frac{2\Delta\varepsilon_{\lambda_s\xi}\hbar^2}{3|t_{\lambda_s}|^2}$, and the spin-orbit split energy, $\Delta\varepsilon_\lambda$.

Solving the Schrödinger equation also provides the wave functions, eq. 2.92, by determining the values of the tight-binding coefficients, $C_{\lambda_s\xi\mathbf{k}j}$. One can thus proceed with the calculation of the carrier-light coupling strength as momentum matrix elements,

$$\mathbf{M}_{s\xi\mathbf{k}} = \langle \psi_{v_s\xi\mathbf{k}} | \mathbf{p} | \psi_{c_s\xi\mathbf{k}} \rangle \ , \tag{2.99}$$

where we are assuming optically induced transitions to be vertical in k space and preserve the spin index, s[†]. It was shown [60] that the matrix elements derived within this

† For a more convenient inclusion in FDTD, these can be converted to dipole matrix elements through

$$\boldsymbol{\mu}_{s\xi\mathbf{k}} = \frac{\mathbf{M}_{s\xi\mathbf{k}}}{i m \omega_{s\xi\mathbf{k}}} \ ,$$

model reproduce the experimentally observed circular dichroism of this class of materials [49] as electrons in the K (K′) valley only couple with right-handed (left-handed) circularly polarised light.

Furthermore, the 2D hexagonal lattice of a TMDC monolayer is not centrosymmetric as a consequence of the lattice base including two different atoms. Indeed, when the crystal is inverted with respect to the centre of the hexagon the metal atom is replaced by a chalcogen and vice versa. This results in a strong SHG from monolayers and systems consisting of an odd number of layers[47, 73]. Conversely, an inversion centre is present in the middle of a bilayer, thus strongly suppressing SHG for even-layered systems. We introduce this behaviour in the model via the inclusion of an in-plane permanent dipole moment for electron and hole states, as discussed in section 2.5.1†.

As the last step the Coulomb matrix elements have to be recalculated

$$V_{\alpha_1\alpha_2\alpha_3\alpha_4} = \widetilde{V}(\mathbf{q})\,\Gamma_{\alpha_1\alpha_2\alpha_3\alpha_4}\,, \tag{2.100}$$

where momentum conservation is taken into account by only using three momentum indices‡, $\alpha = \lambda_s \xi \mathbf{k}$ is the compound index which fully characterises a single-particle electronic state and $\Gamma_{\alpha_1\alpha_2\alpha_3\alpha_4}$ takes into account the tight-binding coefficients, $C_{\lambda_s \xi \mathbf{k}j}$. Since the $\xi$ index is related to momentum and due to momentum conservation it is possible to introduce the following selection rule

$$\Gamma_{\alpha_1\alpha_2\alpha_3\alpha_4} = \Gamma_{\alpha_1\alpha_2\alpha_3\alpha_4}\delta_{\xi_1,\xi_4}\delta_{\xi_2,\xi_3}\,, \tag{2.101}$$

which represents the fact that electrons cannot be scattered from one valley to the other by a pure Coulomb event§. The momentum part of the carrier-carrier interaction matrix

where $\omega_{s\xi\mathbf{k}}$ is the transition frequency.

† Note that for a hexagonal lattice we expect some wave functions to still show some degree of spatial symmetry. This is true for states located at high symmetry points of the reciprocal space, like the K and K′ points are. This makes the permanent dipoles a strongly $\mathbf{k}$ dependent quantity even within the valleys. Nevertheless, for a fast and off-resonant excitation, several different states in the valley contribute to SHG and we can thus approximate the dipole moment to be independent on $\mathbf{k}$.

‡ This means that the four states have momenta $\mathbf{k}_1$, $\mathbf{k}_2$, $\mathbf{k}_3 = \mathbf{k}_1 + \mathbf{q}$ and $\mathbf{k}_4 = \mathbf{k}_2 - \mathbf{q}$.

§ This is only valid if small deviations from the valley centres are considered for the $\mathbf{k}_\xi$, which is consistent with a picture of separated valleys as opposed to a single k index spacing over the whole Brillouin zone.

element, $\widetilde{V}(\mathbf{q})$, is not simply the two-dimensional Fourier transform of the Coulomb potential as it is for quasi-two-dimensional systems like QWs. As a consequence of the two-dimensional nature of these monolayers, the macroscopic dielectric screening is no longer described by a simple dielectric constant. An intrinsic $\mathbf{q}$ dependence has to be included[58, 68],

$$\widetilde{V}(\mathbf{q}) = \frac{e^2}{2\varepsilon_0 \varepsilon(\mathbf{q}) A |\mathbf{q}|} \tag{2.102}$$

$$\varepsilon(\mathbf{q}) = \varepsilon_s (1 + r_0 |\mathbf{q}|) \ , \tag{2.103}$$

where $\varepsilon_s$ is the average of the dielectric constants of substrate and superstrate, $r_0 = \frac{d\varepsilon_\perp}{\varepsilon_s}$ plays the role of a screening length, $d$ is the layer thickness and $\varepsilon_\perp$ is the in-plane component of the dielectric tensor of the bulk material.

All of these consideration affects the parameters that enter the model, the states (and thus indices) that have to be considered and the existing selection rules for both carrier light and carrier-carrier interactions. However, the TMDC Bloch equations maintain the same structure as the semiconductor Bloch equations presented in sections 2.4 and 2.6[60]

$$\partial_t n^e_{s\xi\mathbf{k}}(t) = \partial_t n^h_{s\xi\mathbf{k}}(t) = i\left(\Omega_{s\xi\mathbf{k}}(t)\, p^*_{s\xi\mathbf{k}}(t) - \Omega^*_{s\xi\mathbf{k}}(t)\, p_{s\xi\mathbf{k}}(t)\right) \tag{2.104a}$$

$$\begin{aligned}\partial_t p_{s\xi\mathbf{k}}(t) = &-i\left(\omega_{s\xi\mathbf{k}}(t) - i\gamma_{s\xi\mathbf{k}}\right) p_{s\xi\mathbf{k}}(t) \\ &- i\Omega_{s\xi\mathbf{k}}(t)\left(n^e_{s\xi\mathbf{k}}(t) + n^h_{s\xi\mathbf{k}}(t) - 1\right) \\ &- \frac{i}{\hbar}\mathbf{E}(\mathbf{r},t)\cdot\left(\boldsymbol{\mu}^c_{s\xi\mathbf{k}} - \boldsymbol{\mu}^v_{s\xi\mathbf{k}}\right) p_{s\xi\mathbf{k}} \ ,\end{aligned} \tag{2.104b}$$

where the transition and Rabi frequency are renormalised via the inclusion of Coulomb interaction at the HF level

$$\begin{aligned}\hbar\omega_{s\xi,\mathbf{k}}(t) =& E^{e}_{s\xi,\mathbf{k}} + E^{h}_{s\xi,\mathbf{k}} \\ &- \sum_{\mathbf{k}'} \left( V^{e}_{s\xi}\left(\left|\mathbf{k}-\mathbf{k}'\right|\right) n^{e}_{s\xi,\mathbf{k}'}(t) + V^{h}_{s\xi}\left(\left|\mathbf{k}-\mathbf{k}'\right|\right) n^{h}_{s\xi,\mathbf{k}'}(t) \right)\end{aligned} \tag{2.105}$$

$$\hbar\Omega_{s\xi,\mathbf{k}}(t) = \boldsymbol{\mu}_{s\xi,\mathbf{k}} \cdot \mathbf{E}(\mathbf{r},t) + \sum_{\mathbf{k}'} V_{s\xi}\left(\left|\mathbf{k}-\mathbf{k}'\right|\right) p_{s\xi,\mathbf{k}'}(t) \ . \tag{2.106}$$

## 2.8 CONCLUSION

This chapter provided a quick overview on the description of electrons and holes in semiconductor bulk as well as in heterostructures, e.g., a single lattice matched QW. The second quantisation and density matrix formalisms have been introduced and employed to derive a set of time domain differential equations describing the dynamics of charge carriers in semiconductors at different levels of approximation, cf. eq. 2.45 together with the Hartree-Fock corrections from eq. 2.70 for the dynamics inside a QW and eq. 2.104 for the TMDC case. The resulting time evolution of the microscopic dynamical variables in eq. 2.43 can thus be self-consistently calculated under the influence of classical electromagnetic fields. Furthermore, solving the semiconductor equations of motion provides a way to calculate the time evolution of the macroscopic response of the carrier system, the optical polarisation. This macroscopic polarisation can, in turn, influence back the dynamics of the electromagnetic fields, resulting in the need for a self-consistent solution of the two sub-systems.

In this work, the time evolution of the system is obtained by simultaneously solving in time domain Maxwell's equations and the semiconductor equations of motion by applying the FDTD-ADE algorithm, providing a semi-classical description of the system. At each step, the new electromagnetic fields are obtained by solving a discretised version of Maxwell's equations. The resulting electric field can then be used as input in the

solution of the auxiliary differential equations describing the semiconductor system, namely eqs. 2.45 and 2.104. This provides new values for the microscopic dynamical variables and consequently an updated value of the macroscopic polarisation, defined in eq. 2.46, which then acts as an input to update the electromagnetic fields to a new step in time. Lastly, it is important to notice that this approach requires a spatial discretisation of the semiconductor equations of motion, and thus dynamical variables, matching the one used by the FDTD solver for the electromagnetic fields. As a result, this model can only be used if the spatial step is large enough to ensure that electrons pertaining to different grid points are independent from each other†.

† If smaller mesh sizes are required for the convergence of the electromagnetic fields, correlations between carriers at different spatial positions could be included via a Boltzmann-like approach, as outlined in Hess and Kuhn [92].

# 3 Optical response tailoring in two-dimensional semiconductors

This chapter characterises the model presented in chapter 2 by studying the response to ultrashort optical pulses in the linear and non-linear regimes and for different sets of parameters. We thus highlight how the different components of the model describe different features that are typical of a semiconductor under strong optical excitation. The flexibility of the model is highlighted by showing how a minimal set of changes can modify the response of the system from that of a Quantum Well (QW) to that presented from novel semiconductors like Transition Metal Dichalcogenide (TMDC) monolayers. This is achieved entirely by manipulating the parameters and initial conditions of the model while the same mathematical and computational description is maintained.

Before proceeding with the results it is convenient to note that there are a few simplifications that can be applied to the model as a consequence of the specific excitation regime employed here. First of all, the optical pulse is chosen to propagate along the axis of the two-dimensional material, so that the electromagnetic simulation gets transformed into an effective one-dimensional description. This also implies that the field polarisation is in the plane of the two-dimensional material, i.e., $\mathbf{E} \perp \mathbf{u}_z$, and therefore all dipole matrix elements can be considered only in their $x$ and $y$ components. By imposing this selection rule in the case of an inversion symmetric QW, it is possible to suppress intersubband transitions along with transitions between subbands with different parity, effectively separating the system into two different subsystems and, for a shallow well, resulting in a system which can be described via a single subband approximation.

One further simplification comes from the focus onto the region around the bandgap energy, which is typical when studying the optical response of semiconductors, allowing a description in terms of a simple parabolic band structure, like the one described by eq. 2.10. A more subtle consequence of describing the electronic system in effective mass

approximation is that the equations of motion in eq. 2.45 become isotropic in $k$ in the limit of a non-interacting system. They can thus be solved in the one-dimensional space of $k = |\mathbf{k}|$, provided that the correct weights are introduced when a spectral summation is performed[†]. Although less trivial, it can also be shown that the Coulomb interaction at the Hartree-Fock (HF) level does not affect the $k$ space isotropy of the dynamics[‡]. Furthermore, in the case of direct gap semiconductors, the band extrema are usually located at high symmetry points of the reciprocal space, which results in an isotropic response to fields polarised in the $xy$ plane so that a specific polarisation, e.g., $\mathbf{E} \parallel x$, can be chosen without loss of generality. Finally, the dipole matrix elements and polarisation dephasing rates are taken to be homogeneous over the considered region of reciprocal space and all intraband relaxation processes are ignored. In other words, the carriers are frozen in reciprocal space for the whole duration of the pulse. This follows from the ultrashort nature of the optical pulse and is well justified in the linear regime or when the central frequency of the exciting pulse lies in the gap region.

## 3.1 LINEAR RESPONSE OF A SEMICONDUCTOR QW

In this and the following section, we are interested in capturing the response of the semiconductor system in the case of a linear and non-linear excitation, respectively. When the exciting pulse is weak enough, optically active systems show a linear response,

† Given a quantity $F$, which is calculated as a spectral summation of the microscopic $f(k)$, and using the common limit of a crystal of infinite volume,

$$F = \lim_{A\to\infty} \frac{1}{A} \sum_{\mathbf{k}} f(k) = \int \frac{d\mathbf{k}}{(2\pi)^2} f(k) = \int_0^\infty dk \frac{k}{2\pi} f(k) \ ,$$

where the last equality uses the fact that the quantity $f$ only depends on the magnitude of $\mathbf{k}$.

‡ This comes as a consequence of the HF correction terms from eqs. 2.71 to 2.73 containing a full summation over the two-dimensional reciprocal space and the fact that the Coulomb interaction only depends on the magnitude of the exchanged momentum, $q = |\mathbf{k} - \mathbf{k}'|$.

i.e., the polarisation induced in the material is linear in the exciting field. As a consequence the linear susceptibility,

$$\chi^{(1)}(\omega) = \frac{P(\omega)}{\varepsilon_0 \varepsilon E(\omega)}, \tag{3.1}$$

is independent on the intensity of the excitation. On the other hand, as the excitation increases in strength, more terms of the series presented in eq. 2.47 become non-negligible giving rise to a non-linear response, cf. section 3.2.

For a semiconductor system, one is usually interested in probing the bandgap region as well as the lower part of the interband transition region, which usually corresponds to an energy range on the order of 100 meV. Thanks to the time domain nature of the employed method it is possible to collect the system response across multiple frequencies from a single simulation, in analogy with what can be achieved experimentally. To effectively achieve such a result it is convenient to employ an ultrashort optical pulse as this provides a spectrally broad probing field[†].

We excite the system with a hyperbolic secant-shaped transform-limited pulse,

$$E(t) = E_0 \cos(\omega_p t) \operatorname{sech}\left(\frac{t}{\tau}\right), \tag{3.2}$$

where $\omega_p = 2\pi\nu_p = \frac{2\pi c}{\lambda_p}$ is the central (angular) frequency of the pulse, $\lambda_p$ is the vacuum wavelength and $\tau$ defines the duration of the pulse, corresponding to a full width half maximum (FWHM) $\Delta_t \approx 2\tau \log\left(2+\sqrt{3}\right)$. The spectral content of the pulse can be calculated analytically by performing the Fourier Transform of eq. 3.2 and is also expressed as a hyperbolic secant centred at $\omega_p$ whose FWHM is

$$\Delta_\omega = \frac{2\Delta_t}{\pi\tau^2} \approx \frac{8\log^2\left(2+\sqrt{3}\right)}{\pi\Delta_t} \approx \frac{4\log\left(2+\sqrt{3}\right)}{\pi\tau}. \tag{3.3}$$

In order to isolate the QW response as much as possible from any contribution from the environment, we first proceed to study the case of a single 10 nm thick $In_{0.2}Ga_{0.8}As/GaAs$

† Given a generic transform limited pulse of duration $\Delta_t$, e.g., measured as FWHM, the corresponding spectrum has a width of $\Delta_\omega = \frac{\mathcal{C}}{\Delta_t}$, where $\mathcal{C}$ is a constant depending on the specific shape of the pulse envelope.

| | | |
|---|---|---|
| QW thickness | $w$ | 10 nm |
| Effective electron mass | $m_e$ | 0.06 $m_0$ |
| Effective hole mass | $m_h$ | 0.33 $m_0$ |
| Bandgap | $E_g$ | 1.21 eV |
| Dipole matrix element | $\mu$ | 0.5 nm |
| Polarisation dephasing | $\gamma^p$ | 2 $ps^{-1}$ |
| QW refractive index | $n_{QW}$ | 3.698 |
| Barriers refractive index | $n_b$ | 3.551 |
| Initial excitation density | $N_e$ | $4 \times 10^9$ $m^{-2}$ |
| Number of sampling points in k space | $N_k$ | 600 |
| Energy cut-off | $E_c$ | 2.04 eV |
| Spatial step of FDTD grid | $\Delta_x$ | 10 nm |
| Temporal step of FDTD grid | $\Delta_t$ | 0.0333 fs |

**Table 3.1:** Parameters used to simulate the dynamics of carriers in a semiconductor QW at 300 K

QW immersed in an infinitely extended passive medium whose refractive index matches the one of the barrier material, $n_b = 3.551$ (cf. table 3.1). The relevant parameters for the description of the carrier dynamics in the QW are listed in table 3.1. A pulse with the time dependence written in eq. 3.2 and $\Delta_t = 15$ fs is then started inside the homogeneous region and incident on the QW. The full-field dynamics of the reflected and transmitted fields is recorded as the time traces $E_T(t)$ and $E_R(t)$ and their spectral content numerically calculated via the *FFT* algorithm. The resulting (complex) amplitudes can be converted to intensities as

$$\mathcal{I}(\omega) = \frac{|\mathcal{E}(\omega)|^2}{c\mu_0} = \varepsilon_0 c\,|\mathcal{E}(\omega)|^2 \ , \tag{3.4}$$

where $c = (\mu_0\varepsilon_0)^{-1/2}$ is the speed of light, $\varepsilon_0$ is the vacuum permittivity and $\mu_0$ is the vacuum permeability. As a consequence of energy conservation, it is possible to decompose the incident intensity spectrum as reflected, $\mathcal{I}_R(\omega)$, transmitted, $\mathcal{I}_T(\omega)$, and absorbed, $\mathcal{I}_{abs}(\omega)$, components resulting in a relationship between the reflectance, $R(\omega)$, transmittance, $T(\omega)$, and absorptance, $\alpha(\omega)$, coefficients for energy. This allows for the

calculation of the absorption spectrum from the measurement of the transmitted and reflected field time traces and their spectral components,

$$\alpha(\omega) = 1 - R(\omega) - T(\omega) = 1 - \frac{\mathcal{I}_R(\omega) + \mathcal{I}_T(\omega)}{\mathcal{I}_{inc}(\omega)} \,. \tag{3.5}$$

This process of collecting time traces of the field and analysing them for their spectral component, as well as the calculation of absorptivity from eq. 3.5, is the main source of results when performing one-dimensional Finite Difference Time Domain (FDTD) simulations. In the following section 3.1.1 we will start by analysing the linear response of a single QW with independent electrons in order to build an understanding of the phenomena that are included in the model and what is their signature in the field spectra and time traces. We will then proceed to include carrier-carrier interaction in section 3.1.2 and examine how this changes the linear response.

### 3.1.1 Independent electrons

We first analyse the single QW in a homogeneous background in the limit of non-interacting electrons. The pulse used to probe the system has the central frequency close to the bandgap energy, $\hbar\omega_p \approx E_g$, and a time duration $\Delta_t = 15$ fs which results in a broad spectrum, FWHM of $\hbar\Delta_\omega \approx 0.193$ eV. We use eq. 3.5 to calculate the linear absorption spectrum, $\alpha(\omega)$, which is shown in fig. 3.1 as a function of the probe photon energy, $\hbar\omega$. The vertical dashed line marks the bandgap energy, $E_g$, and separates the spectrum in a gap region (lower energy, red shading) and an interband transition one (higher energy, blue shading). The linear absorption of a system of independent electrons in the limit of no polarisation dephasing, $\gamma^p = 0$, can be evaluated via perturbation theory,

$$\alpha_t(\omega) \propto \mu^2_{\mathbf{k}_0} g_J(\hbar\omega) \tag{3.6}$$

$$g_J(\varepsilon) = \sum_{\mathbf{k}} \delta\left(E^e_{\mathbf{k}} + E^h_{\mathbf{k}} - \hbar\omega\right) \,, \tag{3.7}$$

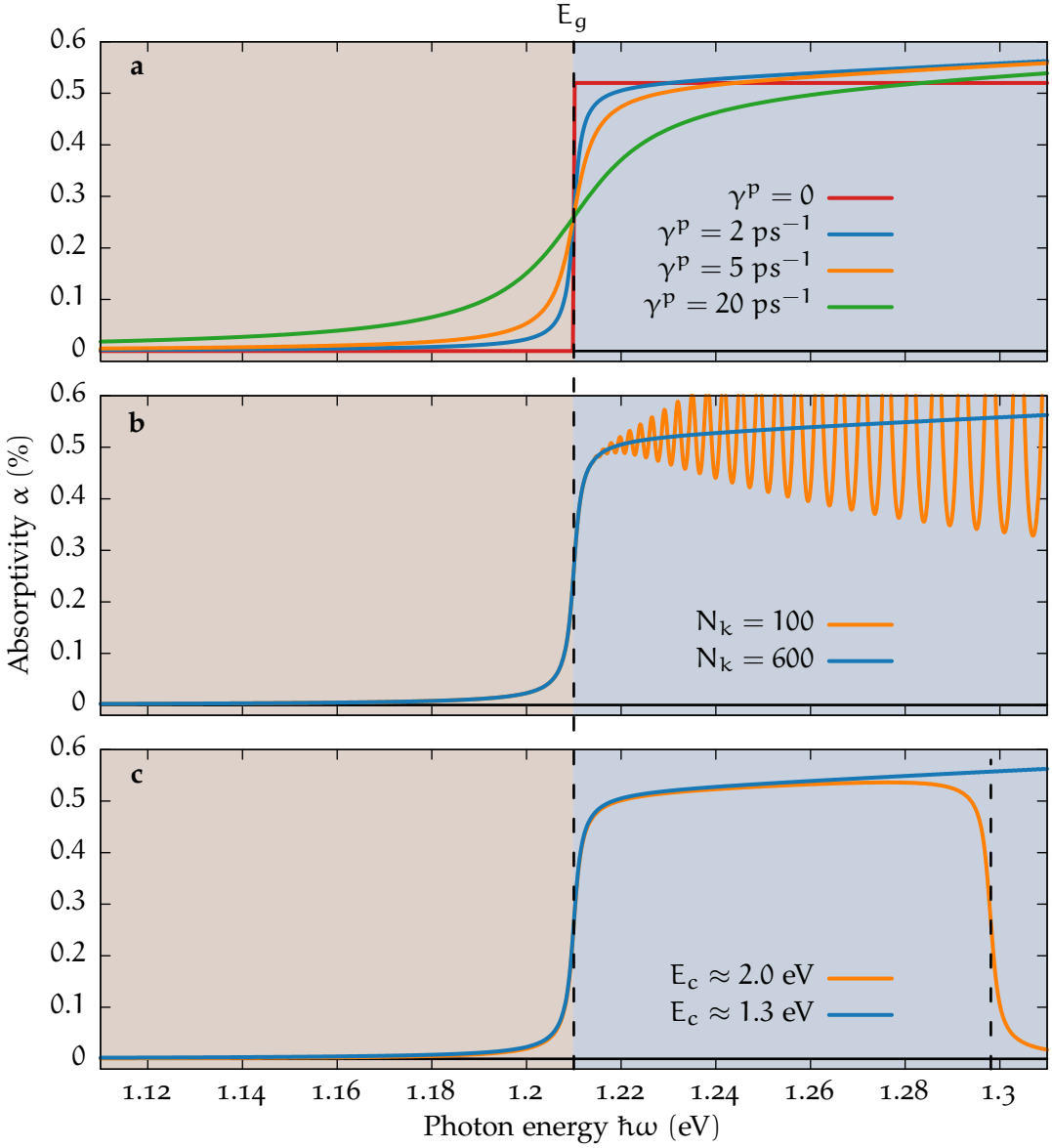


**Figure 3.1:** Absorption spectrum, $\alpha(\omega)$, from a single QW embedded in an infinite passive material with the same refractive index as its barriers. The vertical dashed line at the centre is located at the gap energy, $E_g = E_g' + E_1^e + E_1^h = 1.21$ eV, and separates the gap region (orange shading) from the interband transition region (blue shading). Panel a: Smearing of the absorption spectrum around the bandgap, due to finite temperature effects, modelled via the polarisation dephasing rate, $\gamma^p$. The values used for the different lines are $\gamma^p = 0$ (red), $\gamma^p = 2$ ps$^{-1}$ (blue), $\gamma^p = 5$ ps$^{-1}$ (orange) and $\gamma^p = 20$ ps$^{-1}$ (green). Panel b: Effect of using a finite and discrete set of points to represent the band structure. The blue line is the same as the one in fig. 3.1a and is obtained with the parameters in table 3.1. The orange line is obtained with the same parameters but the band structure is sampled with a reduced number of points, $N_k = 100$. Panel c: Effect of introducing a cut-off in the band structure, $E_c$. The blue line is the same as the one in fig. 3.1a and is obtained with the parameters in table 3.1. The orange line is obtained with the same parameters but the band structure is truncated at a lower energy, $E_c \approx 1.3$.

where the dipole matrix element, $\mu_{\mathbf{k}}$, is assumed to be a slowly varying function of $\mathbf{k}$ and can, therefore, be evaluated at a high symmetry point, $\mathbf{k}_0$, and $g_J(\varepsilon)$ is the joint density of states (JDOS). Within the effective mass approximation of a QW, the JDOS works out to

$$g_J(\hbar\omega) = \frac{2\pi m^*}{\hbar^2}\Theta(\hbar\omega - E_g) \ , \tag{3.8}$$

where $\Theta(x)$ is the Heaviside step function and $m^*$ the electron-hole reduced mass. This, however, is only true if no incoherent processes are considered, which would tend to lower the coherence between pairs of states that are coupled through an optical transition. As it was previously discussed (cf. section 2.6.2) in our model we account for the loss of coherence through a dephasing term, $p_{\mathbf{k}} \propto -\gamma^p_{\mathbf{k}} p_{\mathbf{k}}$, which has the effect of smearing the sharp transition introduced by the Heaviside step function, as it can be seen from the blue line in fig. 3.1a as compared to the red line showing the result for a totally coherent system. We further assume that the dephasing rate changes slowly in $\mathbf{k}$ and thus use a constant value, $\gamma^p$[†]. The oscillating behaviour that can be observed at the right hand of fig. 3.1 is a numerical artefact that follows from the representation of the band structure as a set of $N_k$ discrete levels. The levels are taken to be uniformly distributed in $k$ space resulting in an increased energy spacing at higher energy, which results in an increased amplitude and period of these numerical oscillations. This is apparent in fig. 3.1b, which also shows how the onset and amplitude of the oscillations are worsened by decreasing $N_k$. Similarly, we have to introduce a cut-off in the parabolic band structure at wave vector $\mathbf{k}_c$, which results in a finite bandwidth for the absorption region, as opposed to what is given by eqs. 3.6 and 3.8. This effect can be seen in fig. 3.1c, where the cut-off energy has been lowered, $E_c = \frac{\hbar^2 k_c^2}{2m^*} = 1.298$ eV, and corresponds to the second dashed line.

The linear response of the QW is also affected by the presence of excited electrons and holes as this reduces the number of states available for optical transitions. As the

† The dephasing rate can be either set to a known value for the semiconductor material of interest or used as a free parameter to match experimental results. A third, more theoretical, approach consists in explicitly calculating the contributions to $\gamma^p_{\mathbf{k}}$ from phonon and carrier-carrier scattering. This can be achieved self-consistently by extending the equations of motion to include the phonon system and higher orders carrier-carrier correlations[6] or by interpolating from pre-computed tables[31, 32].

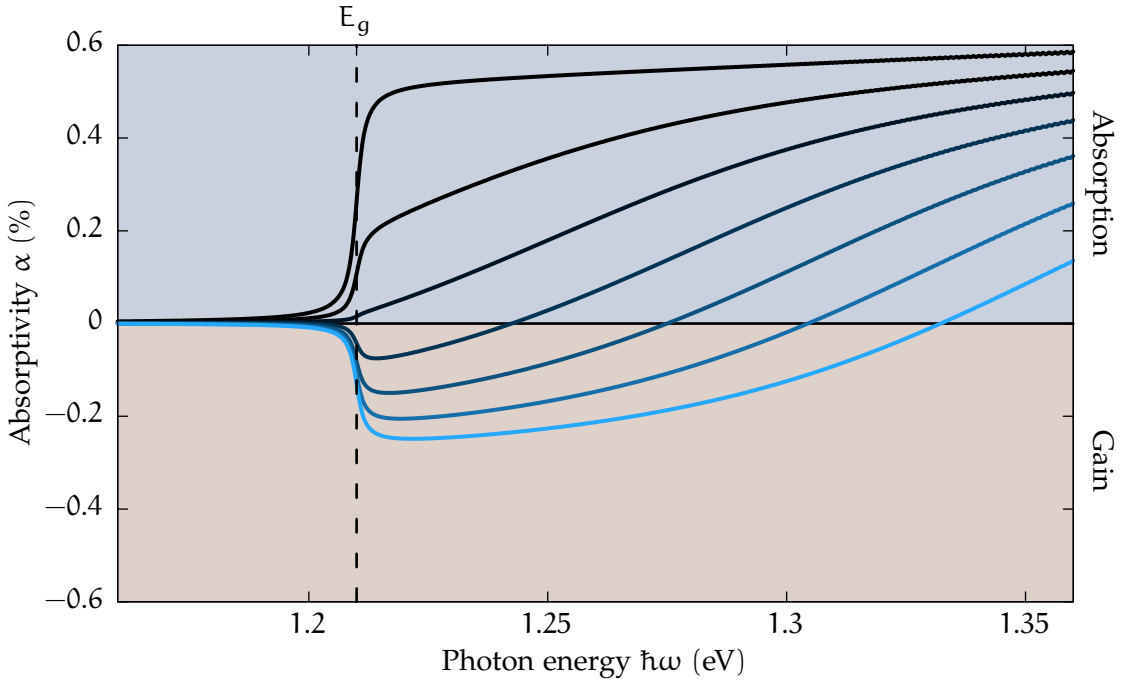


**Figure 3.2:** Absorption spectrum, $\alpha(\omega)$, of a single QW with the same environment as in fig. 3.1. Different lines correspond to different values of the carrier sheet density, $N = \{0, 0.5, 1.0, 1.5, 2.0, 2.5, 3.0\} \times 10^{16}$ m$^{-2}$, with values increasing from black to light blue. The vertical dashed line marks the bandgap and the shaded regions correspond to absorption (blue) and gain (orange).

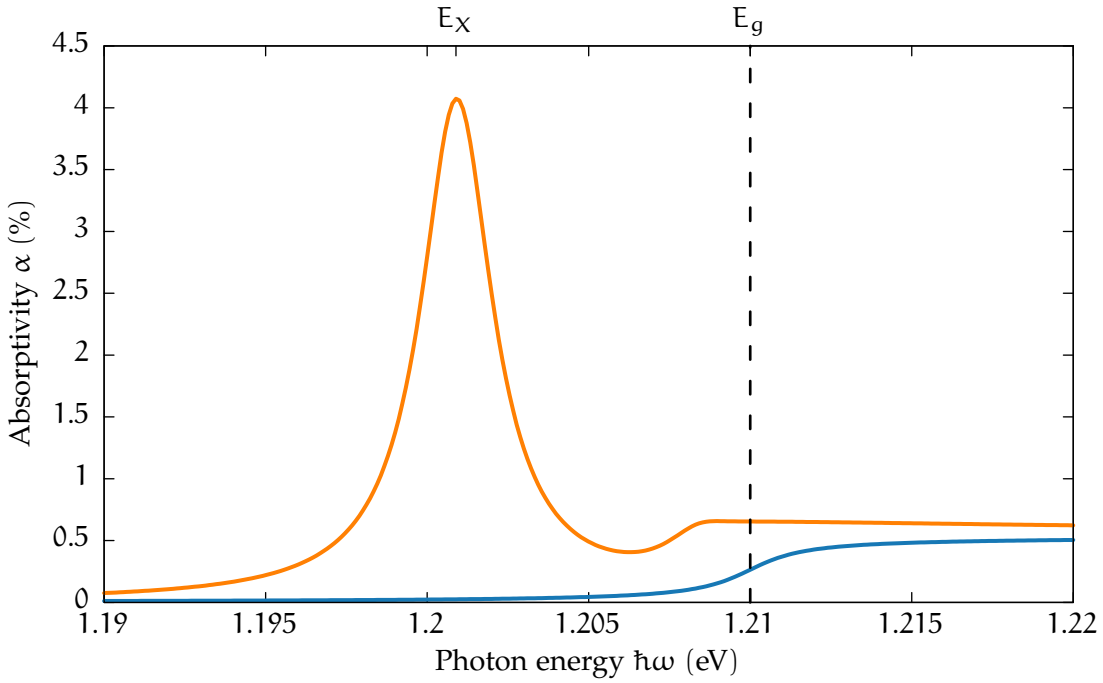


**Figure 3.3:** Absorption spectrum, $\alpha(\omega)$, of a single QW within HF approximation (orange line) compared to that obtained from independent electron approximation (blue line). The simulation domain is filled with a passive dielectric with the same refractive index as the QW barriers, as to isolate the response of the QW. The vertical dashed line marks the bandgap energy, $E_g = 1.21$ eV, below which lies the exciton resonance centred at $E_X = 1.2001$ eV.

density of excited carriers increases, the low transition energy states will start to be more populated and reach zero absorption. Even higher densities will then result in a sign change leading to negative absorption which, going back to eq. 3.5, means that the intensity of the optical fields leaving the system is higher than the incident intensity for certain frequencies. This behaviour is shown in fig. 3.2 for values of the carrier sheet density, N, going from $0.5 \times 10^{16}$ m$^{-2}$ to $3 \times 10^{16}$ m$^{-2}$. As a result of increased carrier density, the gain spectrum provided by the semiconductor system becomes broader.

### 3.1.2 Interacting electrons

We proceed to use a similar setup and probing pulse as in section 3.1.1 to now probe the linear response of a system of interacting electrons and holes, as is described from the HF corrections presented in section 2.6. Following what was done in the non-

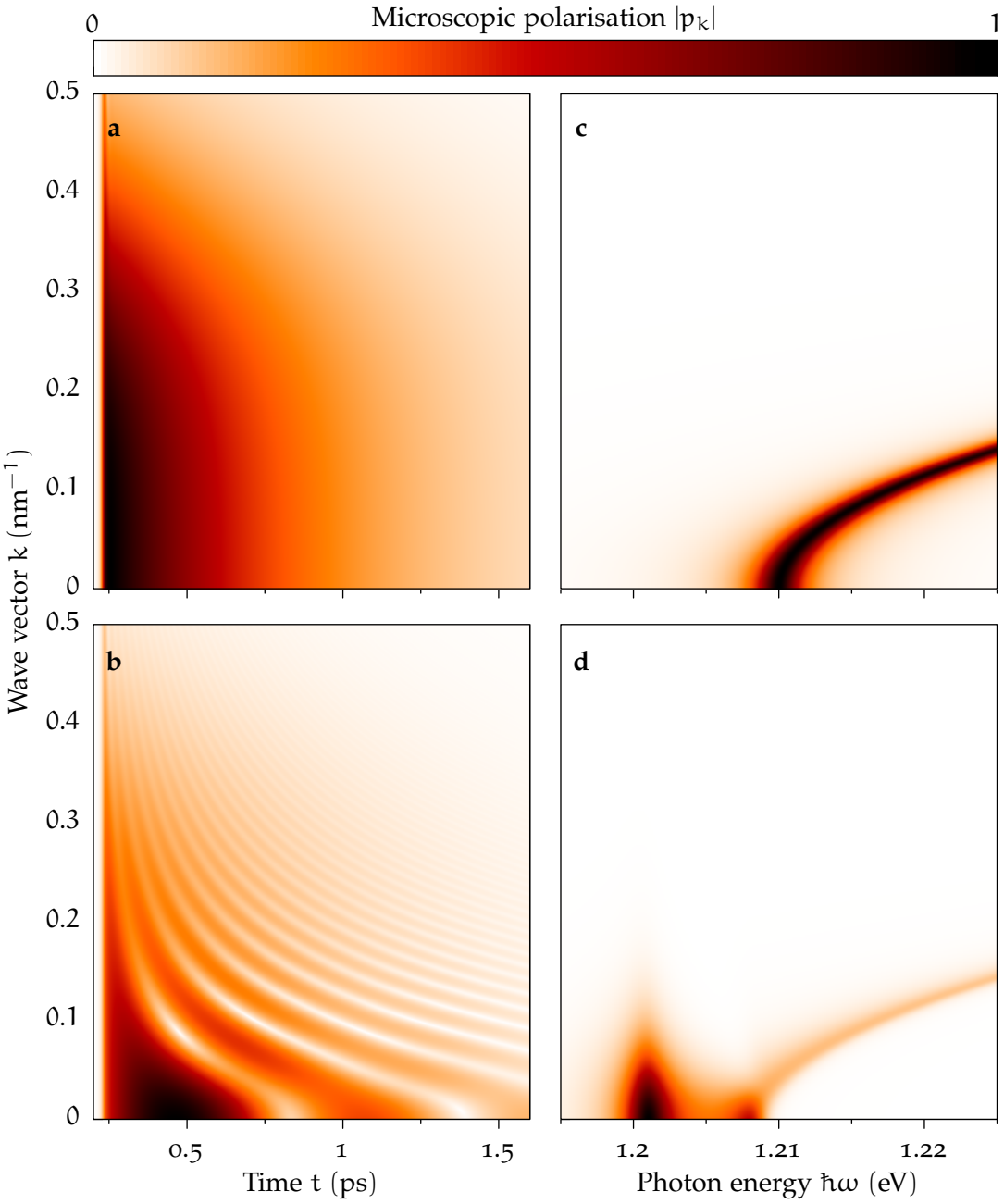


**Figure 3.4:** Time evolution and spectral content of the microscopic polarisation, $p_k$, in a single QW immersed in a homogeneous background and excited within the linear regime. Pane a shows the dynamics of the polarisation envelope, $|p_k(t)|$, under an independent carrier approximation, while pane b shows the spectral content of each microscopic polarisation, $|p_k(\omega)|$. Panes b and d show the same data after including the Coulomb interaction. The data in each pane is normalised to fit in the $[0, 1]$ interval.

interacting case we measure the fraction of field transmitted and reflected at each wavelength and use them to calculate the absorption spectrum, $\alpha(\omega)$. Figure 3.3 shows a comparison between the absorption from a non-interacting electron-hole gas (blue) and the response arising from the same system with the inclusion of Coulomb interaction (orange). The most striking feature of the interacting system is the strong peak located within the bandgap region, $E_X = 1.201$ eV. Such a resonance is the signature of a bound electron-hole state, the exciton, in which the two particles of opposite sign feel an attractive Coulomb force, resulting in a lower energy requirement to excite an electron from the valence to the conduction band. Furthermore, the bandgap is shifted to lower energy by $\delta E^{CH}$ as a consequence of including a screened Coulomb potential, as described in section 2.6.3. A small enhancement in absorption is present for frequencies corresponding to band-to-band transitions, i.e., at higher energy than the bandgap, and a generally flat spectrum is observed for these processes.

The binding energy of the electron-hole pair is calculated from the energy difference between the exciton peak and the bandgap, $E_b = E_g - E_X = 9$ meV $\approx 2.44\ E^*_{Ry}$, with the modified Rydberg energy

$$E^*_{Ry} = \frac{m^*}{\varepsilon^2} E_{Ry} = \frac{m_0 m^* e^4}{32\pi^2 \varepsilon_0^2 \varepsilon^2 \hbar^2} = 3.694 \text{ meV} . \tag{3.9}$$

This value is mainly determined by the QW thickness in relation to the effective Bohr radius in the bulk material, as this provides a measure of how confined the carriers are in the QW[102]. This is introduced through the calculation of the Coulomb form factors from eq. 2.66, as in our model the QW thicknes only affects the calculation of the envelope functions, $\phi_\delta(z)$. The two limiting cases, which can be calculated analytically, are an infinitely thin 2D QW, in which $E_b = 4E^*_{Ry}$, and one that is thick enough to be considered a bulk material, $E_b = E^*_{Ry}$.

Up to here, we focussed on how the combined use of FDTD and a semiconductor model can be used, in a way which is analogous to experiments, to study the optical response of simplified systems by only observing the dynamics of the fields outside of the system that is being investigated. In contrast to experiments, however, we can get

more insight into the behaviour of the system by collecting other kinds of data, like micro- or macroscopic semiconductor quantities, as well as field dynamics and field profiles throughout the structure.

In order to obtain the linear response of the system, we are operating in a regime of weak excitation in which the (quasi-equilibrium) initial distributions of carriers are not perturbed so that we can here focus on the microscopic polarisation, $p_k(t) = \bar{p}_k(t)\, e^{i\theta_k(t)}$. The left-hand side of fig. 3.4 (panes a and b) shows the dynamics of the absolute value of the band resolved polarisation, $\bar{p}_k(t)$, which is observed to change slowly compared to all the involved frequencies and can thus be identified as a (slowly varying) envelope of the signal. Conversely, the right-hand side (c and d) shows the result of performing a numerical Fourier transform of the $k$ dependent polarisation, and thus shows the quickly oscillating part of the time domain signal in term of the constituting frequencies. Figure 3.4a shows that for the non-interacting system a wide range of $k$ states is excited due to the broad spectrum of the incoming pulse and a maximum in the polarisation is achieved soon after the peak of the probing pulse, $t_p = 0.234$ ps. Following this, all coherences undergo a simple exponential decay characterised by the dephasing rate, $\gamma^p$. Figure 3.4c shows that the microscopic polarisations oscillate at a frequency $\omega_k$, corresponding to the energy difference of the dipole active transition at $k$ (cf. eq. 2.45c) and thus shows the parabolic nature of the band structure. In contrast to this, fig. 3.4d shows that in the presence of carrier-carrier interaction multiple spectral components are present in each microscopic polarisation. In the higher frequency part of the spectrum the parabolic shape from fig. 3.4c is recovered, albeit shifted towards lower energies by the Coulomb Hole energy. At energies lower than the bandgap, however, a completely new resonance frequency is introduced which shows very little change with $k$ and can thus be identified as the response from a localised state. As a consequence of the strength of the Coulomb interaction, as well as the collective nature[†], this state

† The macroscopic polarisation is obtained as a spectral summation from the microscopic polarisations

$$P(t) = \frac{\mu}{A} \sum_k \Re\left(p_k(t)\right) = \mu \int g(\epsilon)\, p(\epsilon, t)\, d\epsilon \,.$$

When all the microscopic polarisations have a component oscillating with the same phase and frequency, they will coherently sum up $P(\omega_X) \approx \Delta E_g(\epsilon(k_0))\, p_{k_0}(\omega_X)$.

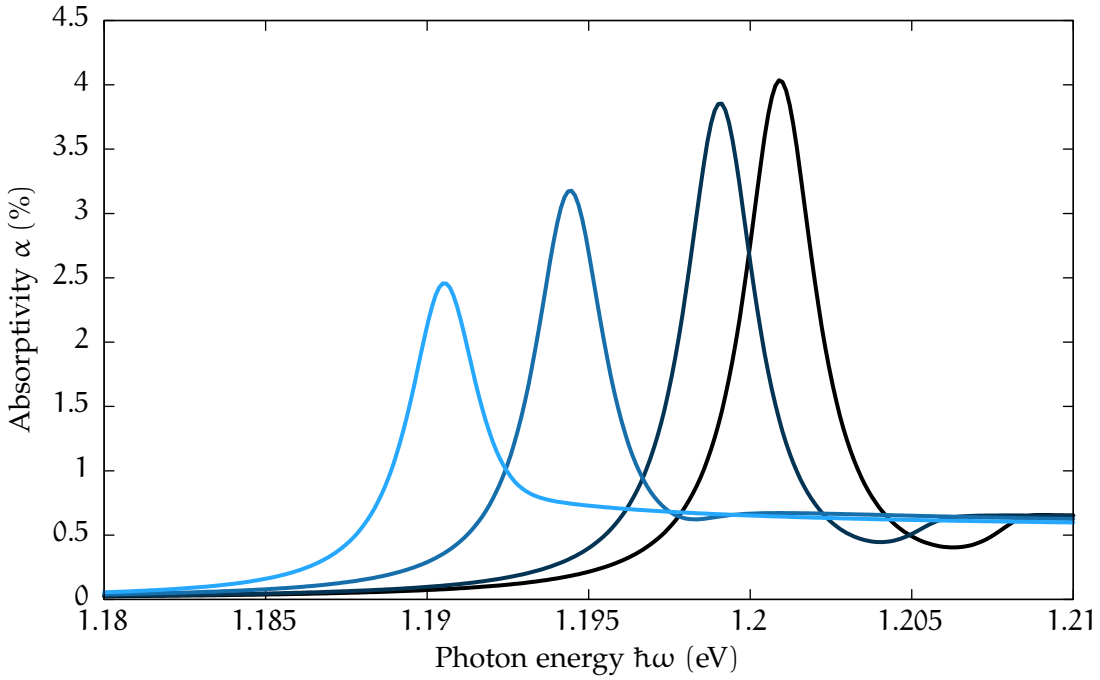


**Figure 3.5:** Absorption spectrum, $\alpha(\omega)$, of a single QW within HF approximation as a function of carrier density. Different lines correspond to different values of the carrier sheet density, $N = \{0.01, 1, 5, 10\} \times 10^{14}$ m$^{-2}$ with values increasing from black to light blue. The bandgap lies at the right-hand edge of the energy scale.

presents a much larger absorption as compared to single-particle band to band transitions. The presence of two distinct frequencies can also be observed in the time domain results from fig. 3.4b as it introduces a beating effect in the envelope of the polarisations.

In a similar way to what we observed for independent electrons in section 3.1.1, we can expect the linear response of a system of interacting electrons to be affected by the presence of previously excited carriers. Results for increasing densities of excited carriers are shown in fig. 3.5, where the carriers, electrons and holes, are assumed to be distributed according to two equilibrium distributions with different chemical potentials, $\mu_e$ and $\mu_h$. As the carrier density is increased from $N = 1 \times 10^{12}$ m$^{-2}$ (black line) to $N = 1 \times 10^{15}$ m$^{-2}$ (light blue line) we observe that the bandgap is further shrunk as a natural consequence of the electron (hole) self-energies depending on the occupation of the conduction (valence) band, cf. eq. 2.74. We further observe an effect from the increased carrier density on the exciton, as the corresponding strong resonance is bleached and redshifted. This has been shown to be a combined effect from Pauli block-

| Material | $n_l$ | $\epsilon_l$ |
|---|---|---|
| SiN | 1.884 | 3.551 |
| $In_{0.2}Ga_{0.8}As$ | 3.698 | 13.675 |
| GaAs | 3.551 | 12.610 |
| AlAs | 2.959 | 8.756 |

**Table 3.2:** Refractive index and background permittivity of all the materials included in the simulation.

ing of band to band transitions, which introduces a dispersionless bleaching, as well as the phenomenological screening of the Coulomb interaction, which is responsible for part of the bleaching as well as the redshift. Conversely, higher order of the Coulomb interaction introduce a balancing blueshift of the exciton energy, so that if all orders are included the exciton peak does not get shifted but purely bleached[103, 104].

### 3.1.3 Environmental effect

After studying the electron dynamics of an isolated QW in a homogeneous background we proceed by introducing a more complex optical environment. For this we choose a semiconductor saturable absorber mirror (SESAM), which is a well-established structure for ultra short pulse generation.[105] The whole structure is included in our simulations as a spatially varying background permittivity $\epsilon_l(z) = n_l^2(z)$, as shown in fig. 3.6, and is surrounded by 2 μm of air on each side. Table 3.2 contains the refractive index and background permittivity of all materials included in the structure.

In order for the structure to be effective, most of the layer thicknesses need to be proportional to the central wavelength of the incoming pulse, $\lambda_0$. The structure is embedded within two anti reflection (AR) coatings obtained via SiN layers of optical length $\frac{\lambda_0}{4}$ which minimize reflection of the pulse at the structure/air interface, thus allowing for a more efficient in-coupling of the light. The distributed Bragg reflector (DBR) is composed by a set of alternating GaAs and AlAs layers, each with an optical length of $\frac{\lambda_0}{4}$. This basic two-layered module is repeated 25 times in order to achieve a very high reflectivity around $\lambda_0$, as shown in fig. 3.7a, where we tuned the pulse to the exciton en-

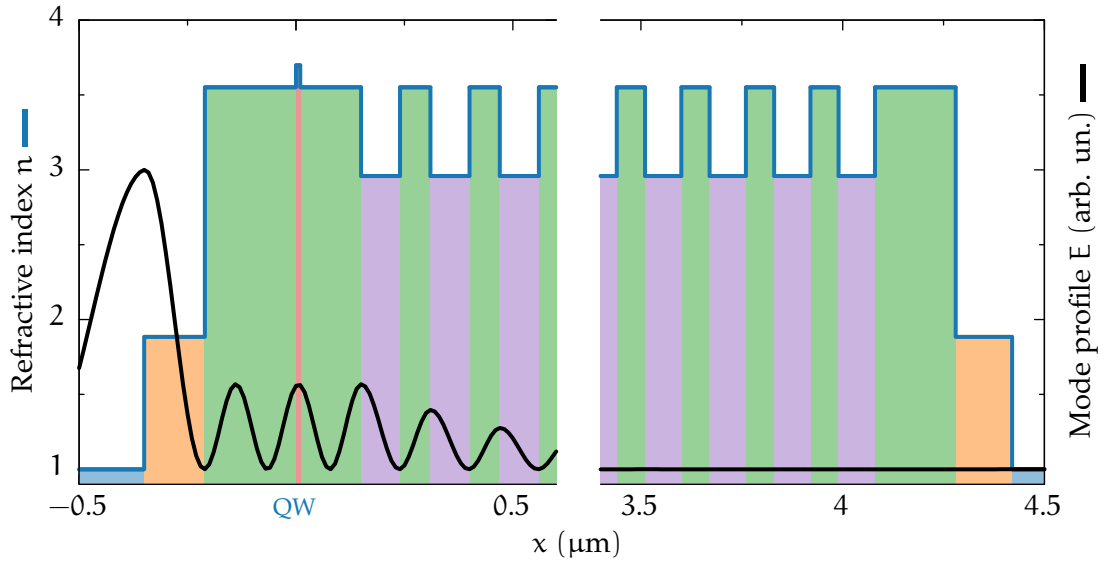


**Figure 3.6:** Refractive index profile of the SESAM structure (blue line). Shaded regions of different colours represent different materials: air (blue), SiN (orange), GaAs (green), InGaAs (red), AlAs (purple). The AR coatings (orange) and DBR layers have thicknesses of $\frac{\lambda_0}{4n}$ and the QW is $\frac{\lambda_0}{4n_b}$ away from the DBR, where $\lambda_0$ is the central wavelength of the incoming pulse and $n_b$ is the barrier refractive index. The black line shows the field profile across the structure at $\lambda = \lambda_0$.

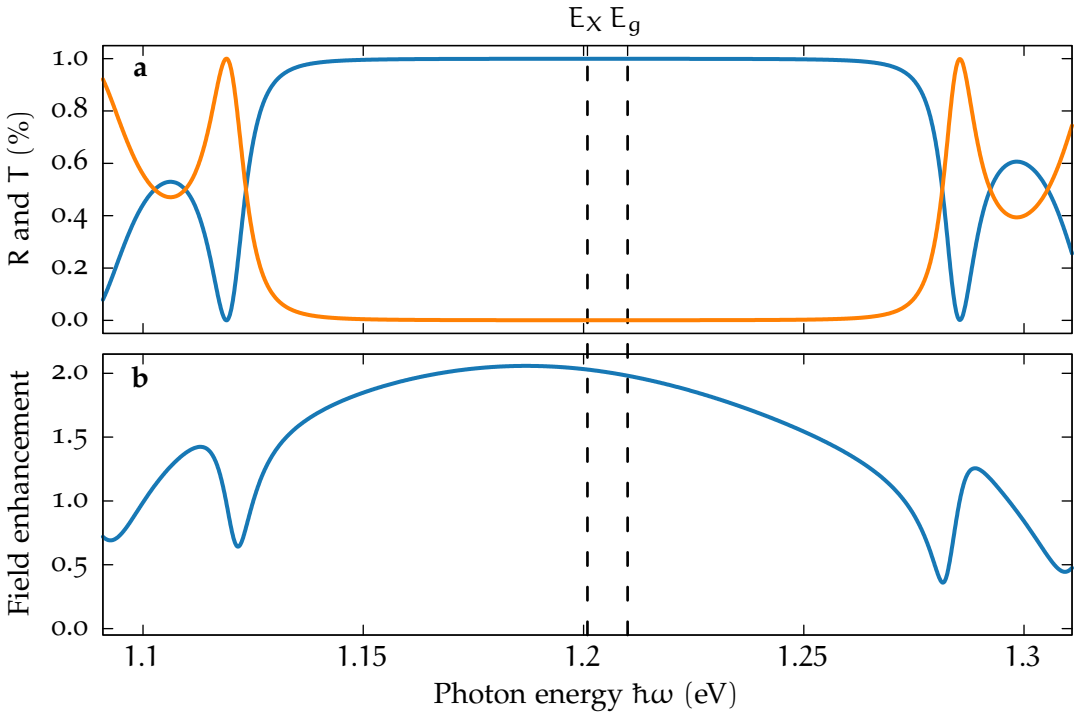


**Figure 3.7:** Pane a: reflectance (blue) and transmittance (orange) spectra of the passive SESAM structure. Pane b: field enhancement at the QW position. The vertical dashed lines indicate the exciton ($E_X$) and gap ($E_g$) energies.

ergy, $E_X$. Due to the presence of the mirror, a standing wave is created inside the GaAs layer between the mirror itself and the anti-reflective layer. Such an interference pattern has zeros at even integer multiples of $\frac{\lambda_0}{4n}$ and maxima at odd ones. The QW is located in such a maximum, in order to take advantage of the field enhancement provided by this interference pattern, and is thus at an optical distance $\frac{\lambda_0}{4}$ from the start of the mirror. Two further layers of arbitrary size are used to isolate the anti-reflection coatings from the mirror on one side and the QW on the other.

The passive structure is characterised first by measuring its characteristic transmittance and reflectance spectra, $T(\omega)$ and $R(\omega)$, as shown in fig. 3.7a. This highlights how the mirror reflects almost perfectly in a broad spectral region around the central wavelength of the pulse while showing oscillation characteristic of a DBR outside the stop band. By measuring the field time trace at the QW position it is further possible to calculate the field enhancement spectrum,

$$\mathcal{F}(\omega) = \sqrt{\frac{\mathcal{I}_{QW}(\omega)}{\mathcal{I}_{inc}(\omega)}} = \sqrt{\frac{\varepsilon_0 n \mathcal{E}^2_{QW}(\omega)}{\varepsilon_0 \mathcal{E}^2_{inc}(\omega)}} = \left|\frac{\mathcal{E}_{QW}(\omega)}{\mathcal{E}_{inc}(\omega)}\right| \sqrt{n}\,, \tag{3.10}$$

where $n = n_{QW}$ is the refractive index at the QW position or, generally, where the field enhancement is measured. Figure 3.7b shows that the field is generally enhanced by a factor between 1.5 and 2 within the stopband region of the DBR, while on the outside it oscillates around 1 following the same pattern seen in fig. 3.7a.

Figure 3.8 shows how the absorption resulting from the inclusion of the QW in the SESAM structure (blue) compares with results from the isolated system (orange, fig. 3.3). Since the DBR and the structure in general have been tuned to the exciton frequency, only the low energy region of the band to band absorption spectrum falls within the stopband, as can be seen in fig. 3.8a for the case of independent carriers. The absorption is increased by a factor $\mathcal{F}^2(\omega) \approx 4$ as compared with the absorption spectrum of an isolated QW. In the case of interacting carriers, fig. 3.8b, the field enhancement results in very large absorption at the exciton energy, whereas the in-band absorption is now decreasing the further we go from the band edge.

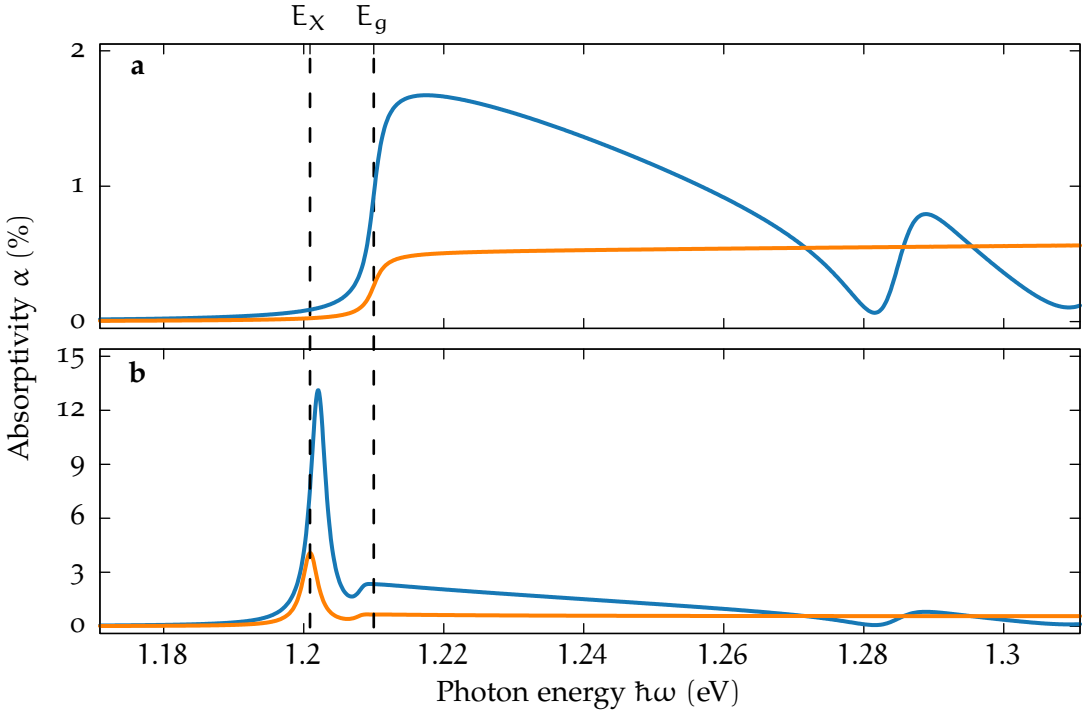


**Figure 3.8:** Absorption spectrum, $\alpha(\omega)$, of a single QW embedded in the SESAM structure (blue lines) compared with results from a homogeneous system (orange lines). The results are presented for the case of independent electrons (a) as well as interacting electrons (b). The vertical dashed lines indicate the exciton ($E_X$) and gap ($E_g$) energies.

## 3.2 NON-LINEAR REGIME AND THIRD HARMONIC GENERATION

In the previous section, it was shown how the linear response of a QW can be manipulated through the environment by using a suitable passive cavity. Such a cavity can be engineered to produce an enhancement in some features of the absorption spectrum while suppressing the response from other spectral regions. An understanding of how this happens in the linear regime can be easily achieved from calculating the cavity induced field enhancement, as it can be deduced from comparing figs. 3.3, 3.6 and 3.8. As the semiconductor is driven into a non-linear regime, however, the back-and-forth interaction between the active material and its near field environment goes beyond what can be described by the field enhancement, e.g., in the case of strong coupling[83, 106, 107]. In such a situation the time domain model presented in this work can provide a dynamical description of the system which treats the active material, the electromagnetic field and the environment all consistently and on the same footing.

To help quantify how the carrier dynamics depends on the excitation intensity it is convenient to draw a comparison with a two-level system, as when Coulomb interaction is neglected the presented semiconductor model falls back to a system of independent two-level systems with the same dipole matrix element. The area of a pulse with respect to a two-level system with dipole matrix element $\mu$ is defined as

$$\theta_2 = \int_{-\infty}^{+\infty} \overline{\Omega}(t)\, dt\,, \tag{3.11}$$

where $\overline{\Omega}(t) = \frac{e\mu\cdot\widetilde{\mathbf{E}}(t)}{\hbar}$ is the Rabi frequency in slowly varying envelope approximation and $\widetilde{\mathbf{E}}(t)$ is the pulse envelope. In the case of a hyperbolic secant pulse like the one presented in eq. 3.2, this integration can be carried out analytically, giving

$$\theta_2 = \frac{e\mu E_0 \tau}{\hbar}\pi\,. \tag{3.12}$$

A pulse of area $\theta_2 = 2\pi$ is defined as the pulse which increases the inversion of the system from the ground state, reaching maximum inversion at the pulse maximum,

and then brings the system back to its ground state. As a consequence of Coulomb interaction in the HF approximation, the Rabi frequency is renormalized and acquires a dependence on the wave vector, $\widetilde{\Omega}_{\mathbf{k}}(t)$. This results in the following definition for the area of a pulse with respect to each one of the QW states

$$\theta_{\mathbf{k}} = \int \widetilde{\Omega}_{\mathbf{k}}(t)\,dt = \theta_2 + \frac{1}{\hbar}\sum_{\mathbf{k}'\neq\mathbf{k}} V^{eh}\left(|\mathbf{k}-\mathbf{k}'|\right)\int |p_{\mathbf{k}'}(t)|\,dt\,, \tag{3.13}$$

where we have used eq. 2.75. This shows that the more complex behaviour of the interacting system cannot be simply described in terms of pulse area. However, we continue to use the pulse area with respect to a two-level system as an approximate measure of pulse strength.

In the non-linear regime the carrier occupations are not fixed at their initial value but evolve dynamically and can thus be used, together with field and polarisation dynamics, to explore the behaviour of the system as it is shown in fig. 3.9. The exciting pulse has a hyperbolic secant shape with an FWHM of 100 fs and is resonant with the exciton energy. The weaker excitation used in figs. 3.9a and 3.9b has an equivalent two-level pulse area $\theta_2 = 0.4\pi$, corresponding to a peak intensity

$$I_0 = \frac{E_0^2}{c\mu_0} = \frac{\hbar^2\theta_2^2}{c\mu_0 e^2\mu^2\tau^2\pi^2} \approx 5.11\times10^{11}\,\frac{W}{m^2}\,, \tag{3.14}$$

while the QW parameters are the same employed in the linear regime and summarised in table 3.1. Figure 3.9a shows the dynamics of the total density of carriers in the semiconductor system,

$$N(t) = \frac{2}{A}\sum_{\mathbf{k}} n^e_{\mathbf{k}}(t) \longrightarrow 2\int g(\epsilon)\,n^e(\epsilon)\,d\epsilon\,, \tag{3.15}$$

where the 2 accounts for the degenerate spin states. From the monotonous increase of density through the pulse action and the absence of Rabi oscillations, it can be deduced that the system behaves as a whole like a two-level system excited by a pulse with area $\theta_s < \pi$. A more refined picture is given by the colour map in fig. 3.9b which

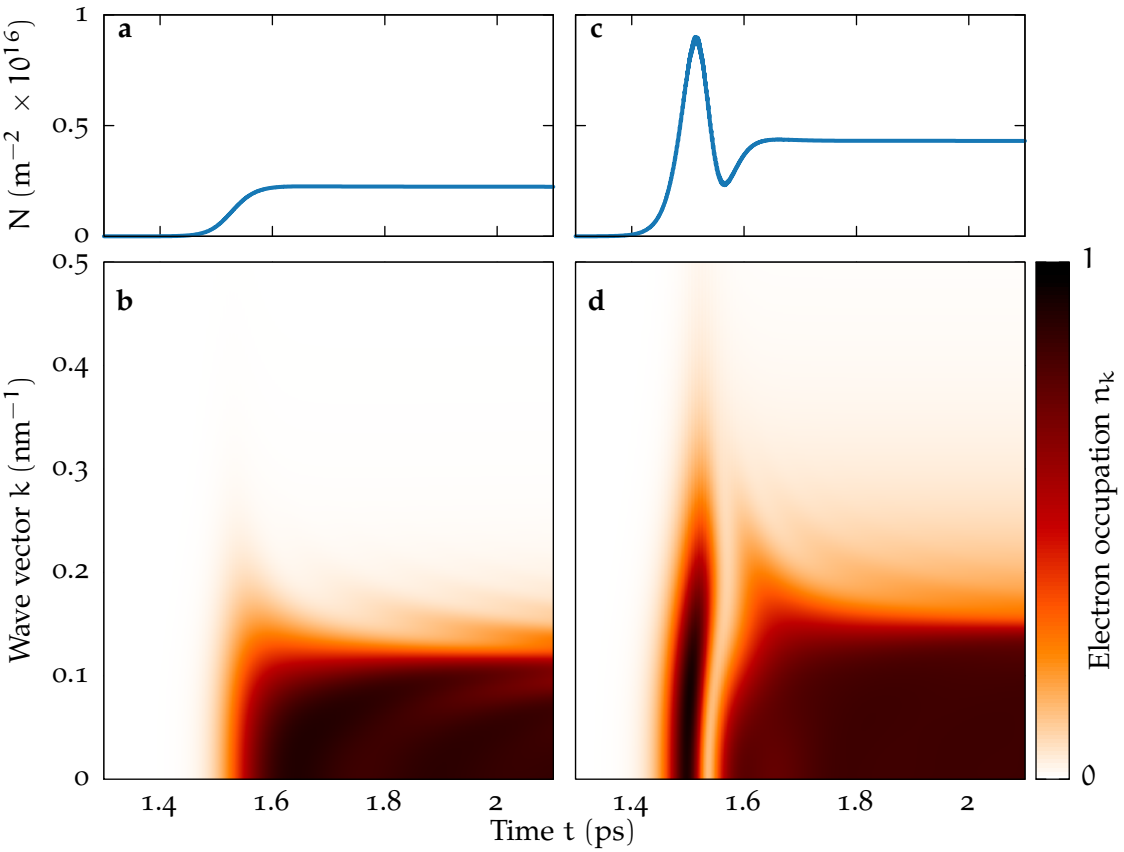


**Figure 3.9:** Macroscopic (a and c) and band resolved (b and d) dynamics of charge carriers in a QW excited outside of the linear regime. The system is excited via a 100 fs long, sech-shaped pulse whose peak reaches the QW position at t ≈ 1.5 ps. Panes a and b show the dynamic resulting from an optical pulse with peak intensity $I_0 \approx 5.1 \times 1011 W/m^2$, corresponding to an equivalent pulse area $\theta_2 = 0.4\pi$ in a two-level system. Panes c and d are the result of a 25 fold increase in the intensity of the excitation pulse, $I_0 \approx 1.28 \times 10^{13}$ W/m$^2$ and $\theta_2 = 2\pi$.

shows the occupation of the electronic states as a function of time and wave vector $k$. The population is located around the minimum of the conduction band, $k = 0$, and its distribution in $k$ space does not significantly change shape as the pulse traverses the material. Following the passing of the pulse, occupations remain almost constant as a consequence of the absence of intraband relaxation and the very slow nonradiative decay.

The exciting field used to produce the results in figs. 3.9c and 3.9d corresponds to an equivalent two-level pulse area $\theta_2 = 2\pi$ and therefore has a 25 fold increase in peak intensity, $I_0 \approx 1.28 \times 10^{13}\ \frac{W}{m^2}$. The total density in fig. 3.9c suggests that the carrier system as a whole still behaves similarly to a level system exhibiting Rabi oscillations. In contrast to the Rabi oscillations in a two-level system, however, the density does not decrease back to zero. A more complex picture emerges from the band resolved results in fig. 3.9d, where the population of carriers extends itself further from the centre of the band as compared to what was observed in fig. 3.9b for a weaker excitation. This is a consequence of the more intense pulse having stronger high energy components. Furthermore, every single state can be seen to behave similarly to an isolated two-level system subject to different excitation intensity, with lower $k$ states having a higher Rabi frequency. This behaviour is a consequence of two main effects; firstly the Rabi frequency acquires a strong $k$ dependence as a consequence of renormalisation induced by the Coulomb interaction. Secondly, Rabi oscillations occur at the generalized Rabi frequency,

$$\Omega_G = \sqrt{\Omega^2 - \Delta^2}\,, \tag{3.16}$$

and therefore decrease with increasing detuning, $\Delta$, of the pulse frequency from the optical transition. This is of particular importance when the excitation is redshifted from a parabolic band, as the detuning grows as $k^2$.

In order to investigate the generation of higher harmonics of the field, a set of simulations is performed by exciting the system with pulses of increasing strength. These pulses are initially taken to be strongly off-resonant with any optically active transition in the system, $\hbar\omega_p = \frac{1}{2}E_X$, so that results can be compared with the analytical ap-

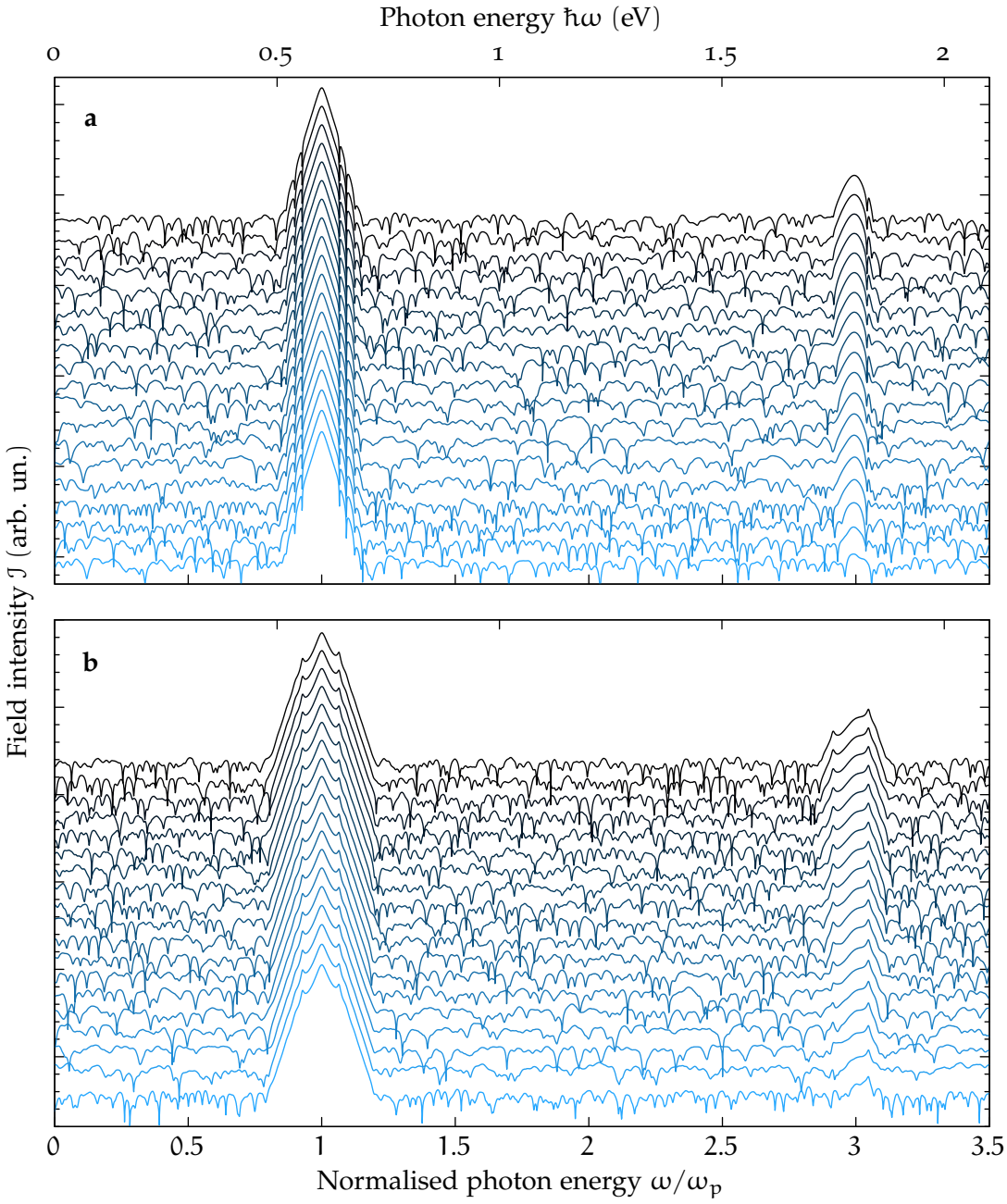


**Figure 3.10:** Intensity spectrum of the field reflected (a) and transmitted (b) from the QW+SESAM structure. The intensity of the pump is varied from an equivalent pulse area $\theta_2 = 2\pi$ (light blue line) up to $\theta_2 = 20\pi$ (black line) in steps of $\pi$. Following eq. 3.14, these correspond to peak intensities ranging from $I_0 \approx 1.28 \times 10^{13}$ W/m$^2$ to $I_0 \approx 1.28 \times 10^{15}$ W/m$^2$. The scale of the y axis is logarithmic and the lines are artificially offset to improve readability.

proach presented in section 2.5. Figure 3.10a shows on a logarithmic scale the spectra of reflected field intensity for increasing (bottom to top) excitation strength. For lower intensities, the only feature present is the spectrum of the exciting pulse, centred around $\frac{\omega}{\omega_p} = 1$. There is also some numerical noise that is several orders of magnitude weaker than the actual signal. As the excitation is increased in strength a second peak emerges over the background at three times the frequency of the exciting pulse, i.e., $\frac{\omega_{THG}}{\omega_p} = 3$, which is the signature of Third Harmonic Generation (THG) from the non-linear active material. For this range of excitation strength the generated third harmonic is several orders of magnitude smaller than the incoming pulse and thus its presence is not appreciable in the time domain signal of the reflected field. It is nevertheless possible to obtain the dynamics of the third harmonic field by applying a bandpass filter around the energy $E_{THG} = 3\hbar\omega_p$, which results in the pulse shown in fig. 3.11 (orange line). One can further look at the transmitted field, fig. 3.10b, where the spectral components of the exciting pulse are less prominent as they are located within the DBR stopband. This results in a lower intensity of the background and thus allows to identify THG for lower excitation strengths.

A more quantitative analysis of the intensity can be performed through the calculation of the THG integrated intensity and its dependence on the integrated intensity of the incoming pulse. In this context the integrated intensity is obtained from the frequency domain as

$$P = \int_{\mathcal{D}} \mathcal{I}(\omega)\, d\omega\,, \tag{3.17}$$

where the integration domain $\mathcal{D}$ is such as to include only one of the peaks shown in fig. 3.10[†]. The results for two different pumping configurations, one which is resonant with the exciton, $\hbar\omega_p = E_X$ (blue squares), and one with an off-resonant pump, $\hbar\omega_p = E_X/2$ (orange circles), are shown in fig. 3.12 on a double logarithmic scale. This shows

† Due to the unitarity of the Fourier transform, this spectral integral is equivalent to a time domain integral,

$$\int \mathcal{I}(\omega)\, d\omega = \frac{1}{c\mu_0}\int |\mathcal{E}(\omega)|^2\, d\omega = \frac{2\pi}{c\mu_0}\int E^2(t)\, dt\,,$$

where the time domain signal, $E(t)$, is assumed to be real.

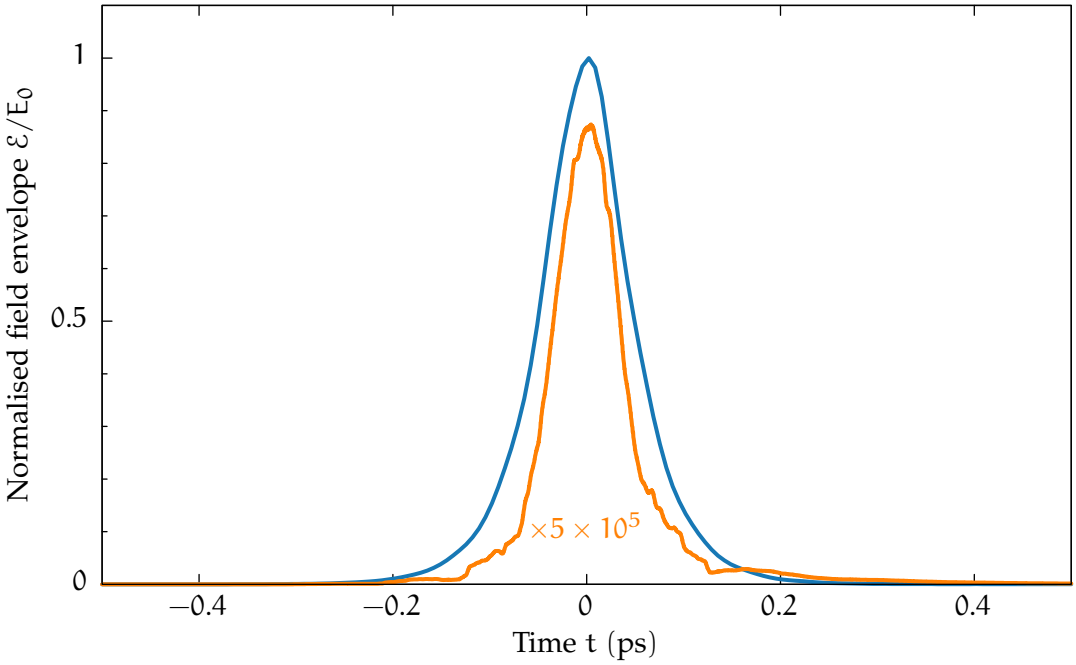


**Figure 3.11:** Field envelope of the excitation pulse (blue) divided by the peak field, $E_0$. Field envelope of the THG pulse (orange) obtained by filtering the total field reflected by the SESAM structure.

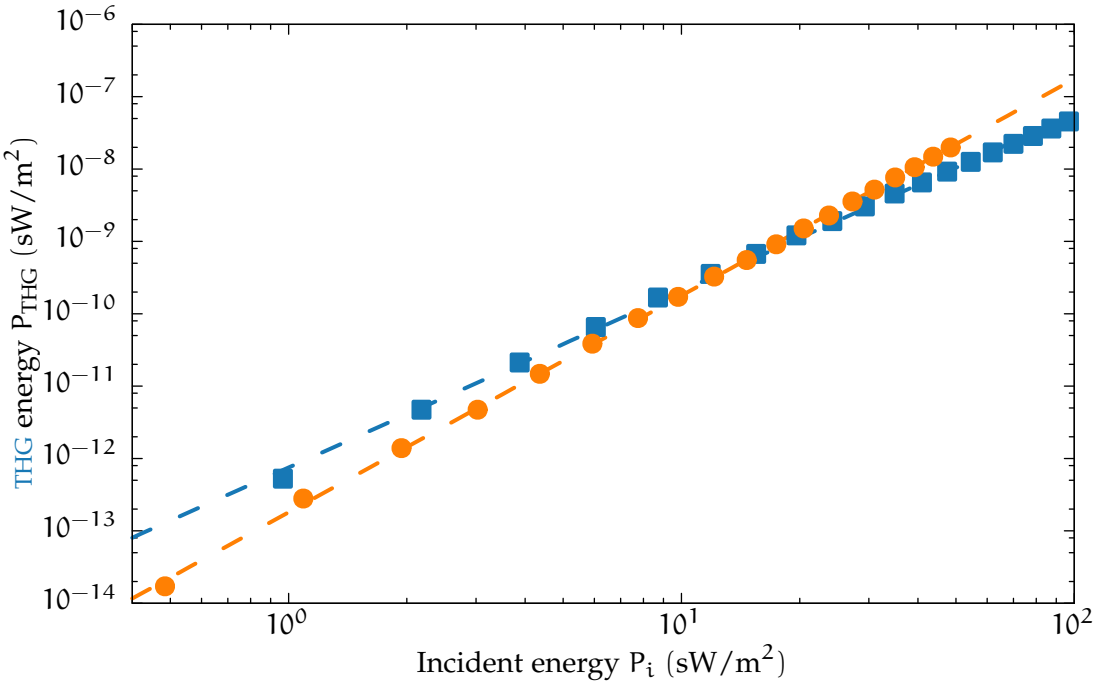


**Figure 3.12:** Integrated intensity of the THG signal, $P_{THG}$, as a function of excitation strength, i.e., integrated intensity of the incident pulse, $P_i$. Different colours correspond to an excitation resonant with the exciton (blue squares) and at half of the exciton energy (orange circles). The dashed lines are the corresponding linear fit for the two sets of data, following $\log(P_{THG}) = \nu \log(P_i) + \log(A)$.

that the total power of the generated third harmonic, $P_{THG}$, has a power law dependence on pumping strength,

$$P_{THG} = A \times P_f^{\nu} \,, \tag{3.18}$$

where $P_f$ is the total power reflected at the fundamental frequency†. The dashed lines in fig. 3.12 are the result of fitting eq. 3.18 to the integrated intensities calculated from the simulations. In the case of the off-resonant excitation fitting the data results in an exponent $\nu = 2.99 \pm 0.01$, which is consistent with an expansion over non-linear susceptibilities, as presented in section 2.5, in which the main contribution at $3\omega_p$ is given by the third order term, $\chi^{(3)}(3\omega, \omega, \omega, \omega)$. Conversely, when the pump is resonant with a transition of the system, the relationship between $P_i$ and $P_{THG}$ takes the form of a power law with a non-integer exponent, $\nu = 2.44 \pm 0.02$.

A similar analysis can be repeated while tuning the central wavelength of the pulse to obtain values of $\nu$ over a wide range of resonant and off-resonant excitations, which are shown in fig. 3.13 (blue squares). When the pump is far enough away from being resonant with any transition in the system, i.e., lying in the bandgap of the semiconductor, the value of $\nu$ approaches an asymptotic value of $\nu \sim 3$ which can be described as a non-linear series, eq. 2.47, dominated by the third order susceptibility, $\chi^{(3)}$[108, 109]. In this regime it is also possible to associate the $A$ coefficient of eq. 3.18 with the third order non-linear susceptibility. The orange circles in fig. 3.13 (right axis) are normalised such that $\chi^{(3)}(E_X/3\hbar) = 1$. They show a resonance when the pump is tuned to one-third of an optical transition of the system in qualitative agreement with eq. 2.50. Conversely, as the excitation gets closer to be resonant we observe a decrease in $\delta$ down to a value of about 2.4. A similar non-cubic dependence has been observed by Haase et al. [110] while performing four-wave mixing experiments on ZnSe QWs with the central laser energy close to resonance with the exciton.

To further investigate the origin of this subcubic dependence, it is useful to analyse the density of carriers generated by pulses with different detuning from the excitonic resonance. The total density of excited carriers left in the semiconductor after the pulse has

† This is done under the assumption that the fraction of the incident pulse which is absorbed is negligible, resulting in $P_f = P_i$, where $P_i$ is the integrated intensity of the incoming pulse.

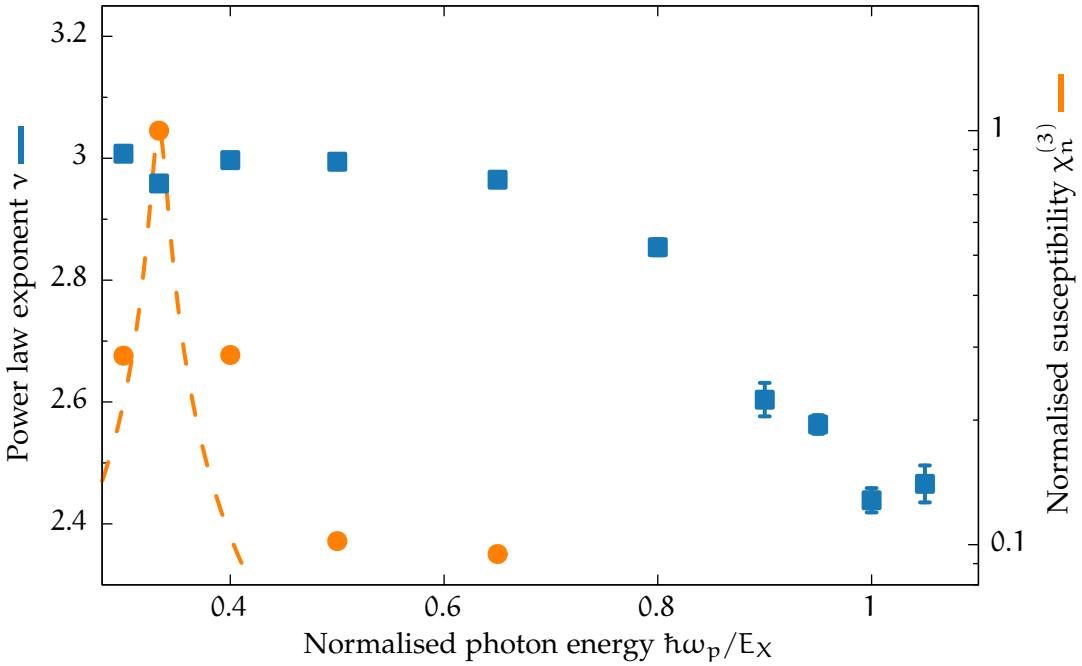


**Figure 3.13:** The blue squares show the frequency dependence of the exponent of the power law relating the integrated intensity of the THG, $P_{THG}$, with that of the pump, $P_i$. This dataset is obtained through a series of linear fits similar to what was shown in fig. 3.12 and the resulting errors are either shown or smaller than the square size. Within the range of excitation frequencies for which $\nu \sim 3$ the other fit coefficient is proportional to the third order susceptibility, $\sqrt{A} \propto \chi^{(2)}$. The orange circles show the frequency dependence of $\sqrt{A}$. For comparison the orange dashed line shows the analytical result for a two-level system with $\gamma \approx 20\gamma^p$, eq. 2.50.

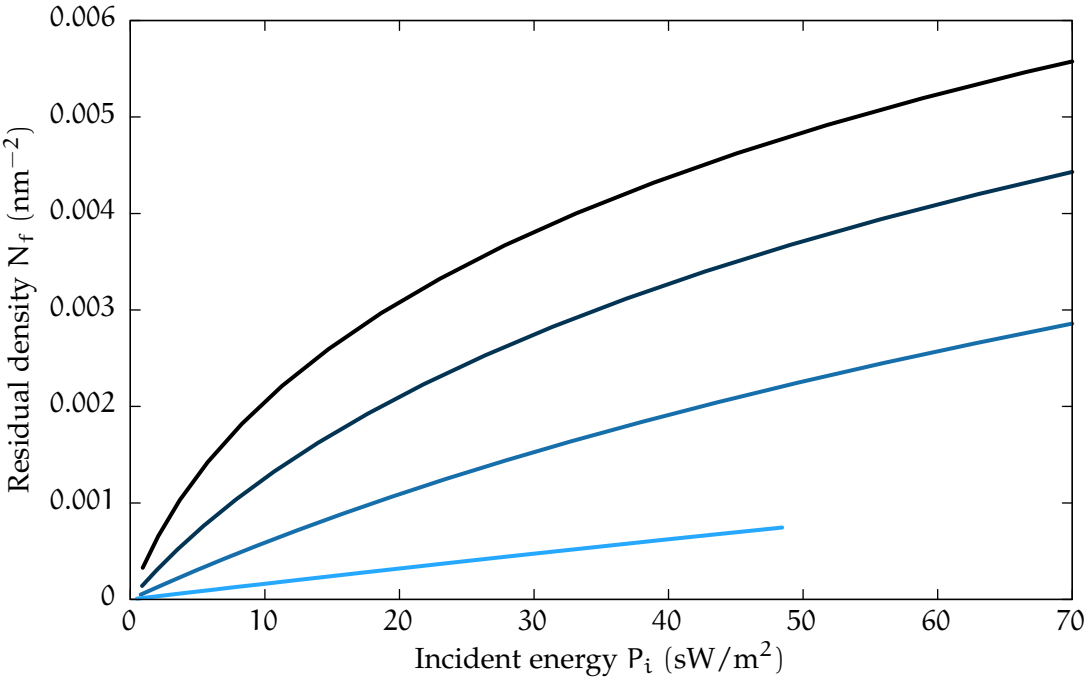


**Figure 3.14:** Density of carriers remaining in the QW as a function of pump strength for different excitation frequencies, $\hbar\omega_p/E_X = \{0.5, 0.8, 0.9, 0.95\}$. Values are increasing from light blue to black.

left the simulation domain is shown in fig. 3.14 as a function of the spectrally integrated intensity of the exciting pulse. This shows that the amount of excited carriers generated in the QW is significantly higher under resonant excitation, even for lower intensities, than what is obtained under non-resonant excitation. As a consequence of the higher number of excited carriers, near-resonant pumping shows a saturation behaviour (black line) which is weakened and shifted towards higher pumping strength as the pulse becomes off-resonant (colour changing towards light blue). This suggests that the subcubic behaviour is resulting from the presence of optically excited carriers. Indeed, the same analysis can be performed on the field transmitted through the SESAM, which shows a lower amount of background noise, where THG from a resonant excitation can be observed at much lower pumping strengths. From this it is possible to observe a crossover at $\mathcal{I}_0 \approx 10^{13}$ W/m$^2$ from the high-intensity subcubic behaviour, $\nu = 2.35 \pm 0.03$, into a third power regime, $\nu = 3.1 \pm 0.1$, for low excitation strength, as it is shown in fig. 3.15.

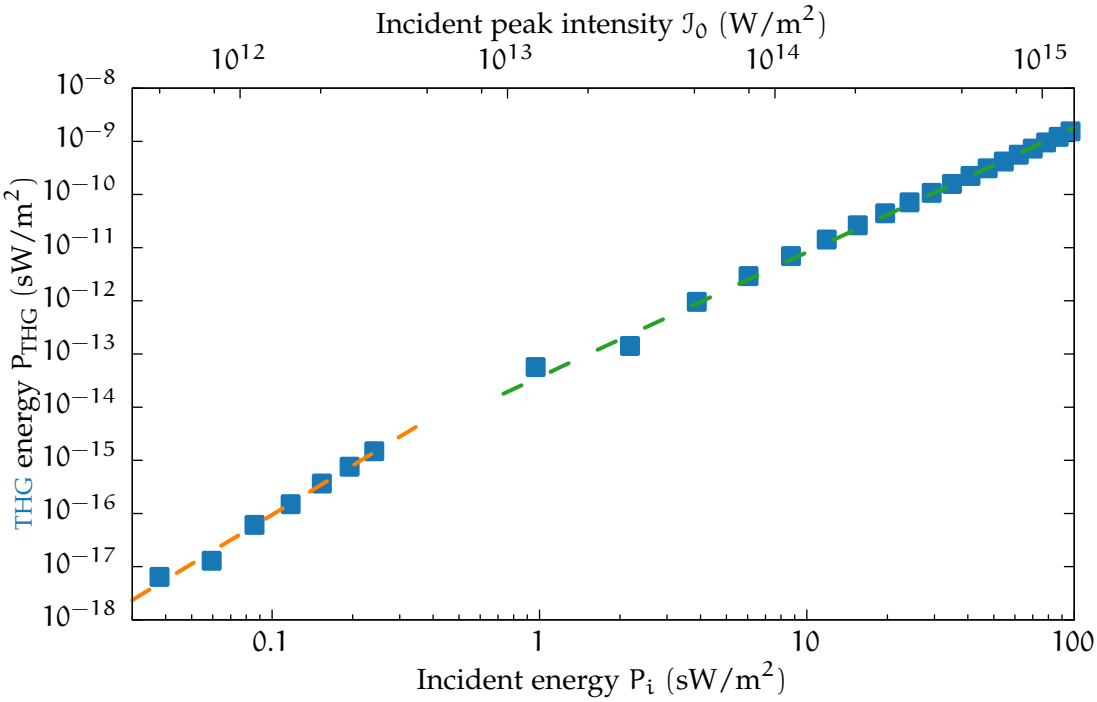


**Figure 3.15:** The blue squares show the integrated intensity of the THG signal, $P_{THG}$, in the resonant configuration. The integral is performed on the field transmitted through the SESAM structure, which has lower background noise. Two different linear regimes are observed for low (orange dashed line) and high (green dashed line) integrated intensity of the pump with exponents of $\nu = 3.1 \pm 0.1$ and $\nu = 2.35 \pm 0.03$, respectively.

## 3.3 TRANSITION METAL DICHALCOGENIDE MONOLAYERS

| | | |
|---|---|---|
| Monolayer thickness | $d$ | 0.312 nm |
| Effective electron mass | $m_e$ | 0.480 $m_0$ |
| Effective hole mass (A) | $m_h^A$ | 0.575 $m_0$ |
| Effective hole mass (B) | $m_h^B$ | 0.660 $m_0$ |
| Bandgap | $E_g$ | 2.84 eV |
| Valence band splitting | $\Delta_v$ | 160 meV |
| Conduction band splitting | $\Delta_c$ | 0 meV |
| Dipole matrix element | $\lvert\mu_x^{cv}\rvert = \lvert\mu_y^{cv}\rvert$ | 0.2 nm |
| Intraband dipole matrix element | $\lvert\mu_{x,y}^{c} - \mu_{x,y}^{v}\rvert$ | 0.02 nm |
| In-plane dielectric constant | $\varepsilon_\perp$ | 12 |
| Polarisation dephasing | $\gamma^p$ | 1/30 fs$^{-1}$ |
| Number of sampling points in k space | $N_k$ | 600 |
| Wave vector cut-off | $k_c$ | 2 nm$^{-1}$ |
| Spatial step of FDTD grid | $\Delta_x$ | 5 nm |
| Temporal step of FDTD grid | $\Delta_t$ | 0.0167 fs |

**Table 3.3:** Parameters of a $MoS_2$ monolayer at $T = 300$ K, with $m_0$ being the free electron mass

This section is focussed on the calculation of the linear and non-linear response from a $MoS_2$ monolayer, which is characterised via the parameters listed in table 3.3. This is a representative of a novel class of materials that have attracted a lot of interest since the discovery that reducing a $MoS_2$ crystal to a single monolayer blueshifts one of the bands responsible for the indirect gap observed in bulk form. This results in the emergence of a direct gap located at the K and K′ points of the reciprocal lattice of the hexagonal crystal[39, 41, 42, 44]. Some characteristics that make this class of materials very appealing are the very strongly bound excitons[45], the presence of a spin-orbit induced splitting of the conduction and valence bands[57], the possibility to selectively couple with carriers in the K or K′ valleys by controlling the polarisation of light[49] as well as the existence of a large class of these materials with very different parameters[111]. Lastly, a very strong Second Harmonic Generation (SHG), with a marked dependence on the excitation frequency, arises when these materials are reduced to thin, odd-layered films[66, 73].

Section 2.7 shows how the model that we previously used to describe QWs can be extended to this class of materials and how the relevant parameters can be derived.

Here we want to quickly stress some of the qualitative differences. Within the dipole approximation, the optical selection rules are entirely contained in the interband dipole matrix elements, $\boldsymbol{\mu}^{cv}_{s,\xi}$, where we are neglecting the dependence on $\mathbf{k}$ and $s$ ($\xi$) is the spin (valley) index. To account for the valley dependent coupling to circularly polarised light, we use $\boldsymbol{\mu}^{cv}_{s,K} = \left(\mu^{cv}_x, i\mu^{cv}_y, 0\right)$ and $\boldsymbol{\mu}_{s,K'} = \left(\mu^{cv}_x, -i\mu^{cv}_y, 0\right)$ with $\mu^{cv}_{x/y} \in \mathbb{R}$. As it was discussed in section 2.5 a Maxwell-Bloch description of a level system does not present any even order non-linearity, with the only exception when a set of three levels ($a$, $b$ and $c$) is present such that $E_b - E_a \approx E_c - E_b$ and thus $E_c - E_a \approx 2\left(E_b - E_a\right)$ and the system is resonantly excited at the $a \to b$ transition. This is in contrast with the case of a system lacking inversion symmetry, as it is the case for the TMDC monolayers. For such a system it is possible to find states in the valence (conduction) band that have a permanent dipole moment, $\boldsymbol{\mu}^{v}_{s,\xi,\mathbf{k}} = \langle v, s, \xi, \mathbf{k} | \mathbf{r} | v, s, \xi, \mathbf{k}\rangle$. The resulting correction to the equations of motion, cf. eq. 2.54c, introduces even order non-linearity in the model, similarly to what was shown by Tsang, Ahn, and Chuang [95] for a tilted QW. Here we will show results corresponding to the simplest case of a constant permanent dipole, i.e., $\boldsymbol{\mu}^{c}_{s,\xi,\mathbf{k}} = (0, \mu^c, 0)$, but the inclusion of more sophisticated parameters can be used to describe more complex features, like polarisation asymmetry[74, 112] or SHG generation from slightly misaligned stacks[113, 114].

### 3.3.1 Linear response

Similarly to what was done in section 3.1 the linear optical response of the TMDC monolayer is investigated with a weak circularly polarised pulse,

$$\mathbf{E}(t) = E_0 \operatorname{sech}\left(\frac{t}{\tau}\right)\left(\mathbf{u}_x \cos\left(\omega_p t\right) + \mathbf{u}_y \cos\left(\omega_p t + \sigma\frac{\pi}{2}\right)\right) , \tag{3.19}$$

where $\sigma = 1$ ($\sigma = -1$) results in a right-handed (left-handed) circularly polarised wave as defined from the point of view of the source. Following the complex nature of the dipole matrix element of the TMDC monolayer, as discussed in section 2.7, the handiness

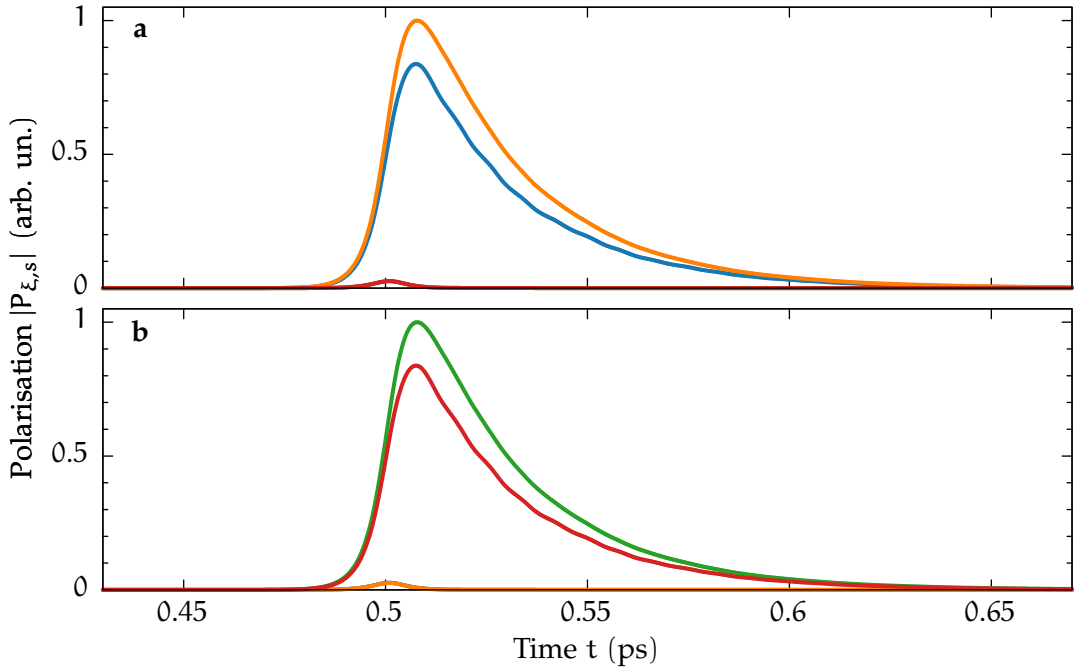


**Figure 3.16:** Time evolution of the polarisation, $P_{\xi,s}$ in a band, s, and valley, $\xi$, resolved fashion when probed with a right-handed (a) or a left-handed (b) polarised pulse. The line colour identifies a valley spin combination as follows; blue, K ↑; orange, K ↓; green, K′ ↑; red, K′ ↓.

of the pulse determines which valley is coupling to the optical excitation. This can be easily assessed in a computational experiment by inspecting the band ($s$) and valley ($\xi$) resolved polarisation,

$$P_{s,\xi}(t) = \sum_{\mathbf{k}} \mathbf{M}^{*}_{\mathbf{k}} p_{s,\xi,\mathbf{k}}(t) \ , \tag{3.20}$$

whose absolute value is shown in fig. 3.16a and fig. 3.16b for $\sigma = 1$ and $\sigma = -1$ respectively. These show that polarisation is mainly created in the K (blue, $s = \uparrow$, and orange, $s = \downarrow$, lines) or K′ (green, $s = \uparrow$, and red, $s = \downarrow$) valleys as a consequence of the polarisation of the exciting pulse, while polarisation in the opposite valley is more than one order of magnitude lower. Furthermore, the K (K′) valley dynamic in fig. 3.16a and the K′ (K) valley dynamic in fig. 3.16b are equivalent with the exception of the inversion of the two spin-split bands, cf. eqs. 2.97 and 2.98.

In order to probe the linear response of the lower energy band to band transitions as well as that of the exciton, the optical wavelength of the pulse in eq. 3.19, $\lambda_p = \frac{2\pi c}{\omega_p}$, is chosen to fall within the semiconductor bandgap. A short pulse is used, with a FWHM of $\Delta_t = 10$ fs, in order to access a broad spectral region, $\hbar\Delta_\omega = 0.29$ eV, within a single simulation. The linear absorption of a free-standing monolayer of $MoS_2$ is shown in fig. 3.17a (blue line). The absorption spectrum exhibits two pronounced peaks at $E_{X,A} \approx 1.90$ eV and $E_{X,B} \approx 2.05$ eV, which are attributed to the two excitons that are formed by the two spin-split bands and are commonly named A (lower energy) and B (higher energy) excitons. These quasiparticles are strongly bound due to the weak screening of the Coulomb interaction which is a consequence of the two-dimensional nature of these materials. The binding energies, $E_\xi = E_{g,\xi} - E_{X,\xi} \approx 850$ meV, are found to be independent of the index $\xi$ and to be comparable to results obtained using density functional theory (DFT)[59, 115–117]. The energetic splitting between the A and B exciton, $\Delta_X \approx 0.15$ meV, reflects mostly the spin-split of valence and conduction bands, $\Delta^{cv} = 0.16$ meV, with a small difference appearing due to the different effective masses of the two valence bands. The difference in peak amplitude can be traced back to different bandgaps. The high binding energy and weak screening of the Coulomb

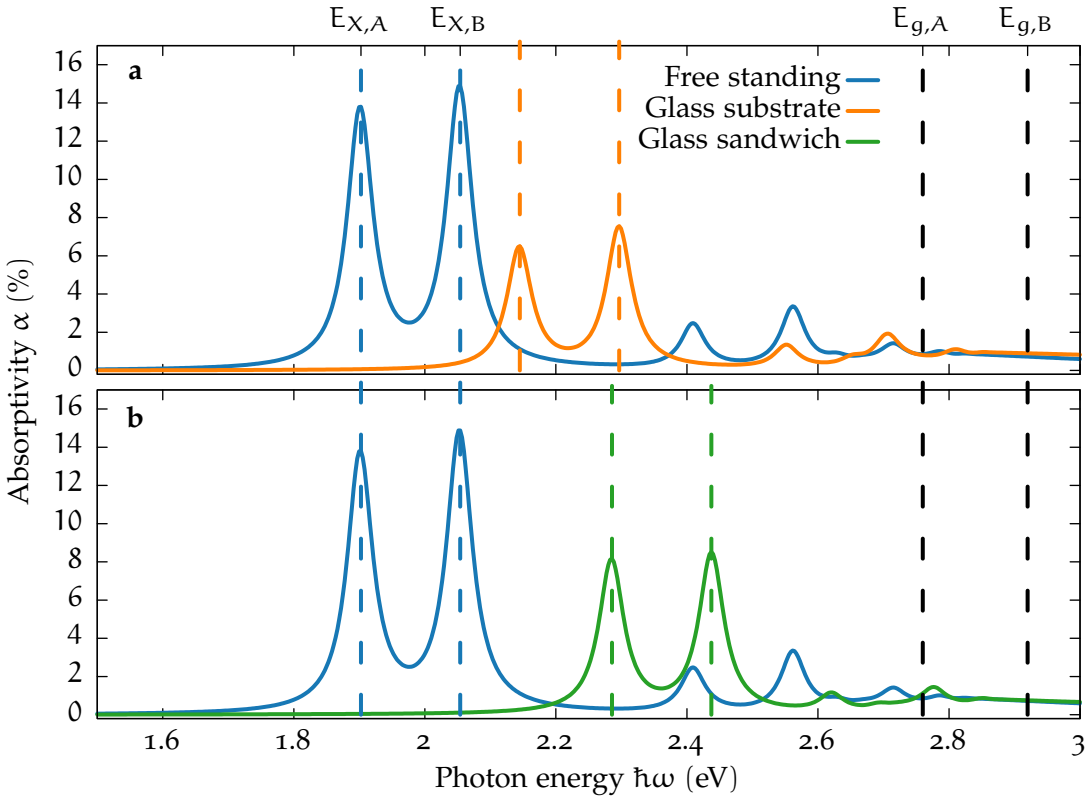


**Figure 3.17:** Absorption spectrum, $\alpha(\omega)$, of a single $MoS_2$ monolayer in different dielectric environments. The black dashed lines are located at the gap energy for the A and B bands, from which the exciton binding energy is measured. Pane a shows how the absorption is modified going from free-standing (blue) to a glass substrate (orange). Pane b shows how the absorption is modified going from free-standing (blue) to a monolayer sandwiched in glass (green). The vertical dashed lines are located at the exciton energies of the corresponding configurations.

interaction make it possible to observe absorption from the first excited state of the A (B) exciton at $E^*_{X,A} \approx 2.41$ eV ($E^*_{X,B} \approx 2.56$ eV) as well as from the second excited states.

Due to its two-dimensionality, the screening of the Coulomb interaction in a monolayer is strongly affected by the surrounding material, e.g., when the monolayer is lying on a substrate. The absorption spectrum of a $MoS_2$ monolayer on a glass substrate, $n_{SiO_2} = 1.50$, is shown in fig. 3.17a (orange line) and compared to the free-standing case (blue). As a consequence of the change in the environment, an additional screening of the Coulomb interaction is introduced and both excitons are blue-shifted by $\Delta E_{SiO_2} \approx 250$ meV to $E_{X,A,SiO_2} \approx 2.15$ eV and $E_{X,B,SiO_2} \approx 2.30$ eV, respectively. Another consequence of the screening of the Coulomb interaction from the environment is the renormalisation (redshift) of the bandgap which was observed in DFT calculations[43, 62, 69] as well as in experiments[71]. This effect, however, does not have a dynamical nature and can therefore be included in the present simulation framework by replacing the material parameters in table 3.3 with values fitted to DFT results. Furthermore, when a TMDC monolayer is to be embedded in a dielectric cavity it is necessary to know how the presence of both a sub- and superstrate affect the optical response. The absorption from a $MoS_2$ monolayer sandwiched between two glass layers is thus shown in fig. 3.17b (green line) in comparison to the previous cases. Here the superstrate further enhances the screening of the Coulomb interaction and accordingly the exciton resonances are again blue-shifted, resulting in $E_{X,A,2SiO_2} \approx 2.29$ eV and $E_{X,B,2SiO_2} \approx 2.44$ eV.

### 3.3.2 Harmonic generation from TMDC monolayers

Probing a free-standing TMDC monolayer with a (linearly polarised) intense pulse, peak intensity $\mathcal{I}_0 = 2.65$ W/m$^2$, results in a non-linear response analogously to what was observed for a QW in section 3.2. The pulse used to obtain the results in fig. 3.18 has an FWHM in time domain of $\Delta_t = 200$ fs and a carrier frequency lower than half of the A exciton energy to avoid the fundamental and SHG frequencies to be resonant with any transition of the electronic system. As a consequence of the broken inversion symme-

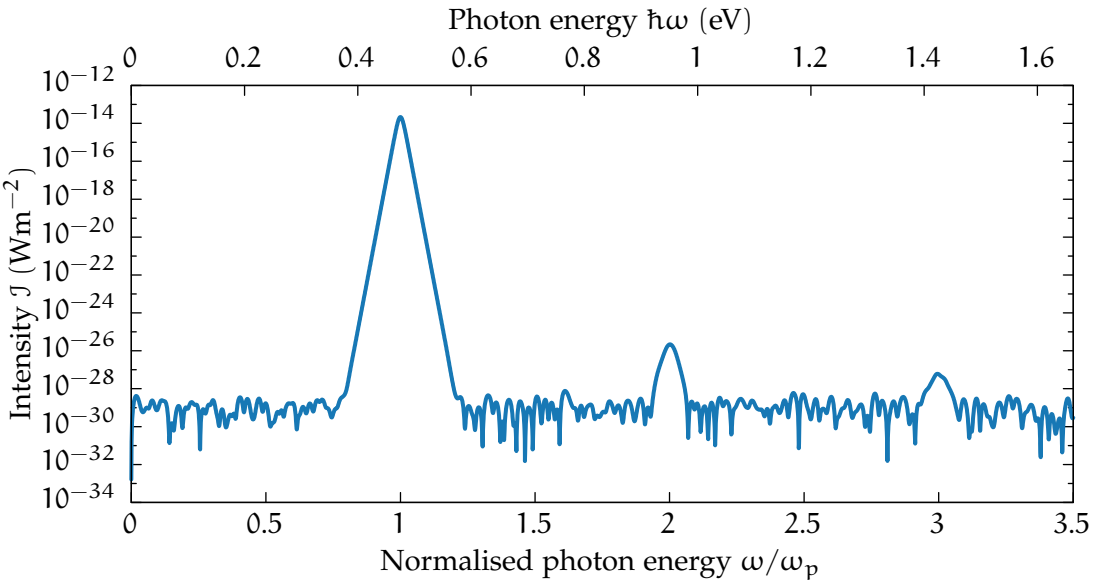


**Figure 3.18:** Field intensity spectrum of a strong non-resonant optical pulse after going through a free-standing TMDC monolayer. The scale of the y axis is logarithmic.

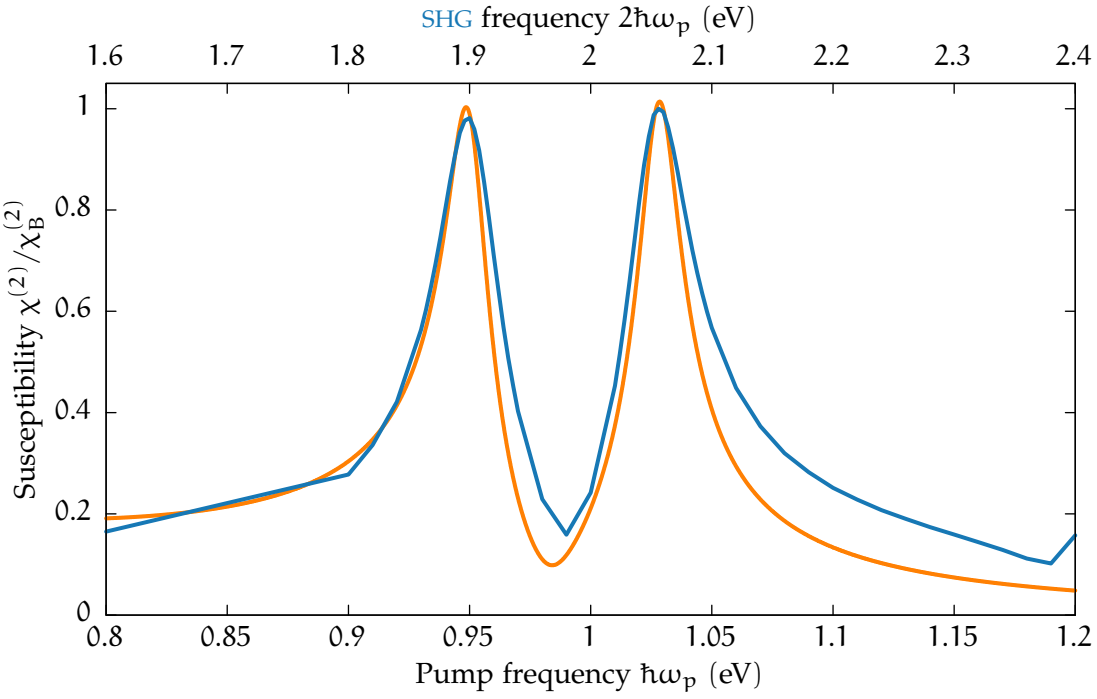


**Figure 3.19:** Frequency dependence of the second-order susceptibility (blue line) calculated from the intensity of SHG, $\chi^{(2)} \propto \sqrt{J(2\omega_p)}$. The orange line shows the analytical result for a pair of two-level systems with the same intraband dipole moment used for the TMDC and $\gamma \approx 0.4\gamma^p$.

try, which is represented in the model via a permanent dipole moment associated with conduction and valence band states, $M^{\nu}_{\xi,s,\mathbf{k}}$, it is possible to identify in fig. 3.18 a strong signal at twice the excitation frequency resulting from the SHG process. The material also presents THG as shown by the presence of the peak at $\omega \approx 3\omega_p$ which is significantly weaker than SHG reflecting the higher order of the process. As for the QW case, the generation of harmonics of the field fully emerges from the dynamical many-body simulation framework and the interaction of the light field with the Coulomb-interacting carriers in the semiconductor and therefore does not require any *a priori* knowledge about the system's non-linear behaviour. This aspect of the simulation is further emphasised by the emergence of resonances in the SHG efficiency at frequencies corresponding to half of the exciton energies, the so-called two-photon resonance condition. The data used for fig. 3.19 are obtained via a series of simulations in which the carrier frequency of the pump pulse incident on a free-standing TMDC layer is changed in the interval $\hbar\omega_p \in [0.8, 1.2]$ eV while all other parameters are kept constant. From the time traces of the transmitted field and their Fourier transform, the peak intensity of the SHG is extracted, $\mathcal{I}_2 = \mathcal{I}(2\omega_p)$. Assuming the signal at $2\omega_p$ to be entirely a consequence of second-order processes, it is possible to write

$$\left|\chi^{(2)}(\omega_p)\right|^2 = \varepsilon_0 \varepsilon \frac{\mathcal{I}_2(2\omega_p)}{\mathcal{I}_0(\omega_p)}\,, \tag{3.21}$$

where $\chi^{(2)}(\omega)$ is the second-order susceptibility that links the pumping field at $\omega$ with the response at $2\omega$ (cf. section 2.5). By further exploiting the fact that the intensity of the pump is kept constant throughout the sweep the blue line in fig. 3.19 is obtained as

$$\left|\frac{\chi^{(2)}(\omega_p)}{\chi^{(2)}_B}\right| = \sqrt{\frac{\mathcal{I}_2(2\omega_p)}{\mathcal{I}_{2,B}}}\,, \tag{3.22}$$

with $\chi^{(2)}_B = \chi^{(2)}(\omega_{X,B}/2)$. This frequency dependence in the non-linear susceptibility, as well as the enhancement from the excitons, have been recently observed in experiments by Wang et al. [66]. In this model these features result from the dynamics of the coupled field and carrier systems as the position of the excitonic peaks is not predetermined

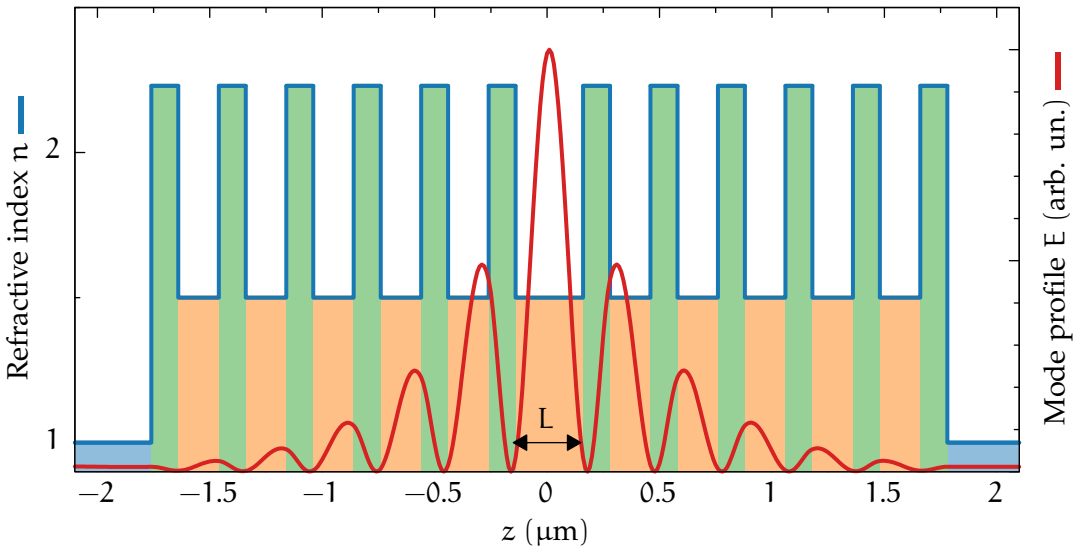


**Figure 3.20:** Schematic of the cavity used to enhance SHG in a $MoS_2$ monolayer. The cavity is composed of two DBR of alternating glass (orange) and silicon nitride (green) layers. The central section of the cavity is formed by a single glass layer of thickness L. The blue line shows the refractive index profile of the whole structure (left axis), while the red line shows the mode profile of the fundamental mode of the cavity.

but emerge from a self-consistent treatment. Figure 3.19 also shows the second-order susceptibility of a system composed of two independent two-level systems (orange line),

$$\left|\chi^{(2)}(\omega_p)\right| = \left|\chi_A^{(2)}(\omega_p) + \chi_B^{(2)}(\omega_p)\right| , \tag{3.23}$$

where $\chi_A^{(2)}$ ($\chi_B^{(2)}$) is from eq. 2.56 with $\Omega = \omega_{X,A}$ ($\Omega = \omega_{X,B}$) and a slower polarisation dephasing, $\gamma \approx 0.4\gamma_p$.

### 3.3.3 Environmental enhancement of second harmonic generation

It has further been shown in experiments that it is possible to obtain enhancement by a factor of over 1000 in the non-linear optical response by embedding a TMDC monolayer into a nanostructured photonic[77–79] or plasmonic[118] cavity. A simple but important example of such a nanostructured photonic cavity is the one used by Day et al. [79], which consists of two parallel DBRs formed by alternating layers of silicon nitrite ($SiN_x$, refractive index 2.23) and glass ($SiO_2$, refractive index 1.50) set at a distance L from each

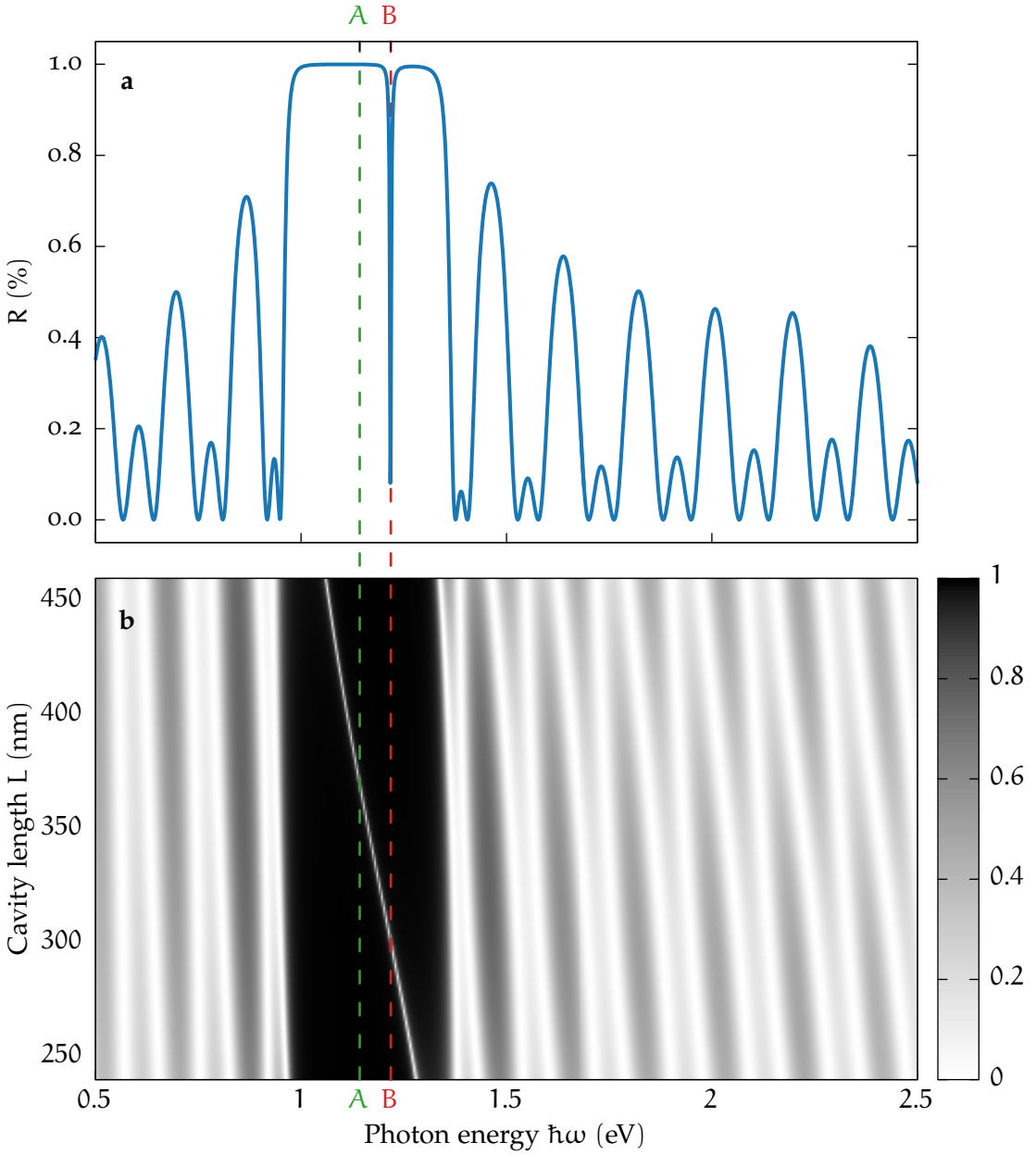


**Figure 3.21:** Reflection spectrum from the structure illustrated in fig. 3.20 for a cavity length $L = 300$ nm at which the cavity mode is resonant with the B exciton. The green (red) dashed line indicate the energy of the A (B) exciton for a monolayer sandwiched in glass, cf. fig. 3.17b. Pane b shows how the reflection spectrum changes with the length of the central part of the cavity, L.

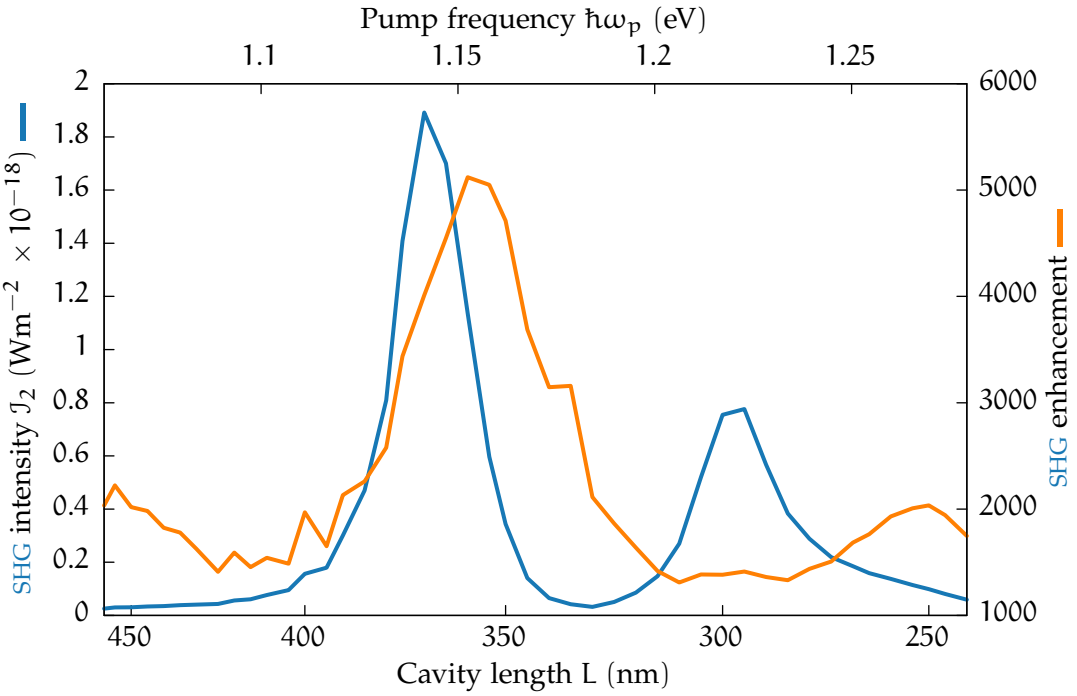


**Figure 3.22:** Intensity of SHG (blue line, left axis) as the length of the cavity is varied. The central frequency of the pulse is adjusted in order to maintain resonance with the cavity mode. The orange line (right axis) shows the enhancement of SHG arising from the presence of a confined electromagnetic mode.

other. The resulting refractive index profile, for $L = 300$ nm, is shown as a blue line in fig. 3.20 with the glass layers, $t = 180$ nm thick, highlighted in orange and the $SiN_x$ ones, $t = 120$ nm, in green. This DBR configuration presents a broad stopband around the two-photon resonance configuration of the A and B excitons of $MoS_2$, as it is shown by the reflection spectrum in fig. 3.21a. The resulting cavity supports a single localised mode with a high quality factor, $Q \approx 400$, corresponding to the narrow resonance in fig. 3.21a and the field profile shown in fig. 3.20 (red line). The energy of the single confined mode depends on the distance between the two mirrors as it is shown in fig. 3.21b, where the white diagonal line shows that the mode energy can be continuously tuned across the stop band and brought in and out of resonance with either the A or B excitons. If the cavity mode lies well within the stop band of the photonic structure, as it is the case in fig. 3.21b, the mode energy has an approximately linear dependence on L.

After introducing the TMDC monolayer at the centre of the cavity, i.e., where the field enhancement is the strongest, one can proceed to consider how the strength of the sec-

ond harmonic signal is affected by the new dielectric environment. Figure 3.22 shows the peak intensity of the SHG, $\mathcal{I}_2$, (blue line) as the cavity length is varied while the pump is kept resonant with the cavity mode energy in order to achieve high incoupling. The strong second harmonic signals observed for $L = 300$ nm and $L = 370$ nm are obtained with photon energies of $\hbar\omega_p \approx 1.22$ eV and $\hbar\omega_p \approx 1.14$ eV and correspond to the two-photon resonance of the B ($E_{X,B,2SiO_2}/2$) and A ($E_{X,A,2SiO_2}/2$) excitons, respectively. By comparing these results with what is observed for a TMDC embedded in a homogeneous glass system excited at the same frequencies it is possible to calculate the SHG enhancement from the structure,

$$\mathcal{S}(\omega) = \frac{\mathcal{I}_0(\omega)}{\mathcal{I}_{0,\text{hom.}}(\omega)} . \tag{3.24}$$

From fig. 3.22 (orange line) it can be seen that the enhancement has a peak around $\hbar\omega_p \approx 1.15$ eV where it reaches $\mathcal{S} \approx 5000$ which is comparable with experimental results reported by Yi et al. [78]. The position and relative narrowness of the peak in the enhancement explains the difference in SHG signal between the A and B excitons which can be observed in fig. 3.22 with respect to fig. 3.19.

One could expect a similar behaviour from a cavity whose mode is tuned at the second harmonic frequency, where the resulting increase in the photonic density of states could enhance SHG by providing a better coupling of the semiconductor polarisation into the field[78]. This can be tested by halving the thickness of the layers composing the DBR in fig. 3.20 which results in a blue shift of the photonic stop-band by a factor of 2. Setting the length of the central part of the cavity to $L = 185$ nm brings the fundamental mode of the cavity in resonance with the A exciton, i.e., the SHG when pumping at the two-photon resonance. The resulting second harmonic enhancement is much smaller, $\mathcal{S}_2 \approx 6$, in comparison with what can be achieved in the previous configuration.

One final remark can be made about the cavity induced enhancement of the second harmonic as well as the difference between second-order non-linearities in systems with and without inversion symmetry. As it was shown in section 3.3.3, the SHG from a system which lacks inversion symmetry, as a TMDC monolayer, is greatly enhanced by

the field enhancement at the pumping frequency whereas introducing a cavity resonant with the second harmonic frequency has a limited effect. To contrast this, one can consider the generation of a second harmonic of the field from centrosymmetric materials with equally spaced levels, which can be described via the three-level system discussed in section 2.5[119, 120]. By embedding such a system in the same cavities used in section 3.3.3 and performing the same analysis and comparison with a free space system, one can observe SHG enhancement factors of $\mathcal{S}_f \approx 2$ and $\mathcal{S}_2 \approx 25$ when the cavity is tuned at the fundamental or second harmonic frequencies, respectively. This difference in behaviour can be attributed to the different pumping configuration between the two systems, as the generation of the second harmonic in a centrosymmetric system is an intrinsically resonant phenomenon. Consequently, the SHG efficiency is affected by the occupation level of the involved states and can be improved via a faster out-coupling to the field, which attenuates the depletion of ground state carriers and mitigates the effect of saturable absorption. On the other hand for off-resonant SHG, which is only possible for systems lacking inversion symmetry, the excitation of carriers is much reduced and therefore does not present a limiting factor. This different behaviour for resonant and off-resonant harmonic generation is further exemplified by the results on frequency dependence of the THG in semiconductor QWs presented in section 3.2[1].

## 3.4 CONCLUSION

In this chapter we have shown how the combination of a dynamic full-wave and spatially resolved simulation of Maxwell's equations with a many-body band resolved Maxwell Bloch model can be used to investigate the linear response of different semiconductor systems. In particular, we highlighted how the microscopic nature of the active material model can provide a self-consistent description of the excitonic nature of the absorption as well as a tool to investigate the time- or frequency- domain behaviour of the quantum mechanical coherences induced by weak ultrashort pulses. Furthermore,

the time and space description of Maxwell's equations allows a consistent description of the response resulting from the combination of an active element, providing gain or absorption, with an electromagnetic cavity.

Under strong excitation we showed how this time domain model can provide a self-consistent non-linear response which goes beyond a simple description provided by using one, or even a finite sum, of non-linear susceptibilities. Indeed, when a pulse resonant with a transition is used to excite the system, the creation of excited carriers results in a saturation-like behaviour in the generated intensity of THG with respect to the pump intensity. This saturation-like behaviour strongly depends on the frequency and intensity of the exciting pulse and emerges from the time domain interplay between state occupations and coherences. An even more striking dependence on the exciting frequency is present when looking at SHG from TMDCs. As a consequence of the strong Coulomb interaction in materials like $MoS_2$, the strongly bound excitons are spectrally well separated from the interband transition region and feature prominently in the linear and non-linear optical response. The consistent treatment of field and carrier dynamics provides a way to calculate SHG enhancement factors which are consistent with experimental observations[66, 78]. By extending the electromagnetic simulation domain to two or three dimensions, the method presented in this work can be an ideal platform to explore and design complex photonic[77] or plasmonic[118] structures which employ TMDC monolayers to achieve novel optical functionalities.

# 4 Semiconductor Laser Near-Field Dynamics

In this chapter we apply the model presented in chapter 2 to the investigation of a Quantum Well (QW) edge emitting laser. In such a system the electrically pumped semiconductor QW provides spatially distributed optical gain for the lasing process. The model discussed in chapter 2 provides a consistent spatio-temporal description of the elements involved in the lasing process, optical fields and gain medium, as well as their interaction. In particular, we do not rely on a set of previously determined modes but the modes emerge from the spatial description of the electromagnetic fields. By going beyond the slowly-varying envelope approximation we can investigate how the emergence of wavelength-sized structures in the carrier density affects the stability of the laser output. Furthermore, the QW model detailed in chapters 2 and 3 is capable of reproducing several characteristic features of the semiconductor medium, e.g., a broad and asymmetric spectrum. These elements are key in allowing us to investigate the spatio-temporal phenomena which produce instabilities in the laser output.

The main results presented in this chapter have been published in Bittner et al. [2] while all the material presented was used in the discussion leading to the paper publication.

## 4.1 Theory Addendum

Due to the geometry of the system we are studying, it is necessary to include an active material over an extended spatial region. Consequently, one has to solve the Auxiliary Differential Equation (ADE) component of the Finite Difference Time Domain (FDTD) model at every spatial cell in order to achieve a spatially resolved polarisation and occu-

pations dynamic. Using the full model presented in chapter 2 over a 1D strip of several μm length is prohibitively expensive in terms of computation time and some simplifications are needed. We thus aim for a model that incorporates enough complexity to calculate the full field dynamics without slowly varying envelope approximation or an expansion of rate equations. It should also go beyond the simple four-level model that is limited to Lorentzian line-shapes and has previously been used in conjunction with FDTD calculations.

As a first step we remove the Coulomb interaction from the model and go back to an independent electron model described by the Maxwell-Bloch equations, cf. eq. 2.45. This is justified as semiconductor lasers operate in high-density conditions such that screening of the Coulomb interaction is very effective. In this regime the exciton resonance is bleached and the carrier-carrier interaction is mainly responsible for bandgap renormalisation[6, Sec. 5.3], which can be introduced by changing the parameters of the model, similarly to what was discussed in section 3.3.1. Under this assumption it is convenient to convert the first order differential equation describing the time evolution of the complex polarisation into a second order one for the real part of the polarisation

$$\left(\partial_t^2 + 2\gamma\partial_t + \overline{\omega}_{\mathbf{k}}^2\right)\widetilde{p}_{\mathbf{k}}(\mathbf{r}) = \frac{e\omega_{\mathbf{k}}\boldsymbol{\mu}\cdot\mathbf{E}(\mathbf{r},t)}{\hbar}\left(1 - n_{\mathbf{k}}^{e}(\mathbf{r}) - n_{\mathbf{k}}^{h}(\mathbf{r})\right) , \tag{4.1}$$

with the polarisation dephasing rate, $\gamma$ and $\overline{\omega}_{\mathbf{k}}^2 = \omega_{\mathbf{k}}^2 + \gamma^2$. Furthermore, all dynamical variables are now parametrised by the position, $\mathbf{r}$.

The presence of the Coulomb interaction has the further effect of introducing a fast intraband relaxation towards an equilibrium, i.e., Fermi-Dirac, distribution of electrons and holes, as it was discussed in section 2.6.1. These carrier-carrier scattering processes happen on a strongly subpicosecond time scale and are therefore much faster than the dynamics of the electric field inside the cavity. Due to this time scale difference, we assume the carriers to always be in a quasi-equilibrium state characterised by the electron (hole) chemical potential, $\mu^{\nu}(\mathbf{r},t)$. Without any transport included in the model, the number of electrons and holes excited at any position is the same, resulting in a common carrier density, $N(\mathbf{r},t)$. The time evolution of the density can be obtained by

| | | |
|---|---|---|
| QW width | $w$ | 10 nm |
| Effective electron mass | $m_e$ | 0.063 $m_0$ |
| Effective hole mass | $m_h$ | 0.51 $m_0$ |
| Bandgap | $E_g$ | 1.424 eV |
| First electron subband energy | $E_1^e$ | 0.034 eV |
| First hole subband energy | $E_1^h$ | 0.006 eV |
| Dipole matrix element | $\mu$ | 0.5 nm |
| Dipole renormalisation value | $\mu^*$ | 0.9848 |
| Polarisation dephasing | $\gamma^p$ | 12 $ps^{-1}$ |
| QW refractive index | $n_{QW}$ | 3.5 |
| Initial excitation density | $N_e$ | $3 \times 10^{16}$ $m^{-2}$ |
| Number of sampling points in k space | $N_k$ | 31 |
| Energy cut-off | $E_c$ | 1.662 eV |
| Spatial step of FDTD grid | $\Delta_x$ | 20 nm |
| Temporal step of FDTD grid | $\Delta_t$ | 0.0666 fs |

**Table 4.1:** Parameters used to simulate the dynamics of carriers in a semiconductor QW. These parameters are valid at $T \approx 300$ K.

integrating eqs. 2.45a and 2.45b over $\mathbf{k}$, following the derivation in Böhringer and Hess [31, 32],

$$\begin{aligned} \partial_t N(\mathbf{r},t) &= \int \partial_t n_{\mathbf{k}}^{\nu}(\mathbf{r},t)\,d\mathbf{k} - \gamma_{nr} N(\mathbf{r},t) \\ &= \mathbf{E}(\mathbf{r},t)\cdot(\partial_t \mathbf{Q}(\mathbf{r},t) + \gamma \mathbf{Q}(\mathbf{r},t)) - \gamma_{nr} N(\mathbf{r},t)\ , \end{aligned} \tag{4.2}$$

with the non-radiative decay rate, $\gamma_{nr}$, and

$$\mathbf{Q}(\mathbf{r},t) = 2e\mu \int \frac{\widetilde{p}_{\mathbf{k}}(\mathbf{r},t)}{\hbar\omega_{\mathbf{k}}} d\mathbf{k}\ . \tag{4.3}$$

For a 2D electron gas the chemical potential can then be calculated exactly from the macroscopic density as

$$\beta\mu^{\nu}(\mathbf{r},t) = \ln\left(e^{\hbar^2\beta\pi N(\mathbf{r},t)/m_{\nu}} - 1\right) \tag{4.4}$$

with the electron (hole) effective mass, $m_e$ ($m_h$) and the temperature of the carrier system, $T = \frac{1}{k_B\beta}$, which is taken to be constant.

Lastly, a way to excite carriers into the conduction band is needed to generate inversion and thus provide a source of electromagnetic gain. This is needed as a way to provide energy to the system and balance the radiative losses. In a QW edge emitting

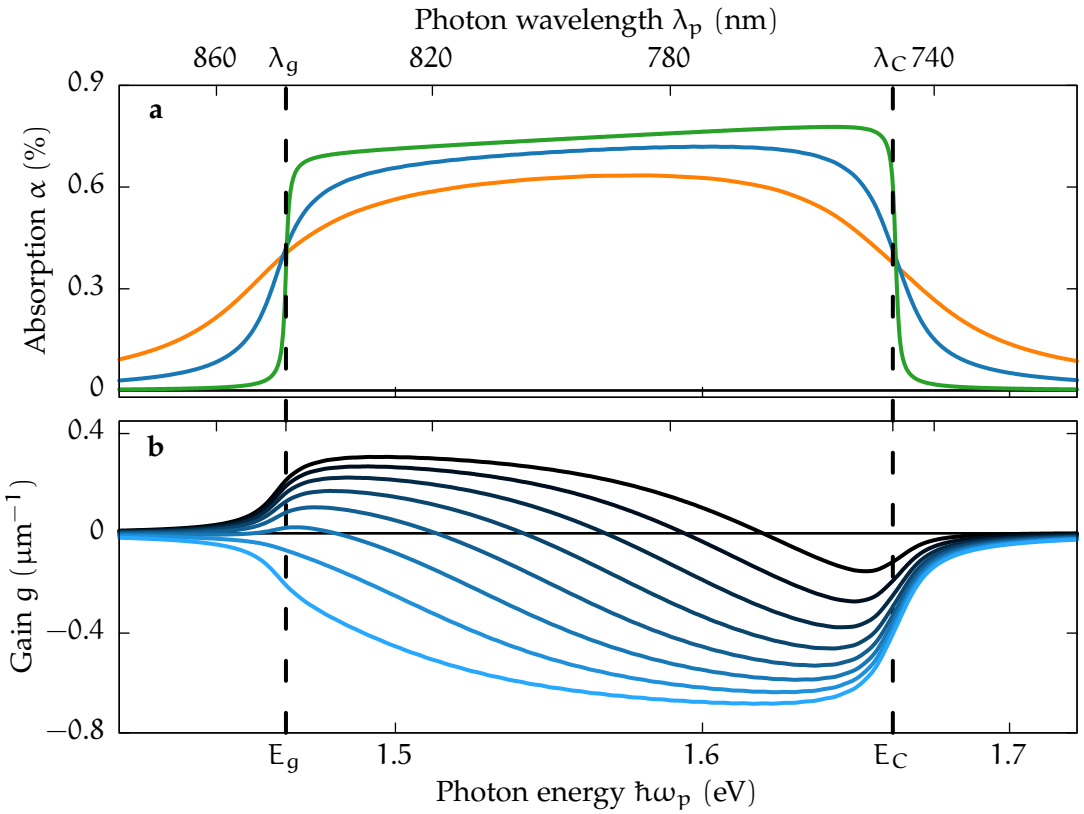


**Figure 4.1:** Pane a: absorption spectrum, $\alpha(\omega)$, of a single QW embedded in an infinite passive material with the same refractive index as its barriers. Different lines correspond to different number of sampling points, $N_k = 11$ (orange), $N_k = 31$ (blue) and $N_k = 301$ (green). Pane b: gain spectrum, $g(\omega) = \log(1 - \alpha(\omega))/L$, of an extended QW system of length L. Different lines correspond to different carrier densities, $N = \{0.5, 1, 1.5, 2, 2.5, 3, 3.5, 4\} \times 10^{16}$ m$^{-2}$, with values increasing from light blue to black. The vertical dashed line on the left is located at the gap energy, $E_g$, while the one on the right marks the cut-off energy, $E_c$.

laser, this is achieved through electrical pumping which results in a contribution to the macroscopic carrier density

$$\partial_t N(\mathbf{r}, t)\Big|_{\text{pump}} = \frac{J}{e}, \tag{4.5}$$

where J is the current density flowing through the active medium[†]. This assumes that the carriers injected through the electric contacts reach the QW layer following a thermal quasi-equilibrium distribution[31].

† This approach can be easily generalised to a spatially inhomogeneous pumping current, $J(\mathbf{r})$.

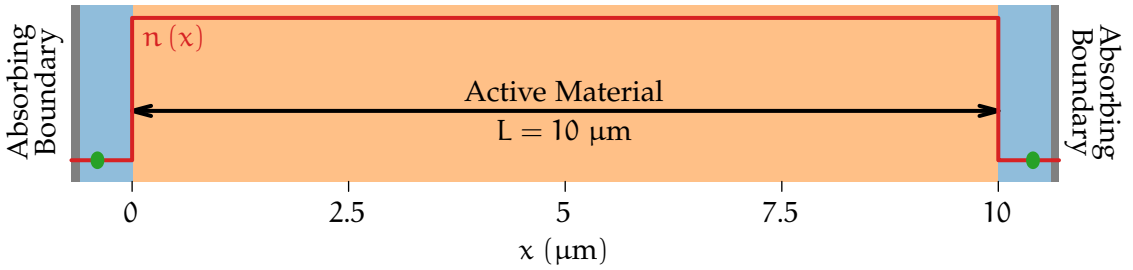


**Figure 4.2:** Schematic of the structure used for lasing simulations. The orange shaded area is the semiconductor containing the active medium and has a length $L = 10\ \mu m$ and refractive index $n = 3.5$. The two blue shaded regions are small air gaps, $n = 1$, around the laser. The grey regions represent the open boundaries of the system. The red line shows the refractive index profile, $n(x)$.

We set the discretisation points so that they are equally spaced in energy and change all k-space summations into energy integrals via the density of states,

$$\mathcal{D}(\hbar\omega) = \frac{m^*}{\pi}\,, \tag{4.6}$$

with the reduced mass of the electron-hole system, $m^*$. As a consequence of the parabolic nature of the band we can use fewer energy points to represent the semiconductor band structure and thus achieve a more efficient description of the active system. Furthermore, this suppresses the numerical oscillations in the high energy part of the band that can be seen in fig. 3.1b and allows us to set a lower cut-off energy (right-hand black line in fig. 4.1). Figure 4.1a shows how the linear absorption spectrum of the QW changes as $N_k$ is set to 10 (orange), 30 (blue) and 300 (green). Figure 4.1b shows the gain coefficient spectrum of the QW,

$$g(\omega) = \frac{1}{L}\log\left(1 - \alpha(\omega)\right)\,, \tag{4.7}$$

with the length of the semiconductor system, L, and the absorption spectrum, $\alpha(\omega)$, as defined in eq. 3.5. As the carrier density is increased from $N = 0.5 \times 10^{16}\ m^{-2}$ (light blue) to $N = 4 \times 10^{16}\ m^{-2}$ (black) the gain region in the spectrum broadens, while absorption is pushed towards higher energies. In particular, we observe that there is no gain up to $N_0 \approx 1.5 \times 10^{16}\ m^{-2}$.

The simulations presented in the following sections are all performed in a one-dimensional domain. A schematic of the structure is presented in fig. 4.2, where the red line shows the refractive index profile, $n(x)$, across the whole simulation domain. The active region (orange shaded region) representing the QW is 10 μm long and has a refractive index of $n_{QW}$. The presence of Absorbing boundary conditions (ABC) layers (grey shaded region) at both ends allows energy to flow outside of the simulation domain, effectively representing an open system immersed in air. The time traces of the emitted field are recorded in the 0.6 μm of air that separate the active material from the ABCs (marked by the green spots). As a consequence of the symmetry of the system, the field recorded on the left-hand side of the structure is equivalent to the one recorded on the right-hand side.

Since the description of the electromagnetic fields in the model is classical, there are no quantum fluctuations in the field to spontaneously start the emission process. Some spontaneous processes can be achieved in a semi-classical Maxwell-Bloch theory via the introduction of noise terms for a two or four level gain medium[121–124]. As an alternative, one can simply introduce some polarisation in the active material by introducing a weak optical pulse incident on the active medium. This is more efficient than introducing noise terms and is well suited for simulations performed above the lasing threshold, where the coherent processes dominate the dynamics[†].

## 4.2 ONE-DIMENSIONAL FABRY–PÉROT LASER DYNAMICS

We investigate the lasing dynamics of a QW edge emitting laser modelled according to the one-dimensional geometry depicted in fig. 4.2. In such a system the QW provides optical gain and a cavity is naturally formed from the reflection, $R \approx 0.3$, at the boundary between the high refractive index semiconductor and the surrounding medium. This re-

† As a test we performed the same simulation multiple times with different choices of *seed* pulse and observed no difference.

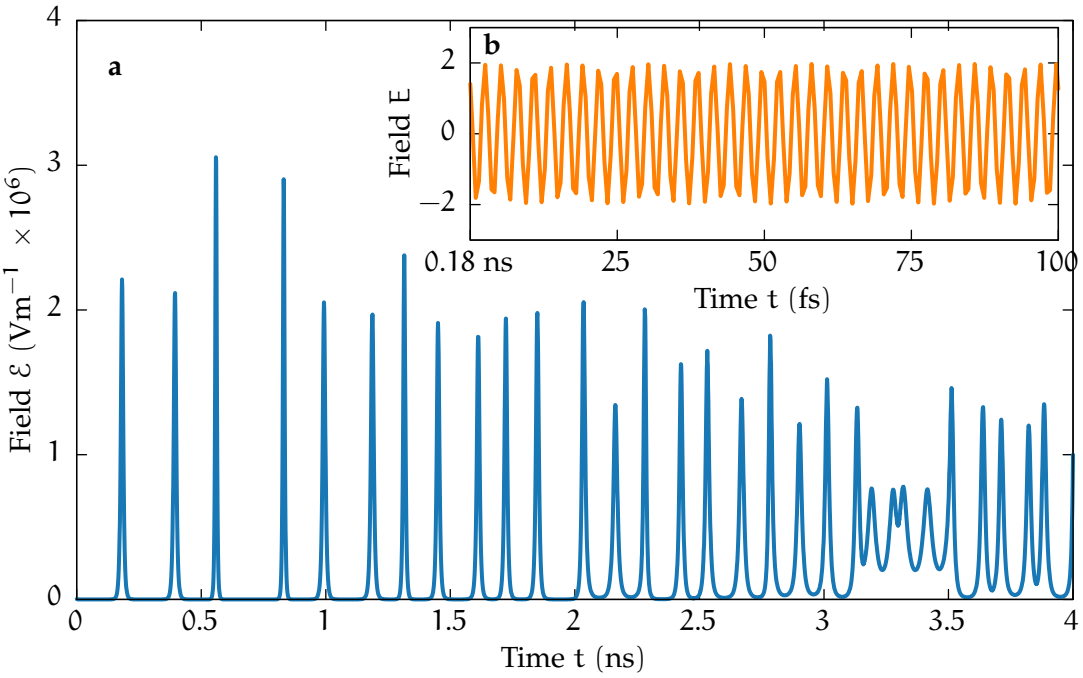


**Figure 4.3:** Full wave (b) and envelope (a) of the output field from the QW edge emitting laser. The inset b shows a 100 fs segment of the emission starting from 0.18 ns, which is all contained within the first pulse shown in a.

sults in a Fabry–Pérot (FP) cavity which supports a set of spatially homogeneous modes with Lorentzian spectral line shape and a constant frequency spacing,

$$\Delta\nu_{\mathrm{FSR}} \approx 4.3\ \mathrm{THz} \approx \frac{0.018}{h}\ \mathrm{eV}\ . \tag{4.8}$$

We start the investigation with an arbitrary pump intensity and set a current density of $J = 5\ \mathrm{A/mm^2}$ and an initially homogeneous density of excited carriers, $N = 3 \times 10^{16}\ \mathrm{m^{-2}}$. Although it would be possible to start from a lower value, characteristic of an intrinsic semiconductor, there is no interesting dynamics happening until the system is inverted. The emission is observed on the right-hand side of the structure, $x = 10.4\ \mu\mathrm{m}$, by recording a time trace of the electric field. Since the method used to perform the simulation directly solves Maxwell's equations in the time domain, the recorded time traces contain variations on two very different time scales, as can be seen in fig. 4.3. On a femtosecond time scale, cf. fig. 4.3b, the electric field is oscillating at one

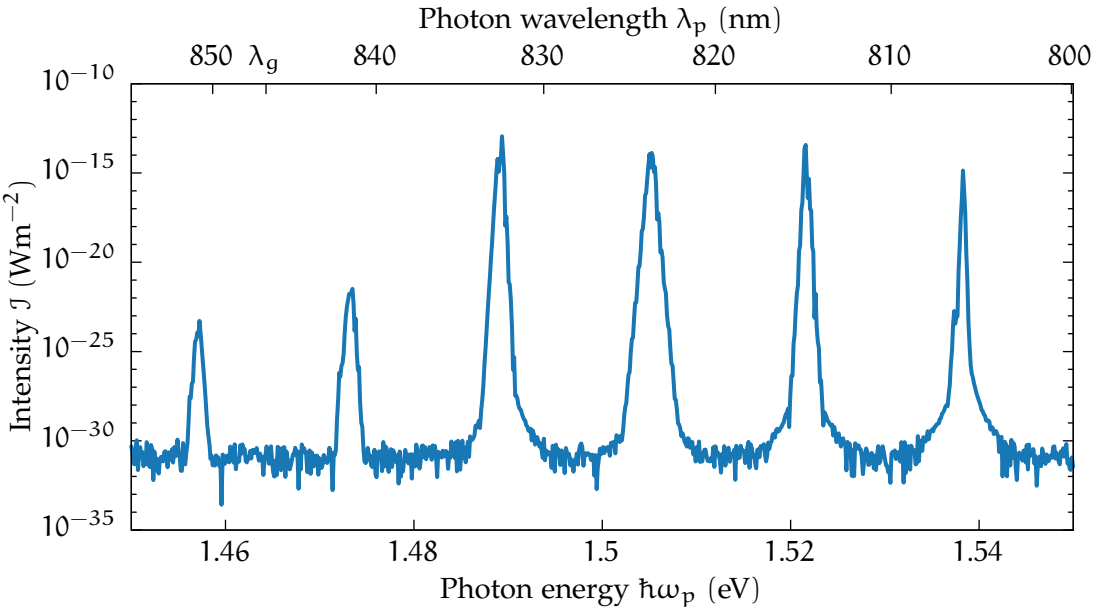


**Figure 4.4:** Spectral content of the output from a QW edge emitting laser. The corresponding time domain data has been collected over the first 9 ns of the simulation.

or more frequencies, $\omega_\nu \approx 2\pi \times 350$ THz, characteristic of the modes of the cavity†. The amplitude of these oscillations, on the other hand, changes on a much longer time scale governed by field and carrier dynamics as well as their interaction. We calculate the variations in the amplitude of the oscillations via a sliding window root-mean-square algorithm, resulting in the envelope shown in fig. 4.3a. This shows that the emission takes the form of a series of pulses ranging in length from a few to a few tens of picoseconds, each one including several thousands of oscillations at the carrier frequency. The pulses are emitted in an irregular series separated by very low-intensity intervals of 10s of picoseconds.

The spectral content of the first 9 ns of time domain signal can be seen in fig. 4.4 plotted with a logarithmic $y$ axis. This shows a set of very marked peaks with a spectral separation which is approximately constant, in agreement with the analytical results for the modes of a passive cavity, eq. 4.8. We also want to draw attention to the fact that the two left-most peaks are about 10 orders of magnitude lower so that we can focus on the higher energy modes,

† We want to stress again that when we discuss results in terms of *modes* we are referring to the presence of specific frequencies in the mode dynamics. These, however, are emerging from our full-field dynamical description in contrast with what is done in models based on phenomenological multimode rate equations.

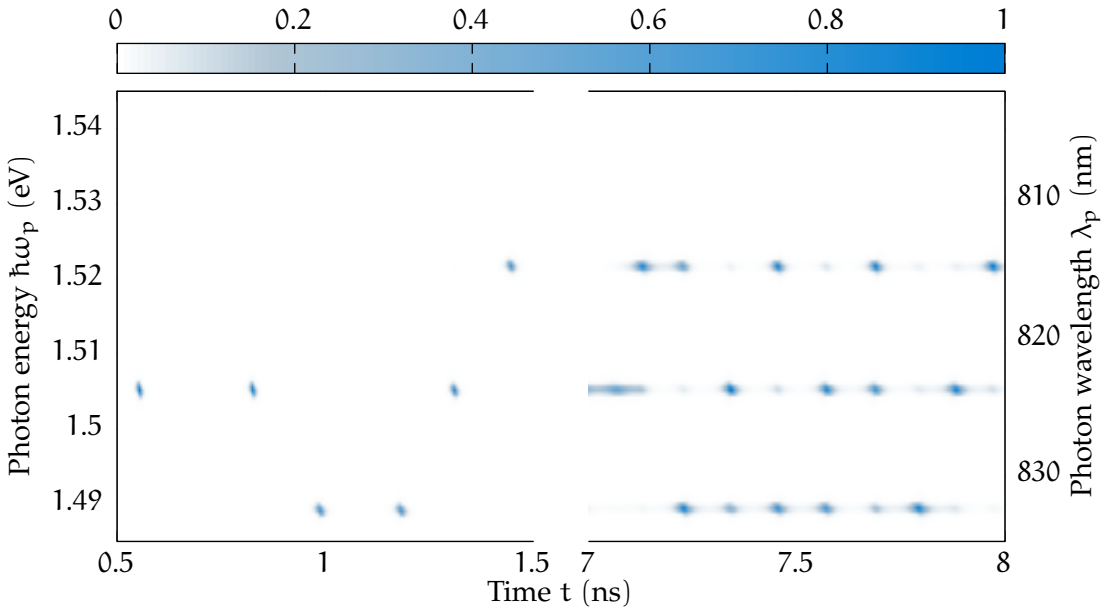


**Figure 4.5:** Time resolved spectral content of the output from a 1D QW edge emitting laser. The left section shows the initial phase of the emission formed by widely spaced single mode pulses. The right section shows the emission in a more advanced state when the pulses get closer together and several modes activate simultaneously.

| $\nu = 1$ | $\nu = 2$ | $\nu = 3$ | $\nu = 4$ |
|---|---|---|---|
| 1.489 eV | 1.505 eV | 1.522 eV | 1.538 eV |
| 832.5 nm | 823.7 nm | 814.8 nm | 806.0 nm |

which will dominate the dynamics. Finally, the spectrograms of the emission during two segments of 1 ns each are shown in fig. 4.5 at the beginning (a) and after few nanoseconds (b). These show how the spectral content of the signal varies over time and thus which *modes* are responsible for the emission of which pulses. In particular, we see that most pulses contain two oscillation frequencies of similar amplitude, while others are single mode in nature. The results in fig. 4.5 show a marked mode hopping in the emission, where the same mode is rarely active for more than a few times in a sequence. Under the assumption that the one or two modes lasing during each pulse are the ones experiencing the highest gain, we conclude that there must be continuous fluctuations in the amount of gain available to each mode. This is confirmed by observing how the spatial distribution of carriers inside the QW evolves over time as a consequence of the

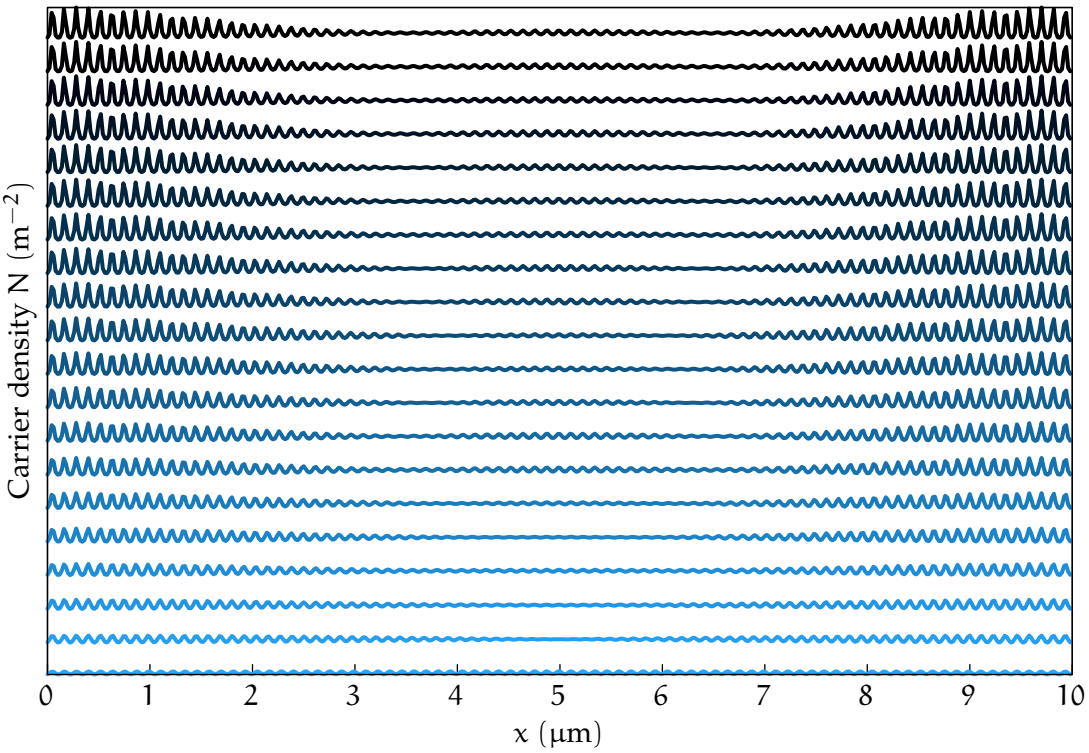


**Figure 4.6:** The lines show the carrier density profile as consecutive snapshots taken at 0.5 ns intervals. The series starts at the bottom (light blue) for $t = 0.5$ ns and ends at $t = 10$ ns (black).

combined effect of pumping and lasing. This highly variable gain dynamics prevent steady state operation from being achieved.

Figure 4.6 shows the time evolution of the carrier density as a series of spatial profiles collected at 0.5 ns intervals between $t = 0.5$ ns (light blue, bottom line) and $t = 10$ ns (black, top line). As the system lases in a specific mode, the gain is depleted with a characteristic spatial pattern corresponding to the mode profile. This remains impressed on the carrier density profile as a negative, i.e., $N(x)$ remains higher where the mode intensity is lower and vice versa, altering the amount of gain available to different modes in a non-uniform way. Due to the regular geometry of the FP modes, it can be shown that the gain depletion from a mode has the highest impact on the mode itself and a much weaker and about uniform impact on other modes. This effect is worsened by the absence of carrier redistribution mechanisms resulting in the very strong spatial hole burning which can be seen in fig. 4.6.

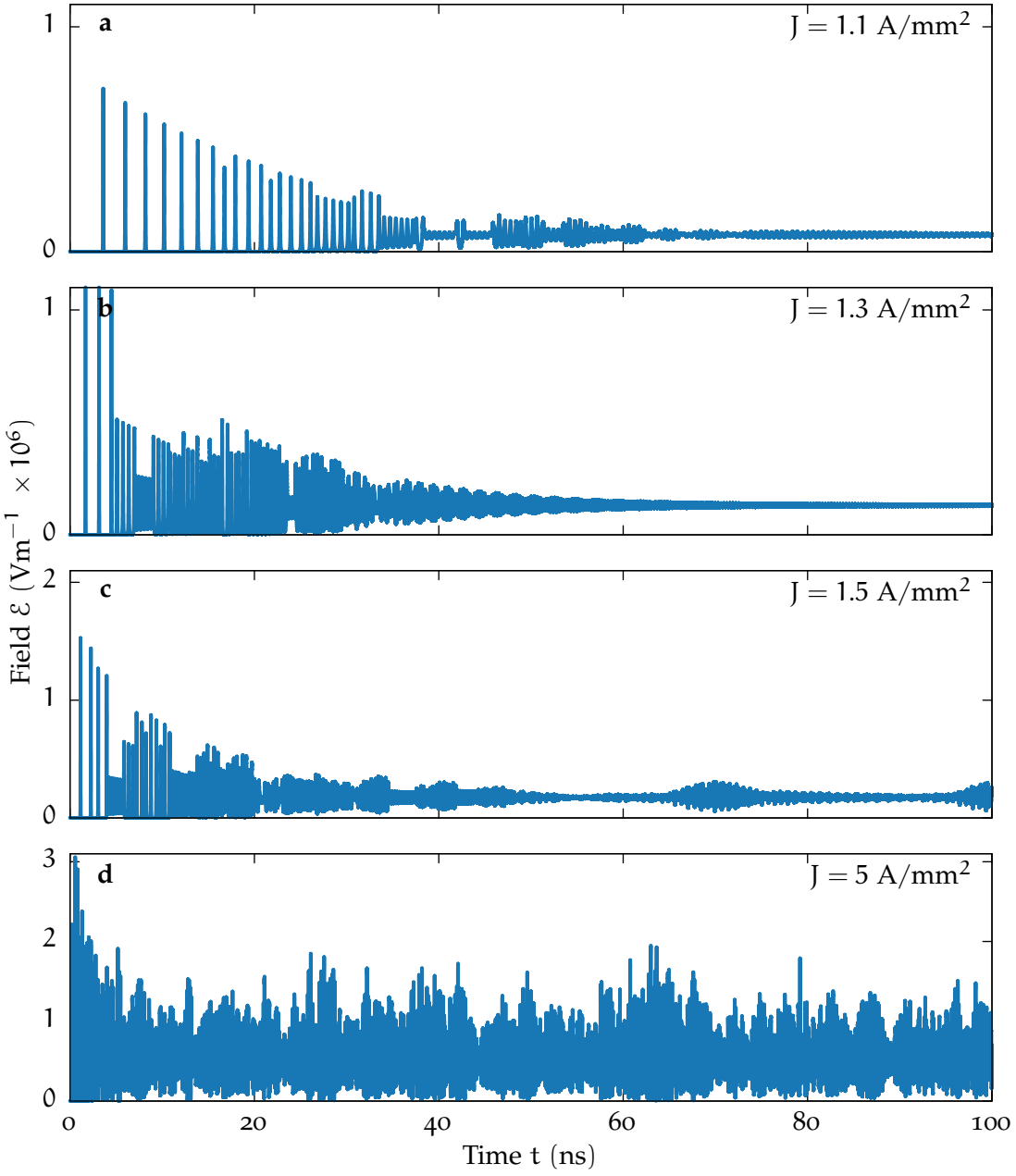


**Figure 4.7:** Time traces of the output field envelope for the first 100 ns of simulation time and different pump currents; a $J = 1.1$ A/mm$^2$, b $J = 1.3$ A/mm$^2$, c $J = 1.5$ A/mm$^2$, d $J = 5.0$ A/mm$^2$. The lasing threshold is $J_{th} = (1.04 \pm 0.03)$ A/mm$^2$.

Lastly, we want to calculate the lasing threshold of this one-dimensional system composed of an extended QW gain model and a FP cavity. The most direct way to do this is to derive the *L-I* curve relating the laser output to the pump, which shows a change in slope at the lasing threshold. To achieve this we perform a set of simulations of the same system at different levels of current density, ranging from $J = 0.9$ A/mm$^2$ to $J = 7.5$ A/mm$^2$. Figure 4.7 shows the envelope of the output field for a few selected simulations, arranged for increasing current densities, $J = \{1.1, 1.3, 1.5, 5.0\}$ A/mm$^2$, from top (a) to bottom (d). First of all, we want to point out the extent of the time axis, and thus the length of the simulation, in comparison with all previous results. This is needed to ensure that the simulations reach an equilibrium condition in which the output intensity can be measured without too many fluctuations. Indeed, all simulations undergo a first stage of variable duration in which the amplitude of the field decreases. This behaviour is particularly apparent under low pump, where the emission is generally more regular, as can be seen in the first 30 ns of fig. 4.7a. Here the emission is characterised by a set of distinct pulses whose amplitude and spacing decreases over time. As the pump intensity is increased this relaxation phase becomes faster. Figure 4.7 also highlights the presence of a trend in the intensity of the irregular fluctuations in amplitude, which is seen to increase with pump intensity. Indeed figs. 4.7a and 4.7b show that a continuous wave (CW) emission regime is achieved for low pump, albeit with small fluctuation coming from the beating of different modes. Under stronger pumping, however, the emission remains highly irregular, e.g., fig. 4.7d, and dominated by the mode hopping phenomenon that we discussed previously. For this reason calculating the emission intensity at high pump is not trivial and can only be performed by averaging the time traces. To confirm the validity of this measure we repeat the average over several different time intervals of the same length. These can then be further averaged to obtain a single value and their standard deviation calculated to provide an estimate of the error. The resulting *L/I* curve can be seen in fig. 4.8 where we use the current density, J, and output intensity, $\mathcal{J}$, instead of the spatially integrated quantities, current intensity and power output respectively. The blue squares are the

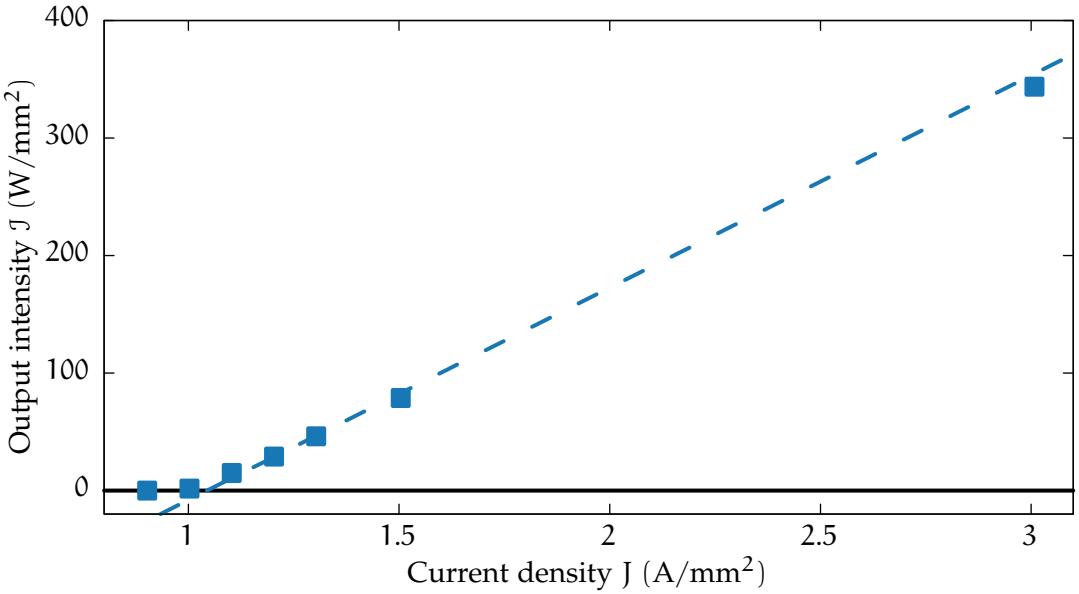


**Figure 4.8:** The blue squares show the average output intensity of the QW laser as a function of pump intensity. The horizontal black line marks the zero and the dashed blue line shows the result of a linear fit. The change in slope around $J = 1$ A/mm$^2$ points at the presence of a lasing threshold.

average output intensities calculated from the data and the corresponding errors are smaller than the squares themselves. A very apparent change in slope marks the lasing threshold, around $J = 1$ A/mm$^2$, below which no emission is observed due to the absence of spontaneous emission in the model. Above threshold we observe that the laser output depends linearly on the current density. By performing a linear fit, blue dashed line, we obtain the slope, $(181 \pm 1)$ W/A, and a better estimate of the lasing threshold, $J_{th} = (1.04 \pm 0.03)$ A/mm$^2$.

## 4.3 TRANSPORT IN A ONE-DIMENSIONAL LASER

We have seen in the previous section that the absence of carrier redistribution mechanisms results in very strong spatial hole burning. This is clearly a limitation of the model, as we expect carriers in a physical system to be able to move around. To determine whether transport has to be included in the model, and at which level of approx-

imation, it is important to understand the characteristic temporal and spatial scales on which carrier redistribution occurs.

One common description of carrier transport is that of a diffusion process in the macroscopic density[125–127],

$$\partial_t N(x,t)\Big|_{\text{diff.}} = D_f \nabla_x^2 N(x,t) \ , \tag{4.9}$$

with the ambipolar diffusion coefficient, $D_f$. This can be easily integrated with our model since we are already tracking all density related effects at a macroscopic level. As an alternative, carrier and polarisation transport can be self-consistently included at the macroscopic level via a set of terms containing real and reciprocal space gradients[14, 92, 128].

In order to assess the impact of diffusion on the system dynamics, we perform a systematic study by running simulations with values of the diffusion coefficient, $D_f$, in a very wide range. In particular, we start from very low values, $D_f = 10^{-6}$ cm$^2$/s, and increase diffusion up to typical experimental values, $D_f \approx 10^2$ cm$^2$/s[13, 16, 129, 130]. Figure 4.9 shows the envelopes of the output field for selected values of the diffusion coefficient, $D_f = \{0, 3\times10^{-3}, 9\times10^{-3}, 3\times10^{-2}\}$ cm$^2$/s, arranged in order of increasing diffusion from top (a) to bottom (d). These show that introducing carrier diffusion leads to a stabilisation of the emission, even for low values of $D_f$, fig. 4.9b. This stabilisation effect becomes faster as the diffusion coefficient is increased toward values consistent with experimental measure, figs. 4.9c and 4.9d. Figure 4.10a shows the spectral content of the emission for values of the diffusion coefficient ranging from $D_f = 0$ cm$^2$/s (black top line) to $D_f = 30$ cm$^2$/s. We observe that, as $D_f$ is increased, the number of lasing modes decreases, leading to a transition to single mode lasing for $D_f \approx 2.5\times10^{-2}$ cm$^2$/s. This behaviour is highlighted in fig. 4.10b, where the intensity of each one of the peaks in fig. 4.10a is tracked as the diffusion coefficient is changed. Both axes of fig. 4.10b are logarithmic. Once the transition to single mode lasing has been reached, the carriers can redistribute quickly enough that the density profile is effectively homogeneous. This

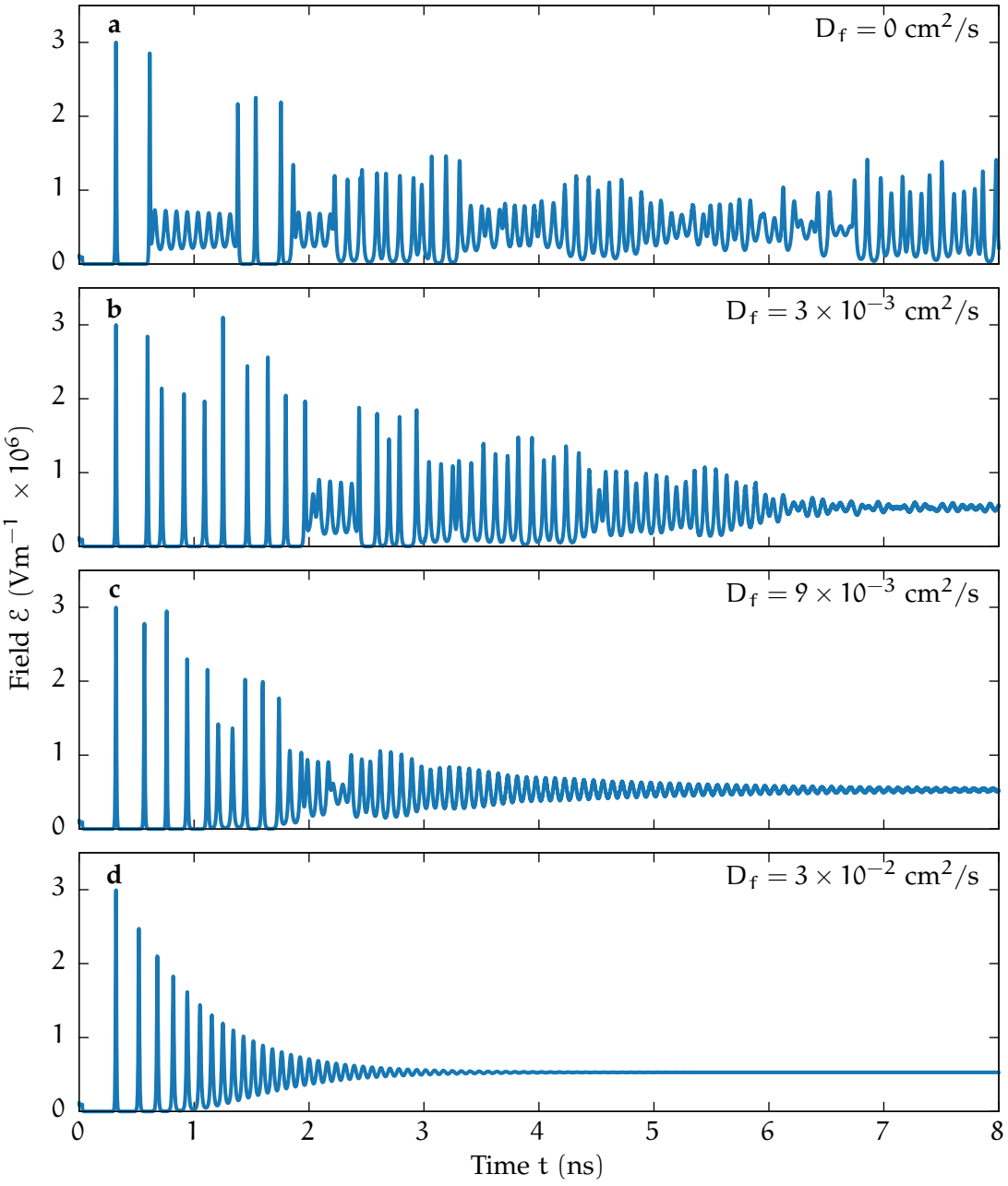


**Figure 4.9:** Time traces of the output field envelope for the first 8 ns of simulation time and different diffusion coefficients; a $D_f = 0\ cm^2/s$, b $D_f = 3 \times 10^{-3}\ cm^2/s$, c $D_f = 9 \times 10^{-3}\ cm^2/s$, d $D_f = 3 \times 10^{-2}\ cm^2/s$.

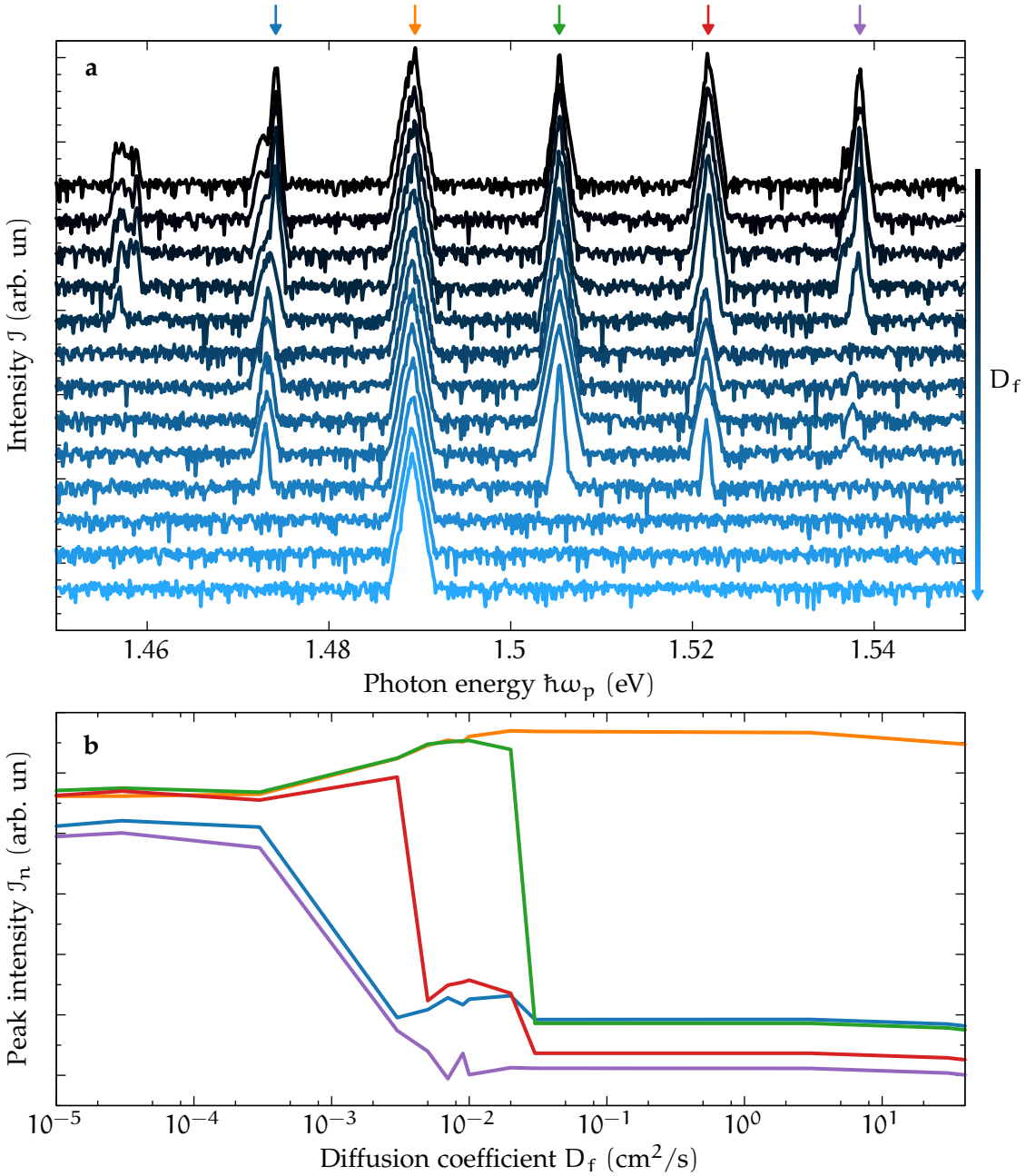


**Figure 4.10:** Pane a shows how the spectral content of the emission changes with increasing diffusion coefficient, $D_f$, going from $D_f = 0$ cm$^2$/s (black line) to $D_f = 30$ cm$^2$/s (light blue). The variation in diffusion coefficient between lines is not uniform, due to the wide range of values. Pane a shows how the intensity of the different modes changes with diffusion coefficient. This is obtained by extracting the peak intensity from the data shown in a. The line colours match the colours of the arrows at the top of pane a. The $y$ axis in a and both axes in b are plotted using a logarithmic scale.

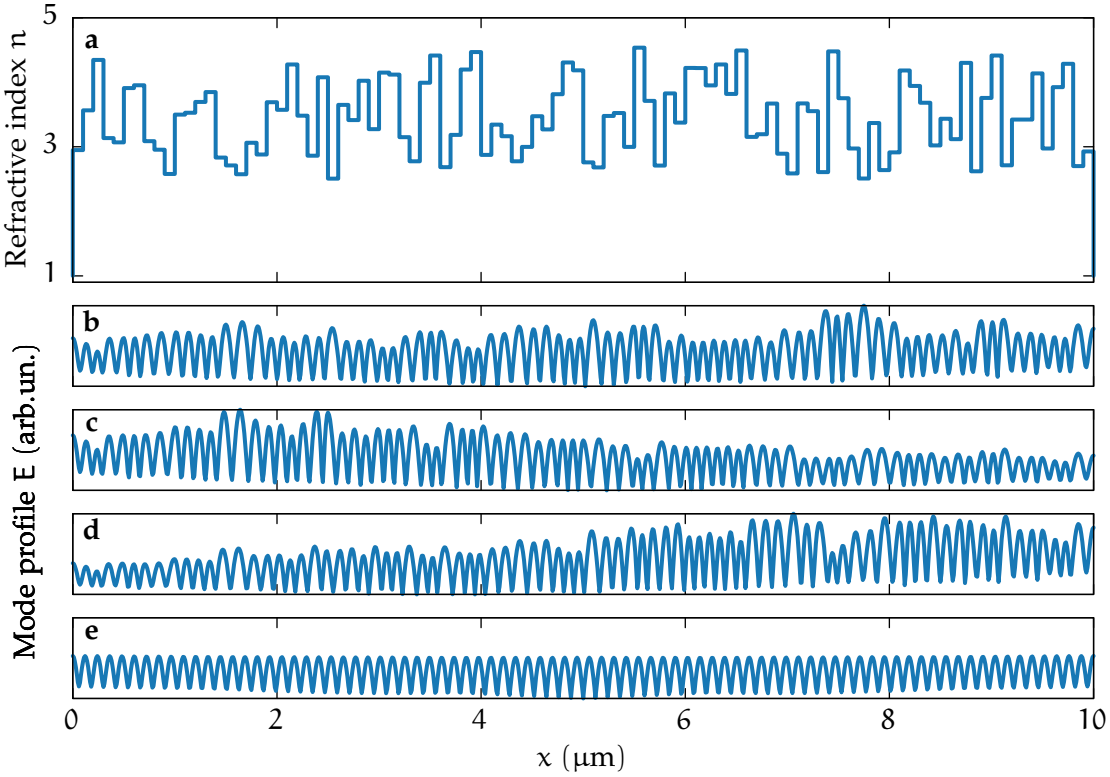


**Figure 4.11:** Pane a shows the randomly generated refractive index profile, $n(x)$, of the disordered 1D cavity. Each slice of the system is 100 nm long. Panes b to d show the spatial profiles of some of the modes of the cavity represented in a. Conversely, pane e shows the spatial profile of one of the modes of the simple FP cavity in fig. 4.2.

results in a steady state CW emission from the single mode which is closest to the gain maximum.

## 4.4 INSTABILITY SUPPRESSION VIA COMPLEX WAVE DYNAMICS

Inspired by the experimentally observed suppression of lasing instabilities from wave-chaotic cavities[2], we investigate if a similar effect can be achieved in one dimension via complex wave interference. We again consider a 10 μm long dielectric cavity, but introduce fluctuations in the refractive index on a sub-wavelength scale, as shown in

fig. 4.11a. The system is subdivided into 100 nm long segments and each one is assigned a randomly generated value of the refractive index,

$$n_i = n_0 (1 + \sigma \xi_i) \ , \tag{4.10}$$

where $\xi_i$ is uniformly distributed in $[-1, 1]$, $\sigma = 0.3$ provides a measure of the fluctuations amplitude and $n_0 = 3.5$ fixes the average of the distribution. In contrast with the case of a FP cavity, which is characterised by homogeneous modes like the one in fig. 4.11e, the modes of a random cavity are spatially dependent as it is seen in figs. 4.11b to 4.11d. These complex mode profiles have non-trivial consequences on the field and carrier dynamics, as well as their interaction. Furthermore, they show spatial features on two different scales which are reminiscent of what can be observed by performing a one-dimensional cut through the modes of a 2D wave chaotic cavity, see for example Bittner et al. [2, fig. S8].

Figure 4.12 shows the field output of the random cavity (fig. 4.12b) compared to that of a simple FP cavity (fig. 4.12a) under a relatively large pump current, $J = 5$ A/mm$^2 \approx 5 J_{th}$ and in the absence of diffusion. This shows that in the case of the random cavity a very stable emission is achieved within a few nanoseconds from the start of the simulation. Furthermore, we calculate the average output intensity for both cavities, as detailed in section 4.2, and find that the output from the random cavity, $\mathcal{I}_r = (716.9 \pm 0.2)$ W/mm$^2$, is comparable with that of the FP cavity, $\mathcal{I}_{FP} = (714 \pm 2)$ W/mm$^2$. Lastly, we compare the spectrogram of the emission from the random cavity (fig. 4.12d) with that of a homogeneous cavity (fig. 4.12c). These show that the mode dynamics during the initial relaxation phase is very similar between the two systems. Figure 4.12d also shows that the CW emission from a complex cavity has a multimode nature.

We perform the same analysis explained in section 4.2 to calculate the lasing threshold of the random cavity. This results in a threshold, $J_{th} = (1.0 \pm 0.1)$ A/mm$^2$, which is very similar to the case of a simple FP cavity. This highlights that the overall properties of the laser are not heavily affected by introducing weak fluctuations in the refractive index. The output field envelopes of the simulations used to calculate the threshold

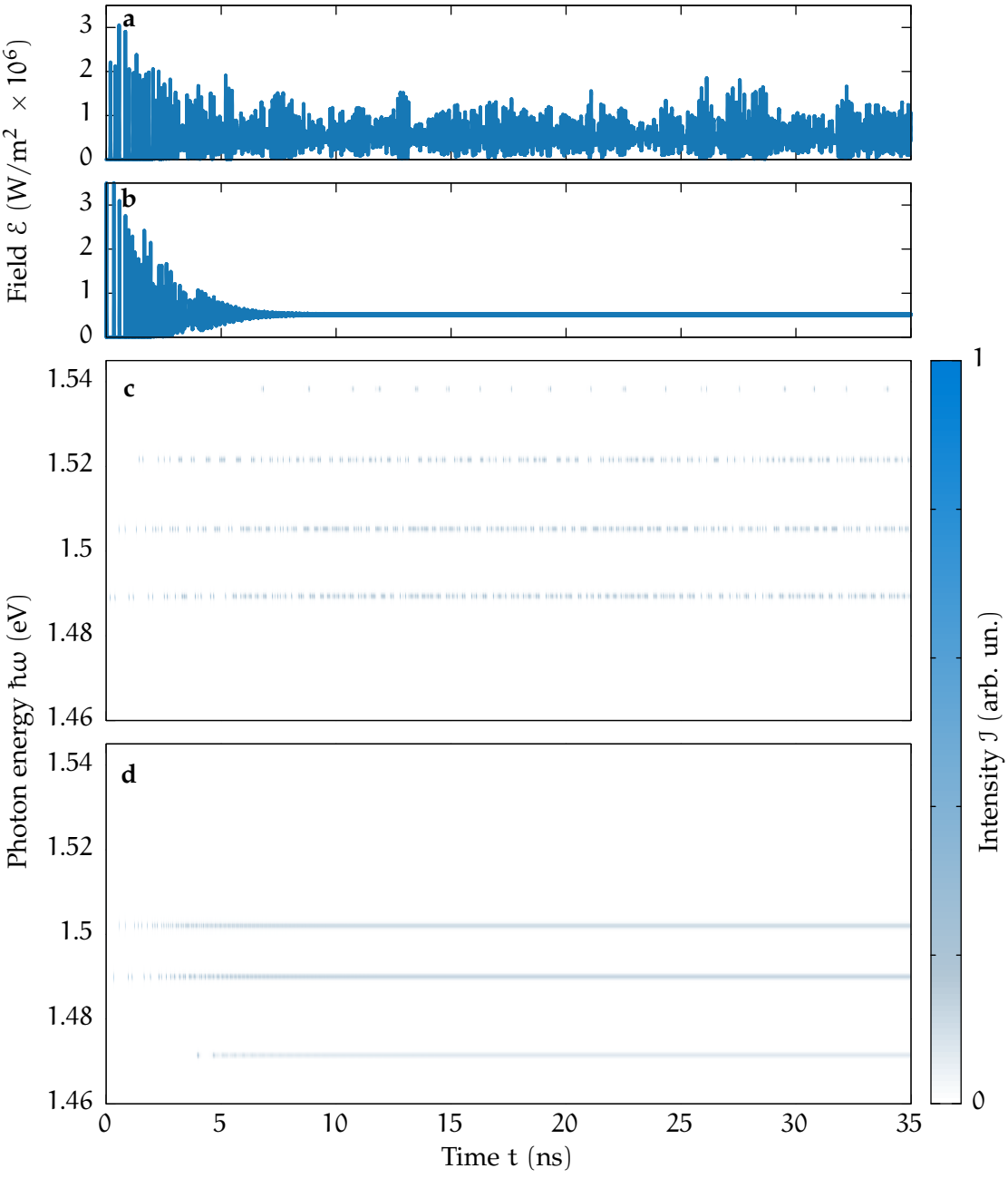


**Figure 4.12:** Comparison of the laser emission from the FP cavity (a and c) and the disordered 1D cavity (b and d). Panes a and b show the time trace of the emission from the two cavities. Panes c and d show the spectrogram of the emission for the two cavities normalised by the respective maximum.

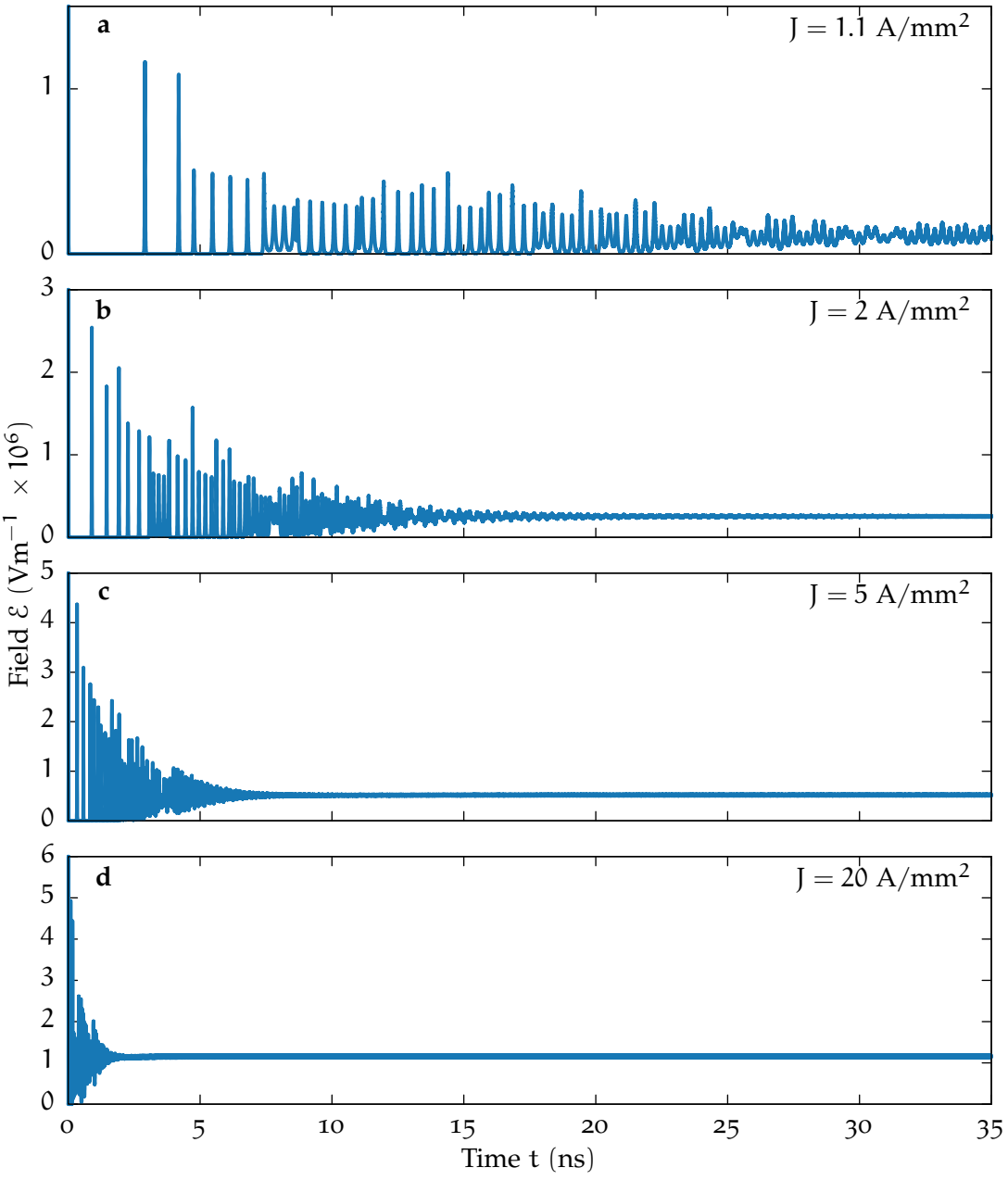


**Figure 4.13:** Time traces of the output field envelope, similarly to fig. 4.7 but obtained from the disordered cavity. The results in different panes are obtained for different pumping intensity as follows; a $J = 1.1$ A/mm$^2$, b $J = 2.0$ A/mm$^2$, c $J = 5$ A/mm$^2$, d $J = 20.0$ A/mm$^2$. The lasing threshold is only slightly modified with respect to the FP cavity and is $J_{th} = (1.0 \pm 0.1)$ A/mm$^2$.

are shown in fig. 4.13 for increasing values of pumping current from just above the threshold, $J \approx 1.1 J_{th}$ (fig. 4.13a), to about 20 times (fig. 4.13d). All of these time traces reach a CW multimode emission supporting the idea that complex wave cavities can be reliably used to achieve stable emission in high power lasers.

## 4.5 CONCLUSION

In this chapter we have numerically investigated the lasing dynamics in a FP QW edge emitting laser. This is achieved via a consistent space, time and band resolved description of the interaction between the semiconductor gain and the electromagnetic field. We observed that the presence of strong fields in the cavity results in a marked spatial hole burning effect on a length-scale which is comparable to the optical wavelength. When the system is pumped at more than a few times the lasing threshold, the spatial hole burning results in a quick mode hopping phenomenon which leads to the presence of dynamical instabilities in the output field. The inclusion of a diffusive behaviour of the macroscopic density results in a complete washing out of any structure on the scale of the wavelength. The resulting transition to a stable single mode emission happens for values of the diffusion coefficient which are 3 to 4 orders of magnitude smaller than reported in the experimental literature. This leads us to hypothesise that a description in terms of a diffusion process is only valid within the slowly-varying envelope approximation and more sophisticated models for carrier transport are needed when performing full wave calculations.

Finally, we demonstrated a novel method to suppress lasing instabilities in one dimension through the use of a disordered cavity. This was inspired by experimental results obtained in a two-dimensional wave-chaotic cavity and is based on the same principle of complex wave interference[2]. By introducing a random patterning of the cavity on a sub-wavelength scale, we showed that a stable multimode lasing regime can be achieved on a wide range of pumping intensities.

# 5 Conclusion and Outlook

In this thesis, we focussed on studying the linear and non-linear optical response of semiconductor systems and its interaction with the environment. In doing so, we hopefully convinced the reader of the usefulness of a self-consistent model for the near-field dynamics of active two-dimensional semiconductors.

In chapter 3 we calculated the non-linear response from a semiconductor Quantum Well (QW) over a wide range of excitation conditions. By using a Maxwell-Bloch based approach, we provided a description going beyond the usual expansion over non-linear susceptibilities, thus allowing the calculation of the non-linear response, e.g., the Third Harmonic Generation (THG), under arbitrary pumping conditions. Furthermore, the time-domain nature of the calculation takes into consideration the effect of dynamical phenomena, e.g., the optical excitation of carriers which produces a saturation in the THG intensity.

The inclusion of the field dynamics on the same footing as the carrier dynamics provides a self-consistent near-field feedback mechanism arising from the semiconductor environment. This description provides better insight in cavity-design compared to a frequency domain calculation of field enhancement. Its dynamical nature would allow a correct description of the field-mediated interaction between multiple emitters within the same cavity.

Similarly, the inclusion of spatially resolved field dynamics proved to be essential when describing systems with a spatially extended gain medium. This has been shown in chapter 4 for the case of a one-dimensional Fabry–Pérot (FP) QW edge emitting laser. In particular, we showed that the emergence of sub-wavelength structures in the distribution of carriers, and thus gain, results in dynamical instabilities in the laser output. We were further able to demonstrate that the introduction of a sub-wavelength pertur-

bation of the optical environment can be used in order to achieve stable continuous wave (CW) emission in a multimode regime.

As it has already been mentioned, the time-domain schema used for the results contained in this thesis could prove very useful in characterising and designing complex cavities consisting of dielectric and plasmonic elements. By further including active elements, e.g., flakes of Transition Metal Dichalcogenide (TMDC) monolayers, and using a self-consistent technique it would be possible to engineer the linear and non-linear response of the system. Moreover, we believe that finding the answer to some fundamental question will further improve the usefulness of the model. A description of the direct and field-mediated interaction between TMDC monolayers and graphene, when closely stacked, would allow to predict the optical properties of van der Waals heterostructures. The inclusion of carrier diffusion in the simulation of a QW laser showed how an understanding of carrier and polarisation transport on short spatio-temporal scales is needed when performing full-field calculations in combination with extended gain systems.

## ORIGINAL CONTRIBUTIONS

This thesis presents a simulation technique capable of calculating the non-linear optical response of a semiconductor in a dynamical fashion. This has been successfully applied in multiple contexts, leading to the following novel contributions.

- The dynamical and microscopic nature of the method allows calculations to be performed under arbitrary excitation conditions, leading to the discovery of a saturation-induced subcubic power of the THG[1].

- The self-consistent approach accurately describes the non-linear behaviour of the system including the optical environment as well as the microscopic structure. The predicted enhancement of the SHG from a TMDC monolayer has been found to be in agreement with experiments, and can thus be used as a tool to design systems with a tailored non-linear response[3].

- Studying the longitudinal dynamics of a FP QW laser revealed that the near-field optical environment has a strong effect on lasing stability. The collaborative experimental and numerical work led to the proposal of a novel paradigm in high-power laser stabilisation[2].

# Bibliography


[1] S. Guazzotti, A. Pusch, D. E. Reiter, and O. Hess. "Dynamical calculation of third-harmonic generation in a semiconductor quantum well" Physical Review B **94**, 115303 (2016) (cit. on pp. 17, 24, 109, 134).

[2] S. Bittner, S. Guazzotti, Y. Zeng, X. Hu, H. Yılmaz, K. Kim, S. S. Oh, Q. J. Wang, O. Hess, and H. Cao. "Suppressing spatiotemporal lasing instabilities with wave-chaotic microcavities" Science (2018) (cit. on pp. 17, 25, 111, 127, 128, 131, 135).

[3] S. Guazzotti, A. Pusch, D. E. Reiter, and O. Hess. "Dynamic theory of nanophotonic control of two-dimensional semiconductor nonlinearities" Physical Review B **98**, 245307 (2018) (cit. on pp. 17, 134).

[4] N. W. Ashcroft and N. Mermin. *Solid State Physics*. Cengage Learning, Inc, 1976. 848 pp. (cit. on pp. 19, 29).

[5] R. Enderlein. *Fundamentals of Semiconductor Physics and Devices*. WORLD SCIENTIFIC PUB CO INC, 1997. 771 pp. (cit. on p. 19).

[6] W. W. Chow, S. W. Koch, and M. Sargent III. *Semiconductor-Laser Physics*. Springer, 2002 (cit. on pp. 19, 20, 56, 57, 59–61, 75, 112).

[7] P. Y. Yu and M. Cardona. *Fundamentals of Semiconductors: Physics and Materials Properties*. Springer, 2005 (cit. on pp. 19, 20, 34, 56).

[8] C. Klingshirn. *Semiconductor Optics (Advanced Texts in Physics)*. Springer, 2005 (cit. on pp. 19, 20).

[9] W. W. Chow and S. W. Koch. *Semiconductor-Laser Fundamentals*. Springer Berlin Heidelberg, 1999. 260 pp. (cit. on p. 20).

[10] H. Haug and S. W. Koch. *Quantum Theory of the Optical and Electronic Properties of Semiconductors (4th Edition)*. WORLD SCIENTIFIC PUB CO INC, 2004. 453 pp. (cit. on pp. 20, 56, 57).

[11] F. Rossi. *Theory of Semiconductor Quantum Devices*. Springer-Verlag GmbH, 2011. 380 pp. (cit. on pp. 20, 57).

[12] T.-H. Kim, K.-S. Cho, E. K. Lee, S. J. Lee, J. Chae, J. W. Kim, D. H. Kim, J.-Y. Kwon, G. Amaratunga, S. Y. Lee, B. L. Choi, Y. Kuk, J. M. Kim, and K. Kim. "Full-colour quantum dot displays fabricated by transfer printing" Nature Photonics **5**, 176 (2011) (cit. on p. 20).

[13] O. Hess. "Spatio-temporal complexity in multi-stripe and broad-area semiconductor lasers" Chaos, Solitons & Fractals **4**, 1597 (1994) (cit. on pp. 21, 124).

[14] O. Hess and T. Kuhn. "Spatio-temporal dynamics of semiconductor lasers: Theory, modelling and analysis" Progress in Quantum Electronics **20**, 85 (1996) (cit. on pp. 21, 124).

[15] I. Fischer, O. Hess, W. Elsäßer, and E. Göbel. "Complex spatio-temporal dynamics in the near-field of a broad-area semiconductor laser" EPL (Europhysics Letters) **35**, 579 (1996) (cit. on p. 21).

[16] J. R. Marciante and G. P. Agrawal. "Spatio-temporal characteristics of filamentation in broad-area semiconductor lasers" IEEE Journal of Quantum Electronics **33**, 1174 (1997) (cit. on pp. 21, 124).

[17] J. R. Marciante and G. P. Agrawal. "Spatio-temporal characteristics of filamentation in broad-area semiconductor lasers: experimental results" IEEE Photonics Technology Letters **10**, 54 (1998) (cit. on p. 21).

[18] M. Arahata and A. Uchida. "Inphase and Antiphase Dynamics of Spatially-Resolved Light Intensities Emitted by a Chaotic Broad-Area Semiconductor Laser" IEEE Journal of Selected Topics in Quantum Electronics **21**, 522 (2015) (cit. on p. 21).

[19] N. B. Abraham, L. A. Lugiato, and L. M. Narducci. "Overview of instabilities in laser systems" Journal of the Optical Society of America B **2**, 7 (1985) (cit. on p. 21).

[20] G. Huyet, M. C. Martinoni, J. R. Tredicce, and S. Rica. "Spatiotemporal Dynamics of Lasers with a Large Fresnel Number" Physical Review Letters **75**, 4027 (1995) (cit. on p. 21).

[21] J. Ohtsubo. *Semiconductor Lasers*. Springer Berlin Heidelberg, 2012 (cit. on p. 21).

[22] J. Martín-Regalado, G. H. M. van Tartwijk, S. Balle, and M. S. Miguel. "Mode control and pattern stabilization in broad-area lasers by optical feedback" Physical Review A **54**, 5386 (1996) (cit. on p. 21).

[23] T. Pawletko, M. Houssin, M. Knoop, M. Vedel, and F. Vedel. "High power broad-area diode laser at 794 nm injected by an external cavity laser" Optics Communications **174**, 223 (2000) (cit. on p. 21).

[24] S. K. Mandre, I. Fischer, and W. Elsäßer. "Spatiotemporal emission dynamics of a broad-area semiconductor laser in an external cavity: stabilization and feedback-induced instabilities" Optics Communications **244**, 355 (2005) (cit. on p. 21).

[25] S. Takimoto, T. Tachikawa, R. Shogenji, and J. Ohtsubo. "Control of Spatio-Temporal Dynamics of Broad-Area Semiconductor Lasers by Strong Optical Injection" IEEE Photonics Technology Letters **21**, 1051 (2009) (cit. on p. 21).

[26] C. Zink, M. Niebuhr, A. Jechow, A. Heuer, and R. Menzel. "Broad area diode laser with on-chip transverse Bragg grating stabilized in an off-axis external cavity" Optics Express **22**, 14108 (2014) (cit. on p. 21).

[27] H. Hodaei, M.-A. Miri, M. Heinrich, D. N. Christodoulides, and M. Khajavikhan. "Parity-time-symmetric microring lasers" Science **346**, 975 (2014) (cit. on p. 21).

[28] W. Liu, M. Li, R. S. Guzzon, E. J. Norberg, J. S. Parker, M. Lu, L. A. Coldren, and J. Yao. "An integrated parity-time symmetric wavelength-tunable single-mode microring laser" Nature Communications **8**, 15389 (2017) (cit. on p. 21).

[29] J. Hamm. "Spatio-Temporal and Polarisation Dynamics of Semiconductor Microcavity Lasers". PhD thesis. Universität Stuttgart, 2004 (cit. on p. 21).

[30] K. Böhringer. "Microscopic Spatio-Temporal Dynamics of Semiconductor Quantum Well Lasers and Amplifiers". PhD thesis. Universität Stuttgart, 2007 (cit. on p. 21).

[31] K. Böhringer and O. Hess. "A full-time-domain approach to spatio-temporal dynamics of semiconductor lasers. I. Theoretical formulation" Progress in Quantum Electronics **32**, 159 (2008) (cit. on pp. 21, 58, 75, 113, 114).

[32] K. Böhringer and O. Hess. "A full time-domain approach to spatio-temporal dynamics of semiconductor lasers. II. Spatio-temporal dynamics" Progress in Quantum Electronics **32**, 247 (2008) (cit. on pp. 21, 58, 75, 113).

[33] S. Calvez, J. E. Hastie, M. Guina, O. G. Okhotnikov, and M. D. Dawson. "Semiconductor disk lasers for the generation of visible and ultraviolet radiation" Laser & Photonics Review **3**, 407 (2009) (cit. on p. 21).

[34] K. S. Novoselov. "Electric Field Effect in Atomically Thin Carbon Films" Science **306**, 666 (2004) (cit. on p. 21).

[35] K. S. Novoselov, A. K. Geim, S. V. Morozov, D. Jiang, M. I. Katsnelson, I. V. Grigorieva, S. V. Dubonos, and A. A. Firsov. "Two-dimensional gas of massless Dirac fermions in graphene" Nature **438**, 197 (2005) (cit. on p. 21).

[36] Y. Zhang, Y.-W. Tan, H. L. Stormer, and P. Kim. "Experimental observation of the quantum Hall effect and Berry's phase in graphene" Nature **438**, 201 (2005) (cit. on p. 21).

[37] A. K. Geim and K. S. Novoselov. "The rise of graphene" Nature Materials **6**, 183 (2007) (cit. on p. 21).

[38] A. H. C. Neto, F. Guinea, N. M. R. Peres, K. S. Novoselov, and A. K. Geim. "The electronic properties of graphene" Reviews of Modern Physics **81**, 109 (2009) (cit. on p. 21).

[39] K. F. Mak, C. Lee, J. Hone, J. Shan, and T. F. Heinz. "Atomically Thin $MoS_2$: A New Direct-Gap Semiconductor" Physical Review Letters **105**, 136805 (2010) (cit. on pp. 22, 97).

[40] A. Splendiani, L. Sun, Y. Zhang, T. Li, J. Kim, C.-Y. Chim, G. Galli, and F. Wang. "Emerging Photoluminescence in Monolayer $MoS_2$" Nano Letters **10**, 1271 (2010) (cit. on p. 22).

[41] T. Li and G. Galli. "Electronic Properties of $MoS_2$ Nanoparticles" The Journal of Physical Chemistry C **111**, 16192 (2007) (cit. on pp. 22, 97).

[42] S. Lebègue and O. Eriksson. "Electronic structure of two-dimensional crystals from *ab initio* theory" Physical Review B **79**, 115409 (2009) (cit. on pp. 22, 97).

[43] H.-P. Komsa and A. V. Krasheninnikov. "Effects of confinement and environment on the electronic structure and exciton binding energy of $MoS_2$ from first principles" Physical Review B **86**, 241201 (2012) (cit. on pp. 22, 23, 102).

[44] T. Cheiwchanchamnangij and W. R. L. Lambrecht. "Quasiparticle band structure calculation of monolayer, bilayer, and bulk $MoS_2$" Physical Review B **85**, 205302 (2012) (cit. on pp. 22, 97).

[45] A. Ramasubramaniam. "Large excitonic effects in monolayers of molybdenum and tungsten dichalcogenides" Physical Review B **86**, 115409 (2012) (cit. on pp. 22, 23, 97).

[46] S. Tongay, J. Zhou, C. Ataca, K. Lo, T. S. Matthews, J. Li, J. C. Grossman, and J. Wu. "Thermally Driven Crossover from Indirect toward Direct Bandgap in 2D Semiconductors: $MoSe_2$ versus $MoS_2$" Nano Letters **12**, 5576 (2012) (cit. on p. 22).

[47] H. Zeng, G.-B. Liu, J. Dai, Y. Yan, B. Zhu, R. He, L. Xie, S. Xu, X. Chen, W. Yao, and X. Cui. "Optical signature of symmetry variations and spin-valley coupling in atomically thin tungsten dichalcogenides" Scientific Reports **3**, 1608 (2013) (cit. on pp. 22, 65).

[48] P. Tonndorf, R. Schmidt, P. Böttger, X. Zhang, J. Börner, A. Liebig, M. Albrecht, C. Kloc, O. Gordan, D. R. T. Zahn, S. M. de Vasconcellos, and R. Bratschitsch. "Photoluminescence emission and Raman response of monolayer $MoS_2$, $MoSe_2$, and $WSe_2$" Optics Express **21**, 4908 (2013) (cit. on p. 22).

[49] T. Cao, G. Wang, W. Han, H. Ye, C. Zhu, J. Shi, Q. Niu, P. Tan, E. Wang, B. Liu, and J. Feng. "Valley-selective circular dichroism of monolayer molybdenum disulphide" Nature Communications **3**, 887 (2012) (cit. on pp. 22, 65, 97).

[50] K. F. Mak, K. He, J. Shan, and T. F. Heinz. "Control of valley polarization in monolayer $MoS_2$ by optical helicity" Nature Nanotechnology **7**, 494 (2012) (cit. on p. 22).

[51] H. Zeng, J. Dai, W. Yao, D. Xiao, and X. Cui. "Valley polarization in $MoS_2$ monolayers by optical pumping" Nature Nanotechnology **7**, 490 (2012) (cit. on p. 22).

[52] G. Sallen, L. Bouet, X. Marie, G. Wang, C. R. Zhu, W. P. Han, Y. Lu, P. H. Tan, T. Amand, B. L. Liu, and B. Urbaszek. "Robust optical emission polarization in $MoS_2$ monolayers through selective valley excitation" Physical Review B **86**, 081301 (2012) (cit. on p. 22).

[53] A. M. Jones, H. Yu, N. J. Ghimire, S. Wu, G. Aivazian, J. S. Ross, B. Zhao, J. Yan, D. G. Mandrus, D. Xiao, W. Yao, and X. Xu. "Optical generation of excitonic valley coherence in monolayer $WSe_2$" Nature Nanotechnology **8**, 634 (2013) (cit. on p. 22).

[54] D. Xiao, W. Yao, and Q. Niu. "Valley-Contrasting Physics in Graphene: Magnetic Moment and Topological Transport" Physical Review Letters **99**, 236809 (2007) (cit. on p. 23).

[55] K. F. Mak, K. L. McGill, J. Park, and P. L. McEuen. "The valley Hall effect in $MoS_2$ transistors" Science **344**, 1489 (2014) (cit. on p. 23).

[56] Z. Y. Zhu, Y. C. Cheng, and U. Schwingenschlögl. "Giant spin-orbit-induced spin splitting in two-dimensional transition-metal dichalcogenide semiconductors" Physical Review B **84**, 153402 (2011) (cit. on p. 23).

[57] D. Xiao, G.-B. Liu, W. Feng, X. Xu, and W. Yao. "Coupled Spin and Valley Physics in Monolayers of $MoS_2$ and Other Group-VI Dichalcogenides" Physical Review Letters **108**, 196802 (2012) (cit. on pp. 23, 97).

[58] P. Cudazzo, I. V. Tokatly, and A. Rubio. "Dielectric screening in two-dimensional insulators: Implications for excitonic and impurity states in graphane" Physical Review B **84**, 085406 (2011) (cit. on pp. 23, 66).

[59] D. Y. Qiu, F. H. da Jornada, and S. G. Louie. "Optical Spectrum of $MoS_2$: Many-Body Effects and Diversity of Exciton States" Physical Review Letters **111**, 216805 (2013) (cit. on pp. 23, 100).

[60] G. Berghäuser and E. Malic. "Analytical approach to excitonic properties of $MoS_2$" Physical Review B **89**, 125309 (2014) (cit. on pp. 23, 62, 64, 66).

[61] P. Cudazzo, L. Sponza, C. Giorgetti, L. Reining, F. Sottile, and M. Gatti. "Exciton Band Structure in Two-Dimensional Materials" Physical Review Letters **116**, 066803 (2016) (cit. on p. 23).

[62] M. M. Ugeda, A. J. Bradley, S.-F. Shi, F. H. da Jornada, Y. Zhang, D. Y. Qiu, W. Ruan, S.-K. Mo, Z. Hussain, Z.-X. Shen, F. Wang, S. G. Louie, and M. F. Crommie. "Giant bandgap renormalization and excitonic effects in a monolayer transition metal dichalcogenide semiconductor" Nature Materials **13**, 1091 (2014) (cit. on pp. 23, 102).

[63] A. Chernikov, T. C. Berkelbach, H. M. Hill, A. Rigosi, Y. Li, O. B. Aslan, D. R. Reichman, M. S. Hybertsen, and T. F. Heinz. "Exciton Binding Energy and Non-hydrogenic Rydberg Series in Monolayer $WS_2$" Physical Review Letters **113**, 076802 (2014) (cit. on p. 23).

[64] K. He, N. Kumar, L. Zhao, Z. Wang, K. F. Mak, H. Zhao, and J. Shan. "Tightly Bound Excitons in Monolayer $WSe_2$" Physical Review Letters **113**, 026803 (2014) (cit. on p. 23).

[65] Z. Ye, T. Cao, K. O'Brien, H. Zhu, X. Yin, Y. Wang, S. G. Louie, and X. Zhang. "Probing excitonic dark states in single-layer tungsten disulphide" Nature **513**, 214 (2014) (cit. on p. 23).

[66] G. Wang, X. Marie, I. Gerber, T. Amand, D. Lagarde, L. Bouet, M. Vidal, A. Balocchi, and B. Urbaszek. "Giant Enhancement of the Optical Second-Harmonic Emission of $WSe_2$ Monolayers by Laser Excitation at Exciton Resonances" Physical Review Letters **114**, 097403 (2015) (cit. on pp. 23, 97, 104, 110).

[67] B. Zhu, X. Chen, and X. Cui. "Exciton Binding Energy of Monolayer $WS_2$" Scientific Reports **5**, 9218 (2015) (cit. on p. 23).

[68] L. V. Keldysh. "Coulomb interaction in thin semiconductor and semimetal films" Soviet Journal of Experimental and Theoretical Physics Letters **29**, 658 (1979) (cit. on pp. 23, 66).

[69] Y. Lin, X. Ling, L. Yu, S. Huang, A. L. Hsu, Y.-H. Lee, J. Kong, M. S. Dresselhaus, and T. Palacios. "Dielectric Screening of Excitons and Trions in Single-Layer $MoS_2$" Nano Letters **14**, 5569 (2014) (cit. on pp. 23, 102).

[70] A. V. Stier, N. P. Wilson, G. Clark, X. Xu, and S. A. Crooker. "Probing the Influence of Dielectric Environment on Excitons in Monolayer $WSe_2$: Insight from High Magnetic Fields" Nano Letters **16**, 7054 (2016) (cit. on p. 23).

[71] A. Raja, A. Chaves, J. Yu, G. Arefe, H. M. Hill, A. F. Rigosi, T. C. Berkelbach, P. Nagler, C. Schüller, T. Korn, C. Nuckolls, J. Hone, L. E. Brus, T. F. Heinz, D. R. Reichman, and A. Chernikov. "Coulomb engineering of the bandgap and excitons in two-dimensional materials" Nature Communications **8**, 15251 (2017) (cit. on pp. 23, 102).

[72] S. Borghardt, J.-S. Tu, F. Winkler, J. Schubert, W. Zander, K. Leosson, and B. E. Kardynał. "Engineering of optical and electronic band gaps in transition metal dichalcogenide monolayers through external dielectric screening" Physical Review Materials **1**, 054001 (2017) (cit. on p. 23).

[73] L. M. Malard, T. V. Alencar, A. P. M. Barboza, K. F. Mak, and A. M. de Paula. "Observation of intense second harmonic generation from $MoS_2$ atomic crystals" Physical Review B **87**, 201401 (2013) (cit. on pp. 23, 65, 97).

[74] Y. Li, Y. Rao, K. F. Mak, Y. You, S. Wang, C. R. Dean, and T. F. Heinz. "Probing Symmetry Properties of Few-Layer $MoS_2$ and h-BN by Optical Second-Harmonic Generation" Nano Letters **13**, 3329 (2013) (cit. on pp. 23, 98).

[75] N. Kumar, S. Najmaei, Q. Cui, F. Ceballos, P. M. Ajayan, J. Lou, and H. Zhao. "Second harmonic microscopy of monolayer $MoS_2$" Physical Review B **87**, 161403 (2013) (cit. on p. 23).

[76] A. K. Geim and I. V. Grigorieva. "Van der Waals heterostructures" Nature **499**, 419 (2013) (cit. on p. 23).

[77] Z. Lin, X. Liang, M. Lončar, S. G. Johnson, and A. W. Rodriguez. "Cavity-enhanced second-harmonic generation via nonlinear-overlap optimization" Optica **3**, 233 (2016) (cit. on pp. 23, 105, 110).

[78] F. Yi, M. Ren, J. C. Reed, H. Zhu, J. Hou, C. H. Naylor, A. T. C. Johnson, R. Agarwal, and E. Cubukcu. "Optomechanical Enhancement of Doubly Resonant 2D Optical Nonlinearity" Nano Letters **16**, 1631 (2016) (cit. on pp. 23, 105, 108, 110).

[79] J. K. Day, M.-H. Chung, Y.-H. Lee, and V. M. Menon. "Microcavity enhanced second harmonic generation in 2D $MoS_2$" Optical Materials Express **6**, 2360 (2016) (cit. on pp. 23, 105).

[80] T. K. Fryett, K. L. Seyler, J. Zheng, C.-H. Liu, X. Xu, and A. Majumdar. "Silicon photonic crystal cavity enhanced second-harmonic generation from monolayer $WSe_2$" 2D Materials **4**, 015031 (2016) (cit. on p. 23).

[81] J. Kern, A. Trügler, I. Niehues, J. Ewering, R. Schmidt, R. Schneider, S. Najmaei, A. George, J. Zhang, J. Lou, U. Hohenester, S. M. de Vasconcellos, and R. Bratschitsch. "Nanoantenna-Enhanced Light–Matter Interaction in Atomically Thin $WS_2$" ACS Photonics **2**, 1260 (2015) (cit. on p. 23).

[82] X. Li, J. Zhu, and B. Wei. "Hybrid nanostructures of metal/two-dimensional nanomaterials for plasmon-enhanced applications" Chemical Society Reviews **45**, 3145 (2016) (cit. on p. 23).

[83] M.-E. Kleemann, R. Chikkaraddy, E. M. Alexeev, D. Kos, C. Carnegie, W. Deacon, A. C. de Pury, C. Große, B. de Nijs, J. Mertens, A. I. Tartakovskii, and J. J. Baumberg. "Strong-coupling of $WSe_2$ in ultra-compact plasmonic nanocavities at room temperature" Nature Communications **8** (2017) (cit. on pp. 23, 86).

[84] A. D. Johnson, F. Cheng, Y. Tsai, and C.-K. Shih. "Giant Enhancement of Defect-Bound Exciton Luminescence and Suppression of Band-Edge Luminescence in Monolayer $WSe_2$–Ag Plasmonic Hybrid Structures" Nano Letters **17**, 4317 (2017) (cit. on p. 23).

[85] K. S. Kunz and R. J. Luebbers. *The Finite Difference Time Domain Method for Electromagnetics*. CRC Press, 1993 (cit. on p. 28).

[86] A. Taflove and S. C. Hagness. *Computational Electrodynamics: The Finite-Difference Time-Domain Method*. ARTECH HOUSE INC, 2005. 1006 pp. (cit. on p. 28).

[87] J. B. Schneider. *Understanding the Finite-Difference Time-Domain Method*. 2010. URL: http://www.eecs.wsu.edu/~schneidj/ufdtd (cit. on p. 28).

[88] C. Kittel. *Introduction to Solid State Physics*. TBS, 1996 (cit. on p. 29).

[89] G. Bastard and J. Brum. "Electronic states in semiconductor heterostructures" IEEE Journal of Quantum Electronics **22**, 1625 (1986) (cit. on pp. 34, 35).

[90] K.-X. Guo and S.-W. Gu. "Nonlinear optical rectification in parabolic quantum wells with an applied electric field" Physical Review B **47**, 16322 (1993) (cit. on p. 34).

[91] P. Harrison and A. Valavanis. *Quantum Wells, Wires and Dots*. John Wiley & Sons, 2016. 624 pp. (cit. on p. 34).

[92] O. Hess and T. Kuhn. "Maxwell-Bloch equations for spatially inhomogeneous semiconductor lasers. I. Theoretical formulation" Physical Review A **54**, 3347 (1996) (cit. on pp. 44, 68, 124).

[93] F. Rossi and T. Kuhn. "Theory of ultrafast phenomena in photoexcited semiconductors" Reviews of Modern Physics **74**, 895 (2002) (cit. on pp. 44, 57, 59).

[94] R. W. Boyd. *Nonlinear Optics*. Elsevier Science, 2008. 640 pp. (cit. on pp. 46, 47).

[95] L. Tsang, D. Ahn, and S. L. Chuang. "Electric field control of optical second-harmonic generation in a quantum well" Applied Physics Letters **52**, 697 (1988) (cit. on pp. 48, 98).

[96] V. M. Axt and A. Stahl. "A dynamics-controlled truncation scheme for the hierarchy of density matrices in semiconductor optics" Zeitschrift für Physik B Condensed Matter **93**, 195 (1994) (cit. on pp. 54, 55).

[97] V. M. Axt and S. Mukamel. "Nonlinear optics of semiconductor and molecular nanostructures; a common perspective" Reviews of Modern Physics **70**, 145 (1998) (cit. on p. 55).

[98] H. W. Wyld and B. D. Fried. "Quantum mechanical kinetic equations" Annals of Physics **23**, 374 (1963) (cit. on p. 59).

[99] U. Hohenester and W. Pötz. "Density-matrix approach to nonequilibrium free-carrier screening in semiconductors" Physical Review B **56**, 13177 (1997) (cit. on p. 59).

[100] M. Bonitz. *Quantum Kinetic Theory*. Teubner-Texte zur Physik 33. B G Teubner, 1998 (cit. on p. 59).

[101] H. Haug and S. W. Koch. "Semiconductor laser theory with many-body effects" Physical Review A **39**, 1887 (1989) (cit. on p. 61).

[102] G. Bastard, E. E. Mendez, L. L. Chang, and L. Esaki. "Exciton binding energy in quantum wells" Physical Review B **26**, 1974 (1982) (cit. on p. 79).

[103] F. Jahnke, M. Kira, and S. W. Koch. "Linear and nonlinear optical properties of excitons in semiconductor quantum wells and microcavities" Zeitschrift für Physik B Condensed Matter **104**, 559 (1997) (cit. on p. 82).

[104] T. Meier and S. W. Koch. "Excitons versus unbound electron-hole pairs and their influence on exciton bleaching: A model study" Physical Review B **59**, 13202 (1999) (cit. on p. 82).

[105] U. Keller and A. C. Tropper. "Passively modelocked surface-emitting semiconductor lasers" Physics Reports **429**, 67 (2006) (cit. on p. 82).

[106] R. Chikkaraddy, B. de Nijs, F. Benz, S. J. Barrow, O. A. Scherman, E. Rosta, A. Demetriadou, P. Fox, O. Hess, and J. J. Baumberg. "Single-molecule strong coupling at room temperature in plasmonic nanocavities" Nature **535**, 127 (2016) (cit. on p. 86).

[107] A. Demetriadou, J. M. Hamm, Y. Luo, J. B. Pendry, J. J. Baumberg, and O. Hess. "Spatiotemporal Dynamics and Control of Strong Coupling in Plasmonic Nanocavities" ACS Photonics **4**, 2410 (2017) (cit. on p. 86).

[108] Y. R. Shen. *The Principles of Nonlinear Optics (Wiley Series in Pure & Applied Optics)*. Wiley-Interscience, 1984 (cit. on p. 93).

[109] W. Schäfer and M. Wegener. *Semiconductor Optics and Transport Phenomena*. Springer Berlin Heidelberg, 2002. 516 pp. (cit. on p. 93).

[110] B. Haase, U. Neukirch, J. Meinertz, J. Gutowski, V. M. Axt, G. Bartels, A. Stahl, J. Nürnberger, and W. Faschinger. "Intensity dependence of signals obtained in four-wave-mixing geometry: influence of higher-order contributions" Journal of Crystal Growth **214-215**, 852 (2000) (cit. on p. 93).

[111] G.-B. Liu, D. Xiao, Y. Yao, X. Xu, and W. Yao. "Electronic structures and theoretical modelling of two-dimensional group-VIB transition metal dichalcogenides" Chemical Society Reviews **44**, 2643 (2015) (cit. on p. 97).

[112] K. L. Seyler, J. R. Schaibley, P. Gong, P. Rivera, A. M. Jones, S. Wu, J. Yan, D. G. Mandrus, W. Yao, and X. Xu. "Electrical control of second-harmonic generation in a $WSe_2$ monolayer transistor" Nature Nanotechnology **10**, 407 (2015) (cit. on p. 98).

[113] W.-T. Hsu, Z.-A. Zhao, L.-J. Li, C.-H. Chen, M.-H. Chiu, P.-S. Chang, Y.-C. Chou, and W.-H. Chang. "Second Harmonic Generation from Artificially Stacked Transition Metal Dichalcogenide Twisted Bilayers" ACS Nano **8**, 2951 (2014) (cit. on p. 98).

[114] J. Zhang, M. Ye, S. Bhandari, A. K. M. Muqri, F. Long, S. Bigham, Y. K. Yap, and J. Y. Suh. "Enhanced second and third harmonic generations of vertical and planar spiral $MoS_2$ nanosheets" Nanotechnology **28**, 295301 (2017) (cit. on p. 98).

[115] T. C. Berkelbach, M. S. Hybertsen, and D. R. Reichman. "Theory of neutral and charged excitons in monolayer transition metal dichalcogenides" Physical Review B **88**, 045318 (2013) (cit. on p. 100).

[116] F. Wu, F. Qu, and A. H. MacDonald. "Exciton band structure of monolayer $MoS_2$" Physical Review B **91**, 075310 (2015) (cit. on p. 100).

[117] B. Scharf, T. Frank, M. Gmitra, J. Fabian, I. Žutić, and V. Perebeinos. "Excitonic Stark effect in $MoS_2$ monolayers" Physical Review B **94**, 245434 (2016) (cit. on p. 100).

[118] K. Thyagarajan, S. Rivier, A. Lovera, and O. J. F. Martin. "Enhanced second-harmonic generation from double resonant plasmonic antennae" Optics Express **20**, 12860 (2012) (cit. on pp. 105, 110).

[119] E. Rosencher, P. Bois, J. Nagle, and S. Delattre. "Second harmonic generation by intersub-band transitions in compositionally asymmetrical MQWs" Electronics Letters **25**, 1063 (1989) (cit. on p. 109).

[120] E. Rosencher, A. Fiore, B. Vinter, V. Berger, P. Bois, and J. Nagle. "Quantum Engineering of Optical Nonlinearities" Science **271**, 168 (1996) (cit. on p. 109).

[121] A. Zardecki. "Fluctuations of optically bistable systems in the bad-cavity limit" Physical Review A **23**, 1281 (1981) (cit. on p. 116).

[122] P. D. Drummond and M. G. Raymer. "Quantum theory of propagation of non-classical radiation in a near-resonant medium" Physical Review A **44**, 2072 (1991) (cit. on p. 116).

[123] J. Andreasen and H. Cao. "Finite-Difference Time-Domain Formulation of Stochastic Noise in Macroscopic Atomic Systems" Journal of Lightwave Technology **27**, 4530 (2009) (cit. on p. 116).

[124] A. Pusch, S. Wuestner, J. M. Hamm, K. L. Tsakmakidis, and O. Hess. "Coherent Amplification and Noise in Gain-Enhanced Nanoplasmonic Metamaterials: A Maxwell-Bloch Langevin Approach" ACS Nano **6**, 2420 (2012) (cit. on p. 116).

[125] H. Hillmer, A. Forchel, S. Hansmann, M. Morohashi, E. Lopez, H. P. Meier, and K. Ploog. "Optical investigations on the mobility of two-dimensional excitons in GaAs/$Ga_1 - xAl_xAs$ quantum wells" Physical Review B **39**, 10901 (1989) (cit. on p. 124).

[126] T. Held, T. Kuhn, and G. Mahler. "Influence of internal electric fields and surface charges on the transport of an optically generated electron-hole plasma" Physical Review B **44**, 12873 (1991) (cit. on p. 124).

[127] H. Hillmer, T. Kuhn, A. Greiner, S. Hansmann, and H. Burkhard. "The role of vertical transport and capture of electrons and holes for the transient optical response in quantum-well heterostructures" Optical and Quantum Electronics **26**, S691 (1994) (cit. on p. 124).

[128] O. Hess and T. Kuhn. "Maxwell-Bloch equations for spatially inhomogeneous semiconductor lasers. II. Spatiotemporal dynamics" Physical Review A **54**, 3360 (1996) (cit. on p. 124).

[129] S. Y. Hu, S. W. Corzine, K.-K. Law, D. B. Young, A. C. Gossard, L. A. Coldren, and J. L. Merz. "Lateral carrier diffusion and surface recombination in InGaAs/AlGaAs quantum-well ridge-waveguide lasers" Journal of Applied Physics **76**, 4479 (1994) (cit. on p. 124).

[130] O. B. Wright, B. Perrin, O. Matsuda, and V. E. Gusev. "Ultrafast carrier diffusion in gallium arsenide probed with picosecond acoustic pulses" Physical Review B **64**, 081202 (2001) (cit. on p. 124).